Search for Heavy Resonances in Four-Top-Quark Final States in pp Collisions at $\sqrt{s}$ = 13 TeV With the ATLAS Detector

Dissertation
zur Erlangung des Doktorgrades
an der Fakultät für Mathematik, Informatik und Naturwissenschaften
Fachbereich Physik
der Universität Hamburg

vorgelegt von
Alicia Wongel

Hamburg
2022

Gutachter der Dissertation:	Dr. Krisztian Peters Prof. Dr. Peter Schleper
Zusammensetzung der Prüfungskommision:	Prof. Dr. Dieter Horns (Vorsitzender) Dr. Krisztian Peters Prof. Dr. Peter Schleper Prof. Dr. Ingrid-Maria Gregor Prof. Dr. Georg Weiglein
Datum der Disputation:	11.07.2022
Vorsitzender Fach-Promotionsausschuss Physik:	Prof. Dr. Wolfgang J. Parak
Leiter des Fachbereichs Physik:	Prof. Dr. Günter H. W. Sigl
Dekan der Fakultät MIN:	Prof. Dr. Heinrich Graener

Eidesstattliche Versicherung | Declaration on oath

Hiermit versichere ich an Eides statt, die vorliegende Dissertationsschrift selbst verfasst und keine anderen als die angegebenen Hilfsmittel und Quellen benutzt zu haben. |
I hereby declare upon oath that I have written the present dissertation independently and have not used further resources and aids than those stated in the dissertation.

Ort, den | City, date
Hamburg, 10.05.2022

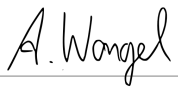

Unterschrift | Signature

Abstract

A search for heavy resonances with a mass of 1 TeV or more in four-top-quark events is presented. This search uses proton-proton-collision data collected with the ATLAS detector at the Large Hadron Collider (LHC) during Run 2 in the years 2015-2018 at a center-of-mass energy of $\sqrt{s} = 13$ TeV. The rare four-top-quark final state can be investigated for the first time with this data set corresponding to an integrated luminosity of 139 fb^{-1}. It offers a unique way to probe top-philic resonances Z' which would predominantly be produced in association with top quarks $t\bar{t}Z' \rightarrow t\bar{t}t\bar{t}$ and are inaccessible by conventional searches. Events with exactly one reconstructed lepton are selected in this search. The particular configuration where the resonance decays fully hadronically is investigated by explicitly reconstructing the resonance. The mass spectrum m_{JJ} is obtained from two reconstructed jets collecting the decay products of the two top quarks from the resonance and is investigated in the range between 1 TeV and 3.2 TeV. In a model-independent interpretation, the data is compared to the expected m_{JJ} distribution. No excess is observed. In a model-dependent interpretation, upper limits on the cross section are computed for six resonance masses between 1 TeV and 3 TeV assuming a simplified model with fixed coupling of the top quark to the resonance. The observed (expected) limits range between 59 (52) fb for a resonance mass of 1 TeV and 11 (10) fb for a resonance mass of 3 TeV. Furthermore, upper limits are presented for different values of the coupling between top quarks and the resonance.

The reach of the LHC is extended to open up more possibilities for discoveries by increasing the precision of measurements and investigating even rarer processes. The LHC and its detectors are scheduled for an extensive upgrade, enabling them to collect a total integrated luminosity of 3 ab^{-1}. A major upgrade of ATLAS is the replacement of its inner detector. The new Inner Tracker (ITk) consists of a pixel silicon detector at small radius and a silicon strip detector at larger radius. The service trays are components of the mechanical structure of the ITk strip detector endcaps in the forward regions. They hold the cooling services and guide the electrical services to the detector components. The development of the final design of the service trays is presented. The quality assurance tests of the service trays are discussed and confirm that the produced service trays meet the required specifications. All service trays for the endcaps are built and ready for assembly with the other structural components.

Zusammenfassung

In dieser Arbeit wird eine Suche nach schweren Resonanzen mit einer Masse von 1 TeV oder mehr in Ereignissen mit vier Top-Quarks vorgestellt. Dazu werden Proton-Proton-Kollisionsdaten ausgewertet, die mit dem ATLAS Detektor am Large Hadron Collider (LHC) während des Run 2 in den Jahren 2015-2018 bei einer Schwerpunktsenergie von $\sqrt{s} = 13\,\text{TeV}$ aufgezeichnet wurden. Der seltene Prozess mit vier Top-Quarks im Endzustand kann zum ersten Mal mit diesem Datensatz von $139\,\text{fb}^{-1}$ untersucht werden. Dieser Endzustand ermöglicht es, nach Resonanzen zu suchen, die vornehmlich zusammen mit einem Top-Quark-Paar im Prozess $t\bar{t}Z' \rightarrow t\bar{t}t\bar{t}$ produziert werden und in konventionellen Suchen nicht zugänglich sind. In dieser Suche werden Ereignisse mit einem rekonstruierten Lepton selektiert und die hadronisch zerfallene Resonanz explizit rekonstruiert. Das Massenspektrum m_{JJ} wird aus zwei rekonstruierten Jets berechnet, welche die Zerfallsprodukte der Top-Quarks aus dem Resonanzzerfall enthalten und im Bereich zwischen 1 TeV und 3,2 TeV untersucht. In einer modellunabhängigen Interpretation werden die Daten mit der erwarteten m_{JJ} Verteilung verglichen, wobei keine Abweichung festgestellt wurde. In einer modellabhängigen Interpretation sind obere Grenzwerte für die Wirkungsquerschnitte für sechs Resonanzmassen zwischen 1 TeV und 3 TeV bestimmt worden. Hierfür wird ein vereinfachtes Modell angenommen mit einer festgelegten Kopplungsstärke der Resonanz zu den Top-Quarks. Die beobachteten (erwarteten) Grenzwerte betragen 59 (52) fb für eine Resonanzmasse von 1 TeV und 11 (10) fb für eine Resonanzmasse von 3 TeV. Des Weiteren werden obere Grenzwerte für verschiedene Werte der Kopplungsstärke zwischen der Resonanz und den Top-Quarks präsentiert.

Die Reichweite des LHC wird außerdem erweitert, um mehr Möglichkeiten für Entdeckungen durch höhere Präzision in Messungen und das Untersuchen von sehr seltenen Prozessen zu schaffen. Der LHC und seine Detektoren werden ausgebaut, sodass $3\,\text{ab}^{-1}$ integrierte Luminosität aufgezeichnet werden können. Der innere Detektor von ATLAS wird dabei vollständig ersetzt mit dem Inner Tracker (ITk). Dieser besteht aus einem Pixel-Silizium-Detektor bei kleinem Radius und einem Silizium-Streifendetektor bei größerem Radius. Die Service Trays sind Teil der mechanischen Strukturen der Endkappen des ITk-Streifendetektors, die sich in Vorwärtsrichtung befinden. In den Service Trays befinden sich die Kühlrohre der Detektorkomponenten und die benötigten Kabel werden an ihnen entlang geführt. Die Entwicklung des finalen Designs der Service Trays wird in dieser Arbeit vorgestellt. Die Tests zur Qualitätssicherung werden präsentiert, in denen sicher gestellt wird, dass die Service Trays die erforderlichen Spezifikationen erfüllen. Alle Service Trays, die für die Endkappen benötigt werden, sind angefertigt und bereit zum Zusammenbau mit den anderen Komponenten der mechanischen Struktur.

Contents

CHAPTER 1

Introduction

The majority of the particles described by the Standard Model of particle physics (SM) was discovered in the 20th century. The most recent discovery of an elementary particle took place in 2012, when the two largest particle physics collaborations in the world announced the observation of the Higgs boson [1, 2]. It was the last missing particle predicted by the SM, currently the most accurate description of the Universe on microscopic scales. Although the predictions of the SM have been confirmed to very high precision, there are phenomena which cannot be described by it. The quantization of gravity, the amount of matter and anti-matter in the Universe and dark matter - gravitational effects observed on cosmological scales which cannot be accounted for by visible matter - remain unexplained in the SM. Many searches for different kinds of phenomena beyond the SM are therefore carried out, aiming to make discoveries that would shine light on these mysteries. Different theoretical models predict extensions of the SM that introduce new particles to address these unexplained phenomena. Several experiments therefore look for such new particles. One possibility to search for them is to collide high energy particle beams and analyze the resulting products.

CERN, the European Organization for Nuclear Research, hosts the largest particle collider in the world, the Large Hadron Collider (LHC). At the LHC, detectors are positioned at the four collision points to collect the produced particles. One of them is the ATLAS (A Toroidal LHC ApparatuS) detector. The data collected with the ATLAS detector is thoroughly analyzed and searches for new particles are performed. One search performed with data collected by the ATLAS detector is presented in this thesis.

Among the many production and decay modes that might involve new elementary particles, searches involving top quarks form an interesting group because they could offer insights on a theoretical challenge regarding the Higgs boson mass. The Higgs mass predicted by the SM is very large because of correction terms from the different particle masses. Of all particles in the SM, the top quarks have the largest mass which leads to the largest correction terms of the Higgs mass. The observed Higgs mass is however much smaller than its predicted mass. Potential observations of top quarks coupling to new particles would provide additional information for understanding the nature of this mechanism.

One approach to search for these new particles is to investigate resonances that decay to a top quark pair. It is typically assumed that such a new particle is produced through light quark pair annihilation. However, this production mode could be suppressed if the coupling of the new particle to light quarks is small. Searches for resonances in four-top-quark final states, as the one presented in this thesis, offer the possibility to find resonances which only or mainly couple to top quarks. Only now with the availability of the so far largest data set collected at the LHC, rare processes with four-top-quark final states can be probed. First evidence of the SM production with this final state has only recently been observed [3]. The unique feature of the analysis presented here is the explicit reconstruction of the potential new resonance. This allows for a model-independent search of deviations from the SM in the investigated resonance mass range. A data-driven approach is used to estimate the expected background to avoid known mismodeling in the simulations. It extends the LHC search programme by probing the existence of resonances with high masses coupling predominantly to top quarks. If no such resonance is discovered, bounds on the parameters of models extending the SM can be derived. Consequently, the possibilities of how these resonances could be realized in Nature are narrowed down.

So far no new particles were observed in the data currently available. In addition, even more precise measurements of the SM than presently possible would offer additional possibilities to identify deviations from it. Therefore, the LHC will extend its reach for potential discoveries and will be upgraded to increase the number of collisions per time unit. Consequently, more particles will be produced which increases the discovery potential of rare processes. The ATLAS detector has to be adapted to that new environment of larger collision numbers and for that, its entire inner detector will be replaced by a new silicon Inner Tracker (ITk). The forward regions of this detector, the so-called endcaps, consist of a carbon fiber based mechanical structure and detector sensitive silicon components. The service trays are part of the mechanical structure and contribute to its stability. They also hold the cooling services and guide the electrical services to the different layers of the endcaps. The development and prototyping processes as well as the final production of the service trays are presented here.

This thesis is organized as follows. In Chapter 2, the SM of particle physics and examples for its limitations are presented. This chapter also includes an overview of selected models predicting resonances that mainly couple to top quarks. In Chapter 3, relevant concepts of collider physics are discussed and the principles of Monte Carlo simulation described. In Chapter 4, the LHC complex and the ATLAS experiment are presented. Details about the subsystems of the ATLAS detector and the methods applied to reconstruct physics objects from the collected data are described. An overview of the planned high luminosity upgrade of the LHC is given. In Chapter 5, details on the replacement of the inner detector of ATLAS with the new ITk are presented with an emphasis on the mechanical structure of the endcaps. This includes a comprehensive description of the design, testing and production of the ITk endcap service trays. In Chapter 6, the search for heavy resonances in four-top-quark final states with the ATLAS detector is presented. Details on the background estimation applied in this analysis, the statistical interpretation and results are shown here. The limitations of the analysis are discussed and an outlook discussing potential future prospects of the analysis is given. In Chapter 7, the presented projects are summarized.

Author's contributions

Today's largest particle physics experiments are collaborative endeavors and involve many people working together on different aspects of the experiment. The ATLAS collaboration has 3000 members who contribute to the maintenance and upgrade of the detector as well as the data analysis and interpretation. Without this combined effort of so many, the work presented here would not have been possible. Since the results presented in this thesis rely on the efforts of many people, the author's contributions are summarized here.

The author was one of two main contributors to the search for heavy resonances in four-top-quark final states [4]. Together with another PhD student, Elise Le Boulicaut, the author implemented and maintained the analysis framework, evaluated the systematic uncertainties and carried out extensive studies to test the performance of the statistical model. The author carried out the model-independent and model-dependent interpretation of the results and contributed to the documentation of the search for the publication.

The author developed the ITk endcap service trays together with the engineering team of the DESY ATLAS group. The author helped finalize the design, developed and carried out extensive tests to fulfill the electrical and mechanical specifications and manufactured several of the final service trays to be installed in the ATLAS detector.

The search presented in this thesis has been published as ATLAS conference note and figures from this publication are labeled as "ATLAS Preliminary". The latest results from this search will be presented in a publication which is about to be submitted to a peer-reviewed journal. Unless referenced accordingly in the caption, figures without this label have been produced by the author. Milestones of the different components of the ATLAS detector upgrade have been presented in technical design reports and are indicated as such.

CHAPTER 2

Theoretical Overview

All currently known elementary particles are described by the Standard Model of particle physics which is introduced in this chapter. Its predictions are continuously confirmed by measurements at ever higher precision. Nevertheless, there remain phenomena in the realm of particle physics that cannot be explained by it. Many theories describing new particles are developed to solve these open questions. Examples for such theories that predict heavy resonances which could be observed in the four-top-quark final state are presented.

2.1 The Standard Model of Particle Physics

The Standard Model of particle physics (SM) is currently the most accurate description of the Universe on microscopic scales. Summaries of the SM can be found in Ref. [5–8] among many others. The four fundamental forces of Nature are gravity, the electromagnetic force, the weak force and the strong force. While the SM describes the other three forces, gravity is currently not described by it. As the quantization of gravity has not been established yet, it cannot be included in the SM so far. Its effect on elementary particles is however small because of their small masses and gravity can therefore be neglected when describing their interactions.

2.1.1 Particle Content

The particles described by the SM can be split into two groups according to their spin. Particles with half-integer spin follow the Fermi-Dirac statistics [9, 10] and are called fermions. Particles with integer spin follow the Bose-Einstein statistics [11] and are called bosons. The fermions make up all known matter and can be further divided into strongly interacting quarks and leptons which are not subject to the strong force. There exist three generations of quarks and leptons which have identical quantum numbers but increasing masses for higher generations.

The up (u), strange (s) and top (t) quark have an electric charge of +2/3 while the down (d), charm (c) and bottom (b) quark have an electric charge of -1/3. The quarks additionally have a color charge

which can be red, green or blue. For each quark q there exists an antiquark $\bar{q}$ with the same mass and opposite electric and color charge.

They can be arranged in left-handed quark doublets with weak isospin $I_3 = \pm\frac{1}{2}$

$$\begin{pmatrix} u \\ d' \end{pmatrix}_L, \begin{pmatrix} c \\ s' \end{pmatrix}_L, \begin{pmatrix} t \\ b' \end{pmatrix}_L \tag{2.1}$$

and right-handed quark singlets with weak isospin $I_3 = 0$

$$u_R, d_R, s_R, c_R, t_R, b_R\,. \tag{2.2}$$

The mixing between the mass eigenstates d, s, b and the weak eigenstates d', s', b' is described by the Cabibbo-Kobayashi-Maskawa (CKM) matrix [12, 13]

$$\begin{pmatrix} d' \\ s' \\ b' \end{pmatrix} = \begin{pmatrix} V_{ud} & V_{us} & V_{ub} \\ V_{cd} & V_{cs} & V_{cb} \\ V_{td} & V_{ts} & V_{tb} \end{pmatrix} \cdot \begin{pmatrix} d \\ s \\ b \end{pmatrix}. \tag{2.3}$$

There are three leptons with an electric charge of -1: the electron (e), the muon (μ) and the tau (τ). Three leptons are electrically neutral: the electron neutrino (ν_e), the muon neutrino (ν_μ) and the tau neutrino (ν_τ). In the SM, the neutrinos are predicted to be massless. There are left-handed lepton doublets with weak isospin $I_3 = \pm\frac{1}{2}$

$$\begin{pmatrix} \nu_e \\ e \end{pmatrix}_L, \begin{pmatrix} \nu_\mu \\ \mu \end{pmatrix}_L, \begin{pmatrix} \nu_\tau \\ \tau \end{pmatrix}_L \tag{2.4}$$

and right-handed lepton singlets with weak isospin $I_3 = 0$

$$e_R, \mu_R, \tau_R\,. \tag{2.5}$$

For each charged lepton l there exists an antilepton $\bar{l}$ with opposite electric charge, lepton number and chirality. The lepton number is defined to be +1 for leptons and -1 for antileptons.

The interactions between the particles are mediated by the bosons. The electromagnetic force affects electrically charged particles and the photon which is the mediator of the electromagnetic force. The photon is massless and electrically neutral.

All particles except the right-handed fermions carry weak charge and therefore interact via the weak force. It is mediated by the electrically charged W^+ and W^- bosons, as well as the electrically neutral Z boson. As opposed to the other mediators, the $W^\pm$ and Z bosons are massive.

The strong force affects the color-charged quarks and the gluons which are the mediators of the strong force. The gluons are electrically neutral but color-charged and massless. Due to the different color charges there exist 8 different gluons. The photon, $W^\pm$ and Z bosons and the gluons all have a spin of 1 and are therefore vector bosons.

The so-called Higgs mechanism gives mass to the fermions. It induces electroweak symmetry breaking which leads to the $W^\pm$ and Z boson being massive (see Section 2.1.6). As a consequence, a scalar (spin 0) particle arises from this mechanism which is the Higgs boson.

The particles of the SM and their properties are summarized in Figure 2.1.

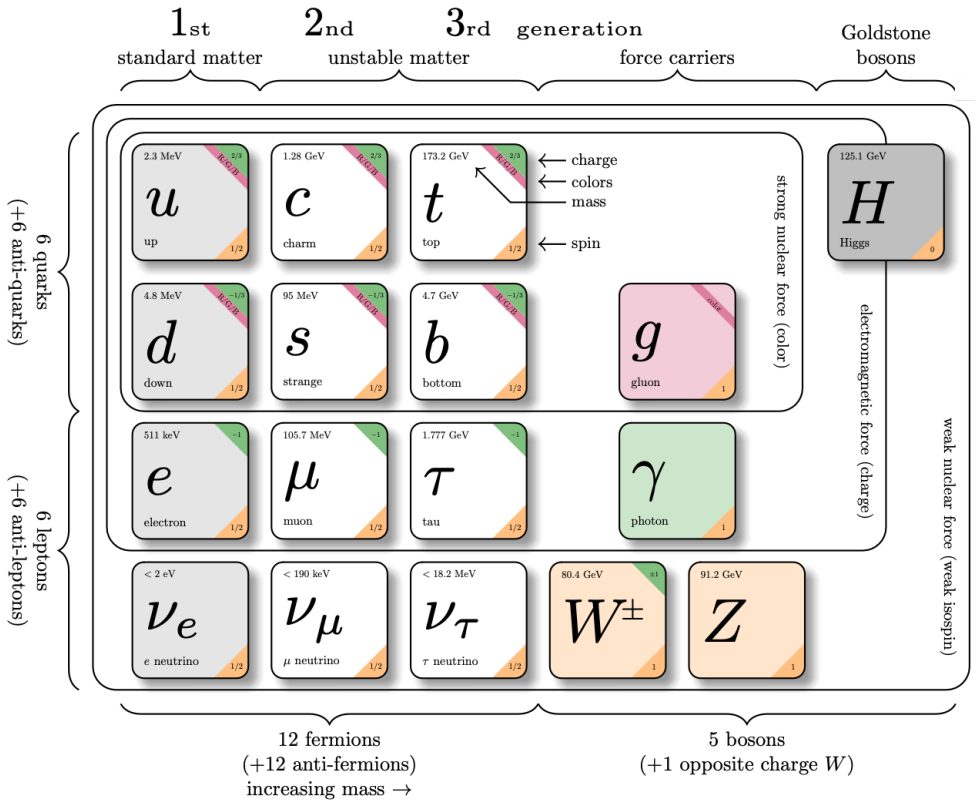

Figure 2.1: SM particles and their properties. The electric charge, color charge, mass and spin of each particle are shown. Figure modified from Ref. [14].

Due to color confinement, quarks as well as gluons cannot be observed as individual particles. Instead, they form composite states called hadrons which are color neutral. Hadrons that consist of pairs of quarks and antiquarks are called mesons and hadrons that consist of three quarks are called baryons. Historically, the underlying quark structure of mesons and baryons was discovered while studying the properties of the composite states [15].

2.1.2 Fundamental Interactions

The SM can be described mathematically with Quantum Field Theory (QFT). Its local gauge group is

$$\mathrm{SU(3)_C} \otimes \mathrm{SU(2)_L} \otimes \mathrm{U(1)_Y}. \tag{2.6}$$

$\mathrm{SU(3)_C}$ is the third degree special unitarity group describing the strong force and C stands for color charge. $\mathrm{SU(2)_L}$ is the second degree special unitarity group describing the electroweak force

and L stands for left-handedness implying that this interaction affects left-handed fermions only. $\mathrm{U}(1)_\mathrm{Y}$ is the unitarity group of first degree and Y stands for the hypercharge defined as $\mathrm{Y} = 2(Q - I_3)$ where Q is the electric charge and I_3 is the weak isospin.

2.1.3 Quantum Electrodynamics

The electromagnetic interaction is described by Quantum Electrodynamics (QED). The Lagrangian describing a free Dirac fermion can be denoted as

$$\mathcal{L}_0 = i\overline{\psi}(x)\gamma^\mu\partial_\mu\psi(x) - m\overline{\psi}(x)\psi(x) \tag{2.7}$$

where $\psi(x)$ is a Dirac spinor describing the fermion, $\overline{\psi}(x) = \psi(x)^\dagger\gamma^0$, and m is the mass of the fermion.

The gamma matrices γ^μ satisfy the anticommutation relations $\{\gamma^\mu, \gamma^\nu\} = 2g^{\mu\nu}$, where $g^{\mu\nu}$ is the Minkowski metric.

The Lagrangian $\mathcal{L}_0$ is invariant under the U(1) symmetry

$$\psi(x) \overset{\mathrm{U}(1)}{\longrightarrow} \quad \psi'(x) \equiv \exp\{iQ\theta\}\psi(x), \tag{2.8}$$

where $Q\theta$ is an arbitrary constant. It is however not invariant under a local U(1) transformation, as

$$\partial_\mu\psi(x) \overset{\mathrm{U}(1)}{\longrightarrow} \exp\{iQ\theta(x)\}\left(\partial_\mu + iQ\partial_\mu\theta(x)\right)\psi(x). \tag{2.9}$$

Therefore, an additional field A_μ is introduced which transforms under a local U(1) transformation as

$$A_\mu(x) \overset{U(1)}{\longrightarrow} A'_\mu(x) \equiv A_\mu(x) - \frac{1}{e}\partial_\mu\theta(x). \tag{2.10}$$

The field A_μ corresponds to the photon. With the covariant derivative defined as

$$D_\mu\psi(x) \equiv \left[\partial_\mu + ieQA_\mu(x)\right]\psi(x) \tag{2.11}$$

the following Lagrangian is obtained which is invariant under a local U(1) transformation:

$$\mathcal{L} = i\overline{\psi}(x)\gamma^\mu D_\mu\psi(x) - m\overline{\psi}(x)\psi(x). \tag{2.12}$$

The kinetic term of the field A_μ

$$\mathcal{L}_{kin} = \frac{1}{4}F_{\mu\nu}F^{\mu\nu}, \tag{2.13}$$

is added to the Lagrangian, where $F_{\mu\nu}$ is the field strength tensor $F_{\mu\nu} = \partial_\mu A_\nu - \partial_\nu A_\mu$.
This leads to the full QED Lagrangian

$$\mathcal{L}_{\mathrm{QED}} = \overline{\psi}\left(i\gamma^\mu\partial_\mu - m\right)\psi - \overline{\psi}e\gamma_\mu A^\mu\psi - \frac{1}{4}F^{\mu\nu}F_{\mu\nu}. \tag{2.14}$$

A mass term of the field A_μ of the form $\mathcal{L}_m = \frac{1}{2}m^2 A^\mu A_\mu$ violates gauge invariance. Therefore, the photon is predicted to be massless.

The fundamental QED vertex can be presented by a Feynman diagram as shown in Figure 2.2. In all Feynman diagrams shown in this thesis, time proceeds from left to right. The diagrams in this section are created with Ref. [16].

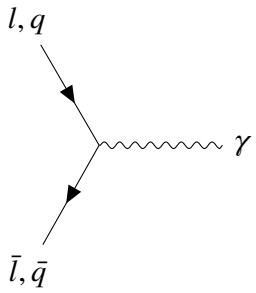

Figure 2.2: Feynman diagram of the fundamental QED vertex.

2.1.4 Quantum Chromodynamics

The strong interaction is described by Quantum Chromodynamics (QCD). A similar approach as for the QED Lagrangian can be applied to obtain the QCD Lagrangian.

Combining the quark field q_f^α of color α and flavor f into a vector in color space according to $q_f^T = (q_f^r, q_f^g, q_f^b)$, the free Lagrangian can be written as

$$\mathcal{L}_0 = \sum_f \overline{q}_f \left(i\gamma^\mu \partial_\mu - m_f\right) q_f, \tag{2.15}$$

with the gamma matrices γ^μ and the quark masses m_f. It is invariant under a transformation of the SU(3) symmetry group

$$q_f^\alpha \rightarrow \left(q_f^\alpha\right)' = U_\beta^\alpha q_f^\beta, \; U = \exp\left\{i\frac{\lambda^a}{2}\theta_a\right\}, \tag{2.16}$$

where $\frac{\lambda^a}{2}$ are the generators of the symmetry. The eight Gell-Mann-matrices λ^a satisfy the commutation relation

$$\left[\frac{\lambda^a}{2}, \frac{\lambda^b}{2}\right] = if^{abc}\frac{\lambda^c}{2}, \tag{2.17}$$

where f^{abc} are the structure constants.

Local invariance under a SU(3) transformation can be established with the covariant derivative defined as

$$D^\mu q_f \equiv \left[\partial^\mu + ig_s\frac{\lambda^a}{2}G_a^\mu(x)\right] q_f, \tag{2.18}$$

where g_s is the strong coupling constant. Because there are eight independent gauge parameters, also eight gauge bosons $G_a^\mu(x)$ exist. These correspond to the eight gluons.

The kinetic term of the gluons

$$\mathcal{L}_{kin} = -\frac{1}{4} G_a^{\mu\nu} G^a_{\mu\nu}, \tag{2.19}$$

is introduced where $G^{\mu\nu}$ is defined as

$$G_a^{\mu\nu}(x) = \partial^\mu G_a^\nu - \partial^\nu G_a^\mu - g_s f^{abc} G_b^\mu G_c^\nu. \tag{2.20}$$

This leads to the QCD Lagrangian

$$\mathcal{L}_{\text{QCD}} = \overline{\psi}_q \left(i\gamma^\mu \partial_\mu - m \right) \psi_q - \overline{\psi}_q g_s \gamma^\mu \frac{\lambda_a}{2} G_a^\mu \psi_q - \frac{1}{4} G_a^{\mu\nu} G^a_{\mu\nu}. \tag{2.21}$$

The gluon is predicted to be massless because a mass term would violate gauge invariance. Because of the non-commutativity of the $\mathrm{SU}(3)_C$ matrices, an additional term arises in the Lagrangian containing only the gluon fields. It describes the self-interaction of the gluons which does not exist in QED. The QCD interactions are shown in Figure 2.3.

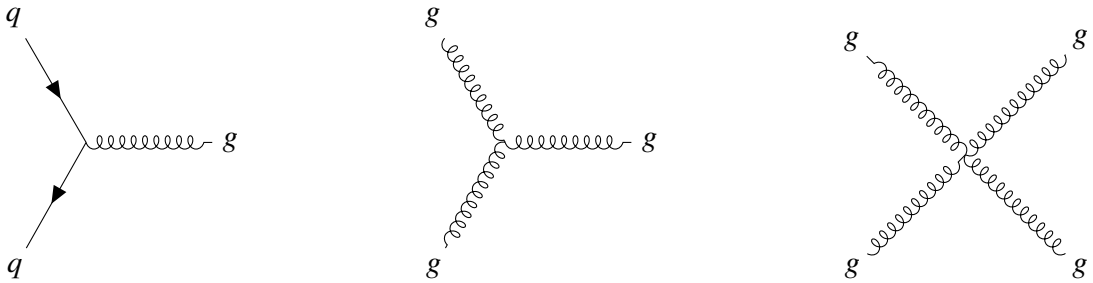

Figure 2.3: Feynman diagrams of the fundamental QCD vertices.

2.1.5 The Electroweak Sector

The unification of the electromagnetic and the weak force was suggested by Glashow [17], Weinberg [18] and Salam [19]. The corresponding symmetry group to describe the unification of the two forces into the electroweak (EW) force is $\mathrm{SU}(2)_\mathrm{L} \otimes \mathrm{U}(1)_\mathrm{Y}$.

The free Lagrangian for quarks and leptons is

$$\mathcal{L}_0 = i\overline{\psi}_{L/R}(x) \gamma^\mu \partial_\mu \psi_{L/R}(x) \tag{2.22}$$

where a sum over all quark and lepton flavors is understood. ψ_L denotes left-handed doublets and ψ_R denotes right-handed singlets defined as

$$\psi_{L/R} = [(1 \mp \gamma_5)/2]\psi, \quad \overline{\psi}_{L/R} = \overline{\psi}[(1 \pm \gamma_5)/2]. \tag{2.23}$$

The mass terms of the fermions are omitted for now, as they violate gauge invariance when constructed from mixing of left-handed and right-handed components. This Lagrangian is invariant under global SU(2) transformations which only affects the left-handed fields ψ_L and $\overline{\psi}_R$.

One new field B^μ is introduced from requiring local invariance under U(1) and three new fields W^i_μ (i=1,2,3) are introduced from requiring local invariance under SU(2).

The covariant derivative is defined as

$$D_\mu \psi_{L/R} \equiv \left[\partial_\mu + ig\frac{\sigma_i}{2}W^i_\mu + ig'\frac{Y}{2}B_\mu\right]\psi_{L/R}, \tag{2.24}$$

where g and g' are the gauge couplings for SU(2) and U(1) respectively, Y is the hypercharge and σ_i are the Pauli matrices. The kinetic terms for the four fields are added to the Lagrangian

$$\mathcal{L}_{kin} = -\frac{1}{4}W^i_{\mu\nu}W_i^{\mu\nu} - \frac{1}{4}B_{\mu\nu}B^{\mu\nu}, \tag{2.25}$$

with

$$B_{\mu\nu} = \partial_\mu B_\nu - \partial_\nu B_\mu \quad \text{and} \quad W^i_{\mu\nu} = \partial_\mu W^i_\nu - \partial_\nu W^i_\mu - g\varepsilon^{ijk}W^j_\mu W^k_\nu, \tag{2.26}$$

where ε^{ijk} are the group structure constants which for SU(2) are equivalent to the totally anti-symmetric Levi-Civita tensor.

These fields can then be identified with the photon, the $W^\pm$ and Z bosons through

$$W^\pm_\mu = \frac{1}{\sqrt{2}}(W^1_\mu \mp iW^2_\mu) \tag{2.27}$$

and

$$\begin{pmatrix} A_\mu \\ Z_\mu \end{pmatrix} = \begin{pmatrix} \cos\theta_W & \sin\theta_W \\ -\sin\theta_W & \cos\theta_W \end{pmatrix} \cdot \begin{pmatrix} B_\mu \\ W^3_\mu \end{pmatrix} \tag{2.28}$$

with the Weinberg angle θ_W satisfying

$$\cos\theta_W = \frac{g}{\sqrt{g^2 + g'^2}}, \quad \sin\theta_W = \frac{g'}{\sqrt{g^2 + g'^2}}. \tag{2.29}$$

The resulting EW Lagrangian is then

$$\begin{aligned}\mathcal{L}_{EW} = \overline{\psi}_L i\gamma^\mu \partial_\mu \psi_L - \overline{\psi}_L \gamma^\mu \left(g\frac{\sigma_i}{2}W^i_\mu + g'\frac{Y}{2}B_\mu\right)\psi_L \\ - \overline{\psi}_R \gamma^\mu \left(g'\frac{Y}{2}B_\mu\right)\psi_R - \frac{1}{4}W^i_{\mu\nu}W_i^{\mu\nu} - \frac{1}{4}B_{\mu\nu}B^{\mu\nu}.\end{aligned} \tag{2.30}$$

The interactions following from this Lagrangian are shown in Figure 2.4. Interactions involving the $W^\pm$ bosons are also referred to as charged current interactions. Interactions involving the Z boson or photon γ are also referred to as neutral current interactions. Similarly as in QCD, self-interactions of the gauge bosons arise from the Lagrangian.

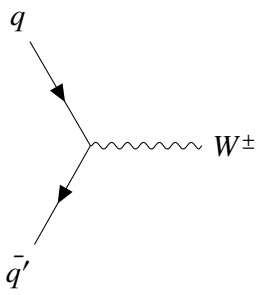

(a) Charged current interaction with left-handed quark doublets q and $\bar{q}'$ except for the kinematically forbidden $(t, \bar{b}')$

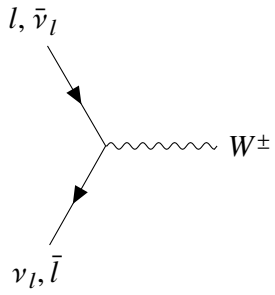

(b) Charged current interaction with the left-handed lepton doublets

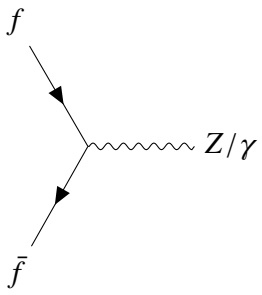

(c) Neutral current interactions with a fermion f; the interaction of a photon with two neutrinos is not allowed

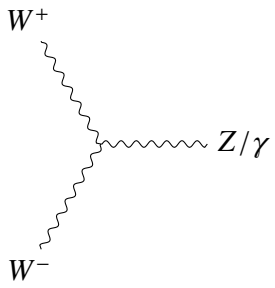

(d) Cubic self interactions of the gauge bosons

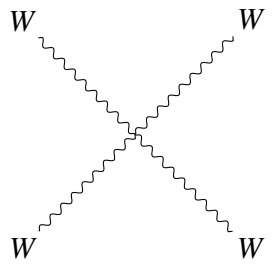

(e) Self interactions of the $W^{\pm}$-bosons conserving charge

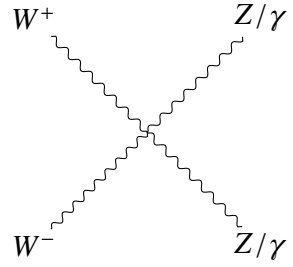

(f) Quartic self interactions of the gauge bosons

Figure 2.4: Feynman diagrams of the fundamental weak interactions.

2.1.6 The Higgs Sector

In the theoretical descriptions presented previously, the fermions and gauge bosons are still massless. As these particles are massive in Nature, spontaneous symmetry breaking was suggested [20–23] and its renormalizability confirmed later [24].

A potential $V(\phi)$ is introduced as

$$V(\phi) = \mu^2 \phi^\dagger \phi + \lambda \left(\phi^\dagger \phi\right)^2 \tag{2.31}$$

for an $\mathrm{SU(2)_L}$ doublet

$$\phi(x) = \begin{pmatrix} \phi^+(x) \\ \phi^0(x) \end{pmatrix}. \tag{2.32}$$

The following Lagrangian is defined

$$\mathcal{L} = \partial_\mu \phi^\dagger \partial^\mu \phi - V(\phi) \tag{2.33}$$

which is invariant under the transformation

$$\phi(x) \longrightarrow \phi'(x) \equiv \exp\{i\theta\}\phi(x). \tag{2.34}$$

By requiring $\lambda > 0$, a ground state is introduced depending only on μ. For $\mu^2 > 0$, the minimum is $\phi = 0$. For $\mu^2 < 0$, the minimum is

$$v = \langle 0|\phi|0\rangle = \sqrt{\frac{-\mu^2}{\lambda}} \tag{2.35}$$

which is called the Vacuum Expectation Value (VEV). Because of the U(1) invariance of the Lagrangian, the VEV is not unique and infinite ground states $v = \sqrt{\frac{-\mu^2}{\lambda}}\exp\{i\theta\}$ are possible. The typical choice is given in Eq. 2.35. This ground state spontaneously breaks the $\mathrm{SU(2)_L}$ symmetry which gives rise to three massless Goldstone bosons, one for every broken generator [25].

The field ϕ can be parametrized in terms of the Higgs field as

$$\phi(x) = \exp\left\{i\frac{\sigma_j}{2}\theta^j(x)\right\}\frac{1}{\sqrt{2}}\begin{pmatrix} 0 \\ v + h(x) \end{pmatrix}. \tag{2.36}$$

Here, $\theta^j(x)$ correspond to the massless Goldstone bosons and $h(x)$ to the Higgs boson. Because of local invariance of the Lagrangian, $\theta^j(x)$ can be chosen such that any dependence on them is removed. In this unitarity gauge, one sets $\theta^j(x) = 0$.

The Lagrangian then becomes

$$\mathcal{L} = (D_\mu\phi)^\dagger D^\mu\phi - \mu^2h^2 - \lambda v h^3 - \frac{1}{4}\lambda h^4 \tag{2.37}$$

with the EW covariant derivative $D_\mu\phi$ defined in Eq. 2.24. The mass of the Higgs boson is obtained from the quadratic term

$$m_h = \sqrt{2}\mu = \sqrt{2\lambda}v. \tag{2.38}$$

The first term of the Lagrangian of Eq. 2.33 can be expressed as

$$\left(D_\mu\phi\right)^\dagger D^\mu\phi \quad \overset{\theta^t=0}{\longrightarrow} \frac{1}{2}\partial_\mu h\partial^\mu h + (v+h)^2\left\{\frac{g^2}{4}W^+_\mu W^{\mu-} + \frac{1}{8}(g^2+g'^2)Z_\mu Z^\mu\right\}. \tag{2.39}$$

The quadratic terms yield the masses of the electroweak gauge bosons

$$m_W = \frac{v}{2}g, \quad m_Z = \frac{v}{2}\sqrt{g^2+g'^2}, \quad m_\gamma = 0. \tag{2.40}$$

Additionally, terms involving the Higgs field arise.

The masses of the fermions arise from a Yukawa-type Lagrangian of the form

$$\mathcal{L}_Y = -c_f(\overline{\psi}_L\phi\psi_R + \overline{\psi}_R\phi\psi_L) = -\frac{1}{\sqrt{2}}(v+h)c_f(\overline{\psi}_L\psi_R + \overline{\psi}_R\psi_L). \tag{2.41}$$

The resulting fermion masses are

$$m_f = c_f \frac{v}{\sqrt{2}}. \tag{2.42}$$

The c_f in the Lagrangian are arbitrary constants and correspond the fermion masses. The fermion masses cannot be derived from theory but have to be measured in experiments.

The interactions associated with the Higgs boson are shown in Figure 2.5.

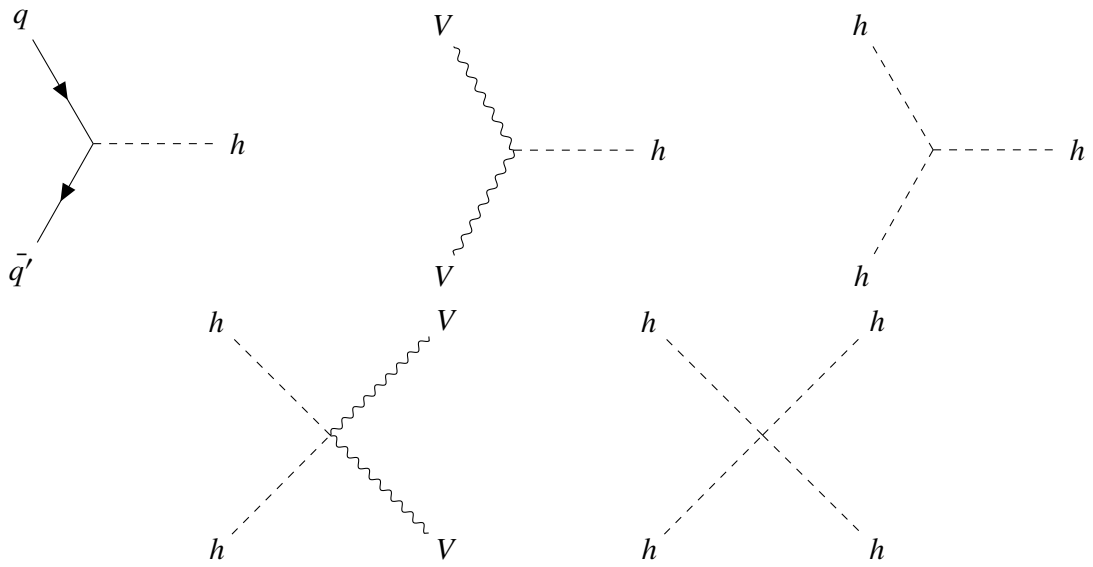

Figure 2.5: Feynman diagrams of the fundamental Higgs interactions with $V = W^{\pm}, Z$.

With the discovery of the Higgs Boson in 2012 [1, 2], the last missing particle predicted by the SM was observed. However, there remain particle physics phenomena which cannot be explained by the SM in its current form.

2.2 Shortcomings of the Standard Model

The SM very accurately describes numerous phenomena on the microscopic scale. Its predictions are observed which confirm the theory further, such as the discovery of the top quark [26]. Despite these great successes, there remain some unanswered questions in the realm of particle physics that cannot be explained by the SM. A few examples are given here.

Gravity

As described in the previous section, the SM describes three of the four fundamental forces but does not include gravity. Although the gravitational force is negligibly small for particles, one theory to describe all four forces is still desired. In order to describe gravity by a QFT, it would be necessary

to quantize the gravitational force. Despite of ongoing efforts, so far no theory could be developed that unifies all four forces and is confirmed by experiments.

Matter-Antimatter Asymmetry

According to the SM, roughly same amounts of matter and antimatter should have been produced in the early stages of the Universe. Since instead, the current Universe exists mainly of matter this symmetry has to be broken. Although several processes in the SM were observed that violate charge and parity (CP) invariance as for example in kaon decays [27], these do not suffice to explain the existing asymmetry in the Universe.

Neutrino Masses

The neutrinos are predicted to be massless in the SM. Observations of flavor changing processes of the neutrinos however require that the neutrinos have a mass. First indications for neutrinos changing their flavor were observed with the Homestake experiment [28]. It was shown that the measured electron neutrino flux from electron neutrinos coming from the Sun did not match the expected rate computed from the Sun's luminosity. This discrepancy can be explained by neutrino oscillation. The electron neutrinos change their flavor on their way from the Sun to Earth and are therefore missed in the measurements. For this neutrino oscillation to take place, it is necessary for the neutrinos to have mass. The observable flavor states of the neutrinos can then be understood as combinations of the mass eigenstates. These are connected through the Pontecorvo-Maki-Nakagawa-Sakate (PMNS)-matrix [29, 30]:

$$\begin{pmatrix} \nu_e \\ \nu_\mu \\ \nu_\tau \end{pmatrix} = \begin{pmatrix} U_{e1} & U_{e2} & U_{e3} \\ U_{\mu 1} & U_{\mu 2} & U_{\mu 3} \\ U_{\tau 1} & U_{\tau 2} & U_{\tau 3} \end{pmatrix} \begin{pmatrix} \nu_1 \\ \nu_2 \\ \nu_3 \end{pmatrix}. \tag{2.43}$$

The Super Kamiokande [31] and the SNO [32] experiments have presented observations of neutrino oscillation in 1998 and 2001. They measured the fluxes of the different neutrino flavors and found them to be incompatible with the predictions without neutrino oscillation.

Hierarchy Problem

The Hierarchy problem summarizes the large discrepancy between the energy scales of the different forces. Similarly, a problem of naturalness arises, as in a natural theory the different energy scales would be of the same order of magnitude. The energy scale of the electroweak interaction is defined by the electroweak symmetry breaking scale $\mathcal{O}(100\,\mathrm{GeV})$. Gravity however becomes relevant at the Planck scale $\mathcal{O}(10^{19}\,\mathrm{GeV})$. The Hierarchy problem becomes apparent when considering the Higgs mass. From the Yukawa coupling of the fermions to the Higgs boson c_f arise correction factors to the Higgs mass:

$$m_H^2 = m_{H_0}^2 - \frac{c_f^2 \Lambda^2}{16\pi^2} + ..., \tag{2.44}$$

where m_{H_0} is the bare Higgs mass and Λ the cutoff scale of the SM. As the top quark is the heaviest fermion, it also leads to the largest Higgs mass correction term. The only theoretical restriction of the cutoff scale Λ is the Planck scale where the SM breaks down. Any potential massive new particles would lead to large correction terms of the Higgs mass. As the measured value of the Higgs mass is $m_H = (125.10 \pm 0.14)\,\text{GeV}$ [33], already the large correction terms from the SM particles have to be artificially cancelled out by fine tuning the bare Higgs mass. Instead, the large loop corrections could be cancelled out by some effects of new physics.

Dark Matter

Dark matter describes the gravitational effects inferred from cosmological observations which cannot be accounted for by any known form of visible matter. An introductory summary can for example be found in [34]. Fritz Zwicky computed the gravitational masses of galaxies of the Coma Cluster in the 1930's [35]. He discovered that the masses he calculated substantially differed from the masses inferred by the luminosities of the galaxies. He attributed the difference to some invisible form of matter which he called "dark matter". Vera Rubin studied rotation velocities of spiral galaxies in the 1970's and confirmed Zwicky's findings [36]. Another indication of dark matter is given by anisotropies in the Cosmic Microwave Background which cannot be explained by SM physics [37].

Following these observations, many experiments have been carried out in order to further understand the nature of dark matter. Historically, non-luminous astrophysical objects as well as neutrinos were considered to account for the additional mass. These options were later disfavored as they cannot explain the amount of dark matter that is observed. Although not proven, it is oftentimes assumed that dark matter consists of one or multiple yet undiscovered particles. So far, it is only known that the potential dark matter particle interacts only or predominantly through gravity. Its interactions through the other forces are either non-existent or very small. Among other possibilities to discover dark matter particles, they are looked for at particle accelerators. Here, the collision of SM particles would lead to the production of dark matter particles. It would therefore be necessary for the dark matter particles to couple to the SM particles.

Theories that extend the SM are continuously being developed and tested in experiments. These theories are aimed at explaining the described phenomena and oftentimes introduce new particles to achieve that.

2.3 The Four-Top Quark Final State

The final state studied in the analysis presented in this thesis consists of four top quarks. It occurs in SM processes and is also predicted in theories Beyond the Standard Model (BSM) that introduce new resonances which couple to the top quark.

The top quark is the heaviest particle of the SM with a mass of about 173 GeV [33]. It therefore plays an outstanding role as this leads to a large coupling with the Higgs boson. Final states involving top quarks offer the possibility to get further insights about its properties which may help to understand the hierarchy problem as described in Section 2.2.

The decay modes of the top quark need to be taken into account when studying them with particle detectors. The top quark has a very short lifetime of about 10^{-24}s [33] due to its high mass. It therefore decays before it can hadronize as the other quarks. The dominant decay mode with almost 100% is the decay to a W boson and a b-quark. The specific final states that are looked for at experiments result from the different W decays. The branching ratio (BR) of the W decaying to a lepton (e, μ, τ) and a neutrino is about 1/3, while the BR into hadrons is about 2/3. The τ lepton in turn decays again hadronically with a BR of about 65% and leptonically (now only including e and μ) with a BR of about 35%.

2.3.1 Four-Top-Quark Production in the SM

Studying also rare processes involving top quarks that are predicted in the SM can offer additional information about the top quark. The production of four top quarks is one such rare process. It has not been discovered yet but evidence of this process was reported recently by ATLAS [3]. Typical Feynman diagrams of the production of four tops in the SM are shown in Figure 2.6. In the production via the Higgs boson shown in Figure 2.6(c), the Higgs boson is off shell to produce the top-quark-pair.

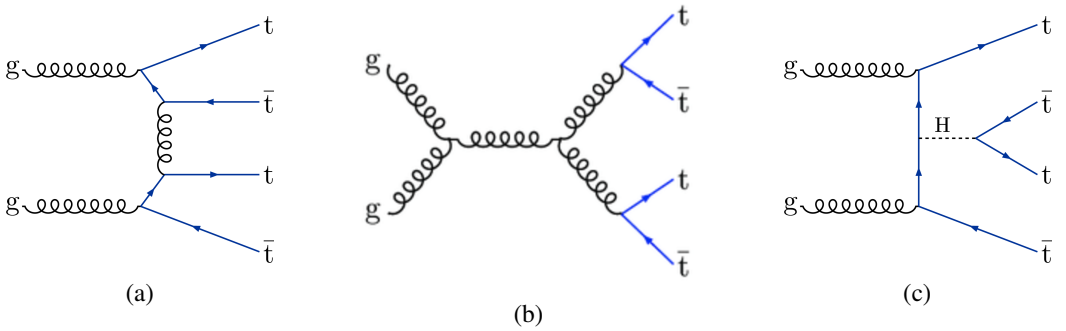

Figure 2.6: Typical Feynman diagrams for SM production of four top quarks. Figures (a) and (c) are taken from Ref. [38], figure (b) is taken from Ref. [3].

2.3.2 Four-Top-Quark Production in BSM Models

Measuring the SM contribution to the four-top-quark final state could also give hints about BSM theories. A measured cross section larger than expected from the SM could be an indication for a BSM contribution. Because of its large mass, the top quark could also have a large coupling to new particles similar to its large coupling to the Higgs boson.

One approach to search for such particles, is to look for new resonances. In typical resonance searches, a new particle would be produced from a quark-antiquark-pair and would then decay to a pair of a top quark and an antitop quark as shown in Figure 2.7(a). However, this production mode would be suppressed if the resonance does not couple or only weakly couples to the light quarks. A resonance that couples predominantly to the top quarks is referred to as top-philic resonance. At leading order, such a resonance would be produced in association with another top quark pair, leading to a final state of four top quarks. The according Feynman diagram is shown in Figure 2.7(b).

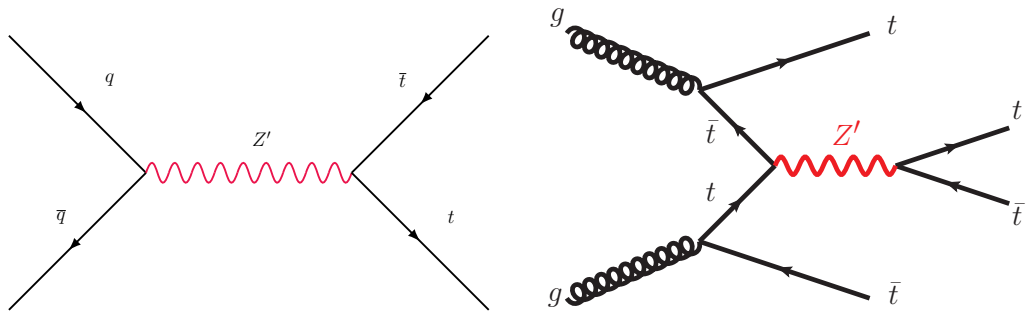

(a) Resonance production through light quarks.

(b) Resonance production through top quarks.

Figure 2.7: Feynman diagrams for top quark pair produced from light quarks (a) and four top quark production (b).

A number of BSM models predict top-philic resonances. Two such BSM theories are briefly outlined in the following to exemplify how these resonances can arise when extending the SM. Detailed discussions of these theories lie outside the scope of this thesis.

Composite Higgs Models

In composite models, the SM is extended by a composite sector [39]. A global symmetry is assumed that is spontaneously broken at around TeV scale. This symmetry group needs to be large enough to produce at least four Goldstone bosons upon breaking. These four Goldstone bosons then form the Higgs doublet. The couplings between the composite sector and the elementary sector which contains the other SM fields are assumed to be linear [40]. As a consequence, the mass eigenstates are mixings of elementary and composite fields. The particle spectrum results from this mixing schematically written as

$$|SM_n\rangle = \cos\alpha_n|\text{elementary}_n\rangle + \sin\alpha_n|composite_n\rangle, \tag{2.45}$$

$$|Heavy_n\rangle = -\sin\alpha_n|\text{elementary}_n\rangle + \cos\alpha_n|composite_n\rangle, \tag{2.46}$$

where α_n is the mixing angle for each particle. The mass hierarchy of the flavor sector is therefore turned into a mixing hierarchy. In the SM, the Higgs couples to the other SM particles through Yukawa couplings giving the fermions their masses. If the Higgs is composite, these are replaced by Yukawa couplings to the composite states that appear in the mixing. Small Yukawa couplings and therefore small masses of the light SM particles correspond to small compositeness fractions $\sin\alpha_n$. The top quark has large compositeness, corresponding to its large mass. As the compositeness of the third generation quarks is high they can have strong couplings to the new heavy quarks.

Similarly, the mechanism giving rise to the vector bosons in the SM subgroup is now embedded in a higher order symmetry. Also the SM and additional heavy vector bosons are mixed states of the elementary and composite sector according to Eq. 2.45 and Eq. 2.46. The SM vector bosons are described by small compositeness. As the top quark has large compositeness it would couple more strongly to a new heavy resonance Z' than the lighter quarks. Such a heavy resonance could then be produced in association with another top quark pair resulting in the four-top-quark final state.

Two Higgs Doublet Model

The Two Higgs Doublet Model (2HDM) belongs to the group of BSM models with an extended Higgs sector. In the 2HDM it is assumed that there exist two Higgs doublets instead of one, leading to four additional Higgs bosons: another scalar H, a pseudoscalar A and the charged Higgs bosons $H^\pm$ [41]. The Higgs boson corresponding to the SM one is denoted as h. The extension of the Higgs sector is close to the so-called alignment limit in its parameter space [42]. This ensures that h has the properties of the SM Higgs boson.

Following the parametrization used in Ref. [41], the model can be described with nine free parameters. The four physical masses $\{m_h, m_H, m_A, m_{H^\pm}\}$ are free parameters of the model. By requiring two Higgs doublets, one also obtains two vacuum expectation values of the form

$$\langle\phi_1\rangle = \frac{1}{\sqrt{2}}\begin{pmatrix} 0 \\ v_1 \end{pmatrix}, \quad \langle\phi_2\rangle = \frac{1}{\sqrt{2}}\begin{pmatrix} 0 \\ v_2 \end{pmatrix}. \tag{2.47}$$

The ratio $\tan\beta = \frac{v_1}{v_2}$ and the mixing angle α which diagonalizes the mixing matrix of m_h and m_H are free parameters as well. Finally, the couplings $\lambda_{5,6,7}$ which are used to describe the coupling g_{Hhh} complete the set of free parameters in the chosen parametrization of the model. The alignment limit can be realized through specific choices of these parameters.

The couplings of the additional scalar H to the SM vector bosons V can be defined in terms of α and β as

$$g_{HVV} = \cos(\beta - \alpha), \quad g_{hVV} = \sin(\beta - \alpha). \tag{2.48}$$

A Higgs boson h corresponding to the SM one is realized if g_{HVV} is small and $g_{hVV} \to 1$. The alignment limit is therefore approached if $\cos(\beta - \alpha) \to 0$. As

$$\cos(\beta - \alpha) \sim -\frac{\lambda_6}{(m_H^2 - m_h^2)^{\frac{1}{2}}}, \tag{2.49}$$

there are two possibilities to achieve $\cos(\beta - \alpha) \to 0$. The first possibility is decoupling [43], in which case H, A and $H^{\pm}$ are much heavier than the Higgs boson of the SM. In the decoupling limit, $m_H \sim m_A \sim m_{H^{\pm}}$ such that the effective Higgs theory is that of the SM. As a consequence, h has the properties of the SM Higgs boson.

The other possibility of realizing the alignment limit is if $\lambda_6 \to 0$ which can be obtained by imposing certain symmetry criteria on the scalar potential.

Hence, the couplings of the Higgs boson h observed at the LHC to the SM gauge bosons approaches unity $g_{hVV} \to 1$ in the alignment limit according to Eq. 2.48. The couplings of the additional Higgs bosons to the SM gauge bosons are in turn suppressed. The most common Higgs production modes at the LHC through Higgsstrahlung and Vector Boson Fusion (VBF) are therefore also suppressed for H. Searches similar to SM Higgs searches like $H \to ZZ$ therefore become ineffective for the new particles. For A, these production modes do not exist at all. Couplings to the fermions are generically unsuppressed, however. The productions in association with $b\bar{b}$ or $t\bar{t}$ therefore become more relevant. The $t\bar{t}$ final state does not offer ideal conditions due to large SM backgrounds and systematic effects to the reconstructed mass spectrum. These can be avoided when investigating the four-top-quark final state instead. The production mode is then similar to that of the SM production via Higgs $t\bar{t}H/A \to t\bar{t}t\bar{t}$ where it is kinematically required that $m_{H/A} \gtrsim 2m_t$.

2.3.3 Simplified Model for a Color-Singlet Top-Philic Resonance Z'

When comparing particle physics data to a BSM model, simplified models are often used in the interpretation instead of full models as introduced in the previous section. The simplified model only describes the extension of the SM which is necessary to specify the process under study. With this approach, only a limited number of new free parameters such as the mass of a new particle are introduced. A simplified model is therefore chosen for the analysis to describe a top-philic resonance as presented in Ref. [44] and Ref. [45]. In this model, it is assumed that the resonance couples exclusively to the top quark. The resonance mass $m_{Z'}$, its coupling strength to the top quarks c_t and the mixing angle θ are free parameters of this model. The resulting Lagrangian to describe the only relevant interaction is:

$$\mathcal{L}_{int} = \bar{t}\gamma_\mu(c_L P_L + c_R P_R) t Z'^\mu \tag{2.50}$$

$$= c_t \bar{t}\gamma_\mu(\cos\theta P_L + \sin\theta P_R) t Z'^\mu \tag{2.51}$$

with the projection operators $P_{L/R} = (1 \mp \gamma_5)/2$ where γ_5 is the fifth Pauli matrix and $c_t = \sqrt{(c_L^2 + c_R^2)}$ is defined through the left- and right-handed components of the coupling strength.

The mixing angle θ is defined by $\tan\theta = \frac{c_L}{c_R}$.

The decay width of the resonance is then:

$$\Gamma(Z' \to t\bar{t}) = \frac{c_t^2 m_{Z'}}{8\pi}\sqrt{1 - \frac{4m_t^2}{m_{Z'}^2}}\left[1 + \frac{m_t^2}{m_{Z'}^2}(3\sin 2\theta - 1)\right] \tag{2.52}$$

$$\approx \frac{c_t^2 m_{Z'}}{8\pi} \quad \text{if} \quad m_t \ll m_{Z'}. \tag{2.53}$$

At leading order, the largest contribution to the production cross section of the resonance is the production in association with a top quark pair through the strong interaction. The resonance can also be produced in association with a light quark through the weak interaction or with a W boson through mixed strong and electroweak interaction. Sample diagrams for the Z' production modes are shown in Figure 2.8.

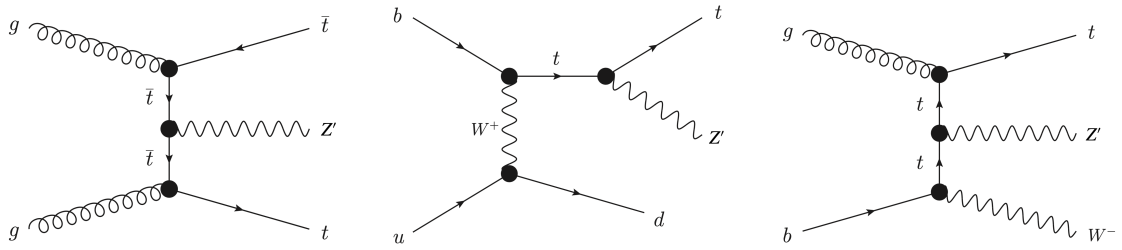

(a) Z' production with $t\bar{t}$. (b) Z' production with tj. (c) Z' production with tW.

Figure 2.8: Tree level production modes of the resonance Z'. Figures taken from Ref. [44].

The production of the resonance in association with tj or tW strongly depends on the chirality parameter θ. The dependence is caused by the t-W-b interaction which is part of both of these production modes. For the Z' production in association with tj or tW, $\theta = 0$ corresponds to the purely left-handed interaction leading to the largest cross section. The case $\theta = \pi/2$ corresponds to the purely right-handed interaction with the smallest cross section. The production in association with a top quark pair on the other hand does not include the t-W-b interaction and is independent of θ. Additional small contributions to the resonance production in association with $t\bar{t}$ and tW arise from the t-channel production mode as shown in Figure 2.9. For the production in association with $t\bar{t}$ and a resonance with a mass of 1.5 TeV, this contribution increases the cross section by about 10 %.

Contributions from loop-induced production modes could contribute as well when higher orders are considered. Assuming the simplified model as discussed, a chirality parameter of $\theta = \pi/4$ would minimize the contribution of these loop-induced production modes. However, this only holds if other contributions of new physics such as couplings of the resonance to other particles do not exist. Since the considered model is defined to be a simplified model with a resonance that couples only to the top quarks, loop contributions in general are neglected in this analysis.

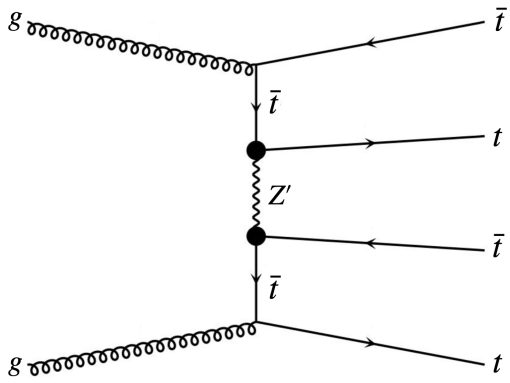

Figure 2.9: Feynman diagram for four-top-quark production via a BSM resonance Z' in the t-channel.

As this is the first analysis of its kind, the most simple choice is made for the signal model used in the first part of the model-dependent interpretation. In this case, the Z' resonance is assumed to be produced only in association with a top quark pair and loop-induced production modes are neglected. The narrow-wdith approximation can be applied for the chosen coupling of the resonance to the top quarks $c_t = 1$. The described simplified model will be referred to as $t\bar{t}Z'$ model.

For the second part of the model-dependent interpretation, the t-channel for the resonance production with $t\bar{t}$ as well as the production in association with tj or tW of the resonance are included. Multiple values of c_t for $\theta = 0$ and $\theta = \pi/2$ are considered in this case.

CHAPTER 3

Collider Physics

On the basis of the theoretical framework, interactions between particles can be described. The resulting predictions from the SM and BSM models can then be compared to the measured observables to test whether they can be confirmed. At particle colliders, higher energies can be achieved than in fixed target experiments which allows to study heavy particles. Important quantities to describe interactions at particle colliders are introduced in this chapter. When colliding proton beams, additional effects need to be taken into account which are also discussed. The different steps carried out in simulations to describe the interactions within colliders are presented. A summary of the different concepts presented in this chapter can be found in Ref. [46].

3.1 Collider Physics Quantities

In this section, the relevant concepts and quantities for the description of proton-proton collisions are discussed. In proton collisions, higher energies can be achieved as compared to electron positron collisions. The higher mass of the protons leads to a smaller energy loss due to synchroton radiation which allows to reach higher energies in the collisions. As protons are constituent particles, one needs to consider the hard scattering processes between their constituents in collisions. Additionally, activity arises from the remaining parts of the proton and the hadronization of the quarks.

3.1.1 Center-of-Mass Energy

The center-of-mass energy describes the combined energy of the collided particle beams. It is defined as the square root of the Mandelstam variable [47]

$$s = (p_1 + p_2)^2, \tag{3.1}$$

where p_1 and p_2 are the four-momenta $p = (E, \vec{p})$ of the two particles. For a collider experiment with two beams that have opposite sign and equal magnitude momentum as well as the same energy, the resulting center-of-mass energy is

$$\sqrt{s} = 2E. \tag{3.2}$$

When elementary particles are collided, for example at an e^+e^--collider, this energy translates directly into the energy available to produce other particles in the collision. When colliding protons, the available energy is less than the center-of-mass energy due to the compositeness of the proton.

3.1.2 Parton Distribution Function

The parton model [48] can be used to describe interactions in hadron collisions. The constituents of the hadrons are referred to as partons which are held together by their interactions. Each parton carries a fraction of the proton's momentum given by the Bjorken-x variable

$$x = p_{\text{parton}}/p_{\text{proton}}. \tag{3.3}$$

The momentum of partons is distributed according to Parton Distribution Functions (PDFs). The PDF $f_a(x_a, \mu_F, \mu_R)$ describes the probability of a parton a to carry the momentum fraction x_a at factorization scale μ_F and renormalization scale μ_R. The factorization scale separates the hard scattering processes of the partons and the interplay of the hadron constituents. The renormalization scale defines the energy at which the energy-dependent strong coupling g_s is evaluated. A typical choice is to set μ_F and μ_R to the energy scale Q of the process and denote the PDF as $f_a(x_a, Q^2)$. The PDFs are obtained by parametrizing their non-perturbative part and fitting these parameters with experimental data. The Dokshitzer–Gribov–Lipatov–Altarelli–Parisi (DGLAP) evolution equations [49–51] are then used to define the PDF at higher values of Q^2.

3.1.3 Cross Section

The cross section σ of the process under study describes the likelihood of a specific final state. According to the factorization theorems [52], the cross section can be expressed as a product of the partonic interaction cross section and the distribution of the partons within the protons. One can then express the cross section of a process $pp \to X$ of two protons i and j as

$$\sigma_{pp\to X} = \sum_a \sum_b \int \mathrm{d}x_a \mathrm{d}x_b f_{a/i}(x_a, Q^2) f_{b/j}(x_b, Q^2)\, \sigma_{ab\to X} \tag{3.4}$$

in terms of the PDFs $f_{a/i}(x_a, Q^2)$ and $f_{b/j}(x_b, Q^2)$ as well as the partonic cross section $\sigma_{ab\to X}$. The partonic cross section can be obtained from the matrix element $\mathcal{M}_{ab\to X}$ as

$$\sigma_{ab\to X} = \int \mathrm{d}\Omega |\mathcal{M}_{ab\to X}|^2(\Omega, Q^2), \tag{3.5}$$

by integrating over the full solid angle Ω. The matrix element $\mathcal{M}_{ab\to X}$ corresponds to the scattering amplitude of the process to occur which can be obtained from the Feynman diagram. The cross section $\sigma_{ab\to X}$ can be expressed perturbatively in a power series in $\alpha_s = \frac{g_s^2}{4\pi}$. The Feynman

diagrams are the pictorial representations of the terms in the power series describing the matrix elements.

3.1.4 Luminosity

The predicted number of events for a specific process can be compared to the number of observed events to test a theory. The number of events per time unit can be expressed in terms of the instantaneous luminosity $\mathcal{L}$ and the cross section of the studied event $\sigma_{pp\to X}$ as [53]

$$\frac{dN_{\text{events}}}{dt} = \mathcal{L}\sigma_{pp\to X}, \tag{3.6}$$

The luminosity can be defined in terms of beam parameters where the beams are split into bunches as

$$\mathcal{L} = \frac{N_b^2 n_b f_{\text{rev}} \gamma}{4\pi \varepsilon_n \beta^*} F, \tag{3.7}$$

where N_b is the number of particles per bunch, n_b is the number of bunches per beam, f_{rev} is the revolution frequency, γ is the Lorentz factor and ε_n is the normalized transverse beam emittance. The beta function β^* describes the transverse size of the beam at the interaction point (IP). The geometric luminosity reduction factor F corrects for the crossing angle at the IP.

The total number of events is then obtained by computing the integrated luminosity

$$N_{\text{events}} = \int \mathcal{L} dt \sigma_{pp\to X}. \tag{3.8}$$

3.2 Principles of Monte Carlo Event Generation

The previously introduced quantities are computed using simulation software. The cross section $\sigma_{pp\to X}$ of a certain process has to be computed by integrating the amplitudes $|\mathcal{M}_{ab\to X}|^2$ of the different contributing Feynman diagrams of the underlying partonic processes at all orders. Depending on the process, large numbers of diagrams may need to be considered which can be computationally challenging. Furthermore, some intermediate states cannot be calculated analytically by perturbative expansion. The integration is therefore carried out by applying the Monte Carlo (MC) method. Here, the basic approach is to compute integrals by throwing random numbers and determine what fraction of these numbers lies inside the area enclosed by a certain function. For the cross section integrals, the enclosed area is the multi-dimensional integration phase space. The more random numbers are generated, the higher the accuracy. Pseudo-random numbers are typically used for reproducibility.

The full simulation chain resulting in the final state particles is then referred to as MC event generation. Large numbers of events are typically generated to model the processes as accurately as possible. However, it remains an approximation. The simulated events should not be taken

as absolute truth and the need for corrections of the simulated events to better describe the data are expected. Nevertheless, MC event generation is an invaluable tool to make estimations about high-energy collision processes.

The simulation can be split into several steps from the hard scattering to the resulting final states which corresponds to the factorization introduced in the definition of the cross section. A pictorial representation of the simulation process is shown in Figure 3.1. The different steps are described in this section, following Ref. [46].

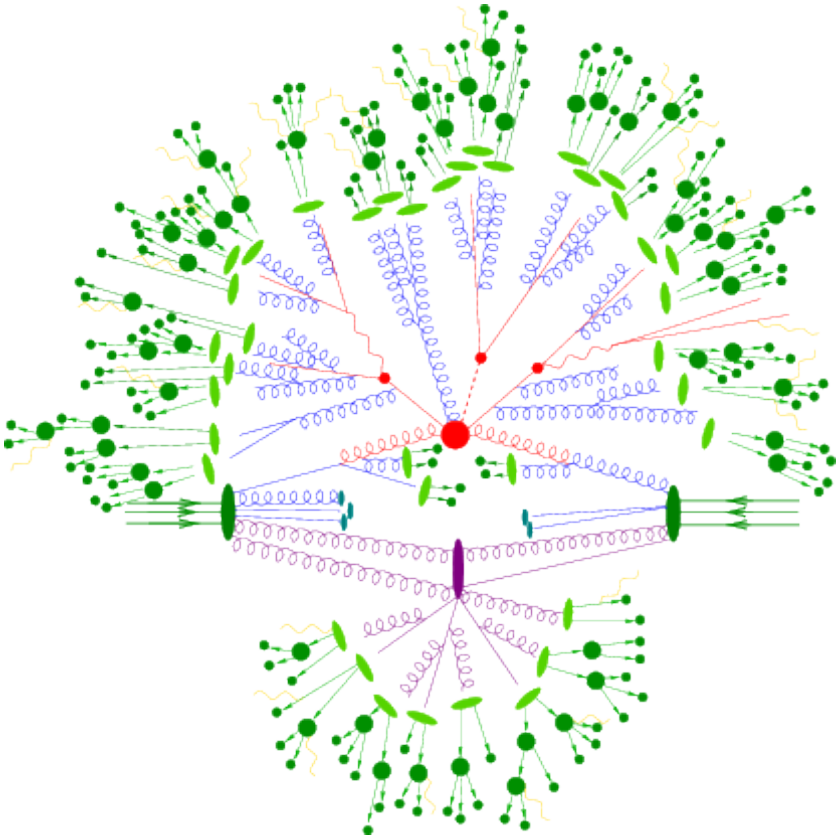

Figure 3.1: Sketch of MC event generation. The hard interaction is shown in red with the primary interaction depicted by the large red blob and the following decays shown as smaller red blobs. A secondary interaction is shown in purple. The hadronization of partons is shown in light green and decays of hadrons in dark green. Photon radiation is represented by the yellow lines. Figure taken from Ref. [54].

3.2.1 Hard Scattering

The first step is the computation of the event cross section also known as matrix element computation. Different orders in α_s of Feynman diagrams are computed. Tree-level Feynman diagrams describe Leading Order (LO) processes. Feynman diagrams with extra loops increase precision to Next to Leading Order (NLO) or to next-to-next-to-leading-order (NNLO). Additional radiations are also taken into account. The cross section is then computed as described in Section 3.1.3 assuming the

parton model. The total cross section corresponding to a process is obtained by convoluting the computed cross section and the PDF according to Eq. 3.4.

3.2.2 Parton Shower

At hadron colliders, not all final state particles are produced directly in the hard scattering processes. Parton showering (PS) describes the procedure of consecutively adding particles to the production process to model the full final state arising from a collision. Starting with a $2 \rightarrow 2$ process for the hardest partons, additional parton branchings are successively added. The parton showering describes the energy flow of the event but does not alter the production cross section. Parton branchings occurring before and after the QCD interaction vertex are called initial and final-state parton showers. An ordering is introduced to determine at what point of time a certain parton showering has taken place. For example, an ordering in p_{T} can be chosen. The parton showering process is ended by a parton shower cutoff. Due to the composite nature of the proton, multiple interactions at parton level can take place when two protons collide. These additional interactions are regularized by a cutoff in p_{T}.

3.2.3 Hadronization

The last step is the hadronization, where the partons are combined into observable hadrons. The partons cannot be observed directly due to confinement in QCD but instead form bound states. One of two different models is typically used for this step. In the Lund model, pairs of quarks and antiquarks are assumed to be connected by a string. The potential energy stored by that string increases when the quark and antiquark move away from each other. The system then breaks when the energy is large enough, resulting in two pairs of quarks and antiquarks. If the potential energy increases further, additional such breaks can occur. The process ends if there is not enough energy to form additional hadrons. The model cannot predict the kind of hadrons produced.

In the cluster model, all gluons are split into quark and antiquark pairs. Color neutral clusters are formed by neighbouring pairs. The clusters then decay into two hadrons. The available energy and properties of the quarks determine the type of the hadron.

After the hadron formation through either of the two models, the hadrons can then decay further depending on their lifetimes.

Sketches illustrating the concepts embodied in the two models are shown in Figure 3.2.

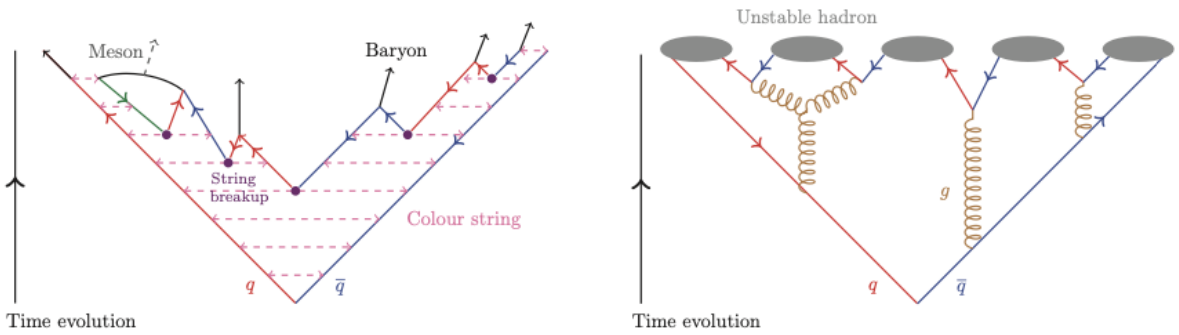

Figure 3.2: Lund hadronization model (left) and cluster hadronization model (right). Figure taken from Ref. [46].

3.3 Simulation Software

The concepts of event simulation introduced before are realized in many different software tools. A brief summary of the most commonly used tools is given here.

3.3.1 Examples of MC Event Generators

Many different event generators exist which are optimized for varying purposes. A few examples of common generators which are currently used for modeling high energy physics processes are given here.

PYTHIA [55] is one of the most widely used multi-purpose generators. It applies the Lund hadronization model and a parton shower ordering in p_{T}. Many efforts were put into optimizing this generator and tailoring it to describe the data collected at hadron colliders as accurately as possible [56].

HERWIG (Hadron Emission Reactions With Interfering Gluons) [57] is another multi-purpose generator. It applies the cluster hadronization model and an angular parton shower ordering.

SHERPA (Simulation of High-Energy Reactions of PArticles) [58] automatically merges LO or NLO matrix element results with its own parton shower model. It thus offers an alternative approach to describe the parton showering.

MADGRAPH [59] is a multi-leg matrix element generator. It has been integrated with aMC@NLO which computes matrix elements at NLO. Since it generates matrix elements, it needs to be interfaced with a PS generator.

POWHEG (POsitive Weight Hardest Emission Generator) [60] provides NLO computations. It needs to be interfaced with a PS generator.

3.3.2 Detector Simulation

The results of the MC event generators do not take into account any effects of the detectors. These effects need to be simulated as well to be able to compare the resulting simulated events with data. A specific simulation of the detector that was used to collect the data is therefore necessary. A simulation of the detector response is carried out after the event generation. The underlying principle is again the MC method. The different parts of the detector are modeled with geometric objects. The interactions of the particles with the detector material, the electric and magnet fields are simulated. The different hadronic and electromagnetic interactions need to be described with designated models. Hadrons interacting with the detector material produce secondary hadrons which in turn produce more hadrons. The modeling of these hadron showers is especially time and resource consuming.

GEANT 4 (GEometry ANd Tracking) [61] provides a very detailed simulation of the interactions inside detectors. It therefore also needs a large amount of computing time and resources.

Fast Simulation Programmes reduce the needed time and resources by using frozen showers instead of recreating the showers for each particle. An example for such a fast simulation programme is Altfast [62] where approximations are made for the geometry and description of hadronic showers. The even simpler approach of a parametrized detector simulation is applied in DELPHES [63].

The next step is digitisation. Hits denoting the interactions of the particles with the detector material are translated into electronic signals from the detector. Dedicated setups in the simulation programmes were developed to model the response of particular detectors that are currently used in particle physics experiment.

CHAPTER 4

The Large Hadron Collider and the ATLAS Detector

The theoretical predictions are tested by comparing them to experimental data. The data is collected with detectors at particle colliders. The Large Hadron Collider (LHC) and the ATLAS detector are presented in this chapter. The reconstruction of the different physics objects from the detector signals is discussed. An overview of the major upcoming upgrade of the LHC and ATLAS is presented which will allow for even larger data sets to be collected.

4.1 The Large Hadron Collider (LHC)

The LHC [64] is the largest particle accelerator in the world. At the LHC, proton and ion beams can be collided. It is located at the European Organization for Nuclear Research (CERN) close to Geneva, Switzerland. It replaced the Large Electron Positron collider (LEP) [65] using the same tunnel which is located up to 175 m below ground level. First collisions at the LHC started in 2008. The LHC has a circumference of 26.7 km and so far reached a center-of-mass energy of up to 13 TeV. Instantaneous luminosities of up to $2 \times 10^{34}\,\mathrm{cm}^{-2}\mathrm{s}^{-1}$ have been achieved at the LHC. There are two beams going in opposite direction in the LHC which are bent and focused by a large number of superconductive magnets. The beams are collided in four interaction points. At these four points, the four large LHC experiments are positioned: ATLAS (A Toroidal LHC ApparatuS) [66], CMS (Compact Muon Solenoid) [67], ALICE (A Large Ion Collider Experiment) [68] and LHCb (Large Hadron Collider beauty) [69]. Of these four experiments, ATLAS and CMS are multi-purpose detectors, targeting a large variety of physics phenomena. ALICE is specifically designed for recording the collisions of ion beams. LHCb is designed to optimally study b-physics. In addition, there are several smaller experiments at the LHC targeting more specific physics purposes.

The LHC is part of the CERN accelerator complex. The beam energy is successively increased in different accelerators before the beams are injected into the LHC. A sketch of the full accelerator chain is shown in Figure 4.1. The beams are split into bunches of 1.1×10^{11} protons.

In the proton source, hydrogen gas is stripped of its electrons using electric fields to obtain

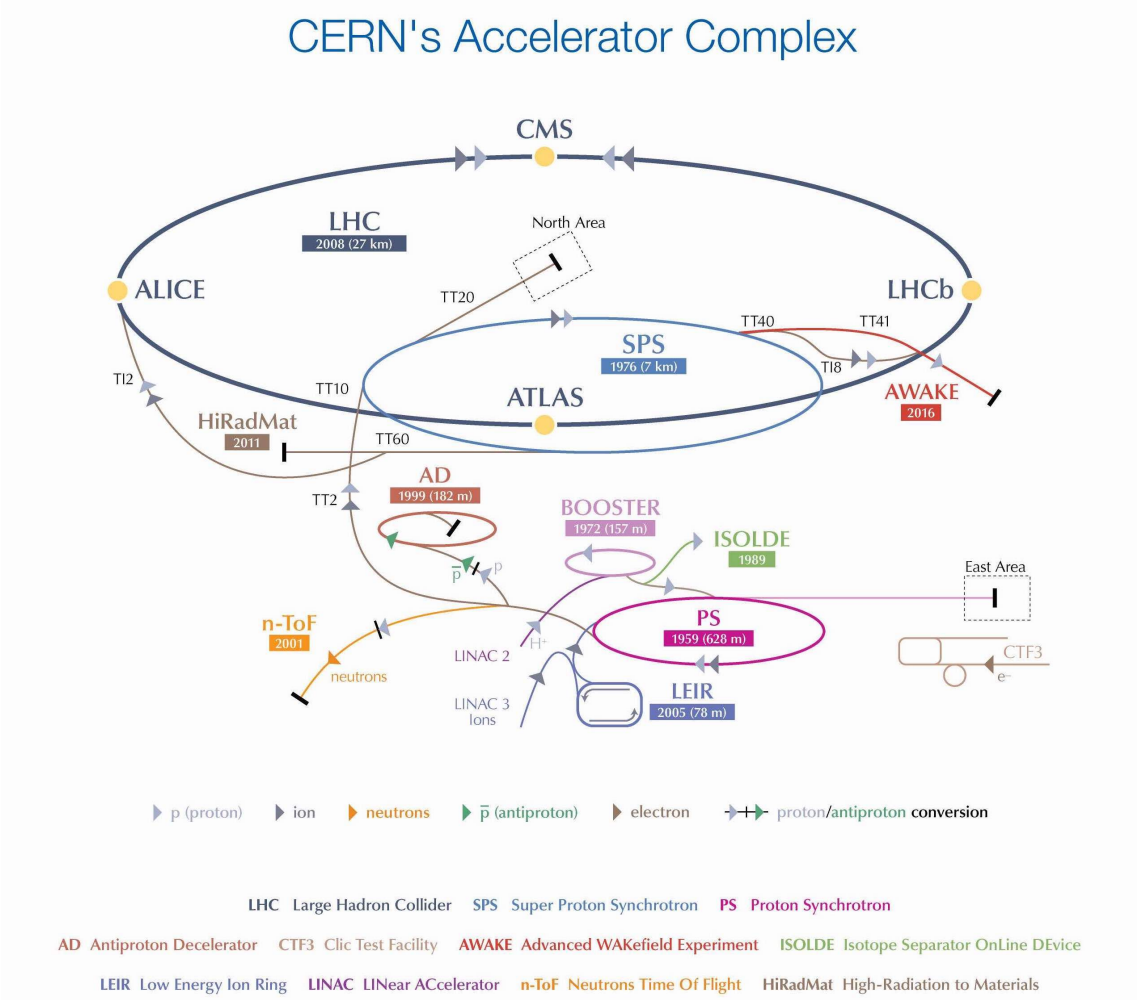

Figure 4.1: The accelerator complex of the LHC. Figure taken from Ref. [70].

the protons. The proton beams are then accelerated by the linear accelerator LINAC2 to 50 MeV. Next, the Proton Synchrotron Booster (PSB) accelerates them further to 1.4 GeV. In the Proton Synchrotron (PS), the energy is increased to 25 GeV and the bunches are produced in LHC spacing of 25 ns. In the Super Proton Synchrotron (SPS), they are further accelerated to 450 GeV. Three to four cycles of the PS are needed to fill the SPS. The beams are then injected from the SPS into the LHC where the final energy of 6.5 TeV per beam is reached. It takes 12 cycles of the SPS to fill the LHC. The minimum time required to increase the energy from 450 GeV to 6.5 TeV is about 20 min.

Several periods of data taking, so called runs, take place at the LHC. In between runs, detector and accelerator upgrades are carried out. The runtimes are summarized in Table 4.1 showing the years when the LHC ran or will run, the center-of-mass energy and the integrated luminosity. The target values for the upcoming Run 3 and High Luminosity (HL) phase [71, 72] are shown as well.

Run Number	Years	Center-of-Mass Energy [TeV]	Luminosity [fb^{-1}]
1	2009-2013	7, 8	30
2	2015-2018	13	140
3	2022-2026	13.6	300
HL	2029-	14	3000

Table 4.1: Summary of the LHC runtimes with corresponding center-of-mass energy and luminosity.

4.2 The ATLAS Detector

One of the four large particle detectors at the LHC is the ATLAS detector. A detailed description of it can be found in Ref. [73]. It has a cylindrical geometry and is 46 m long with a diameter of 25 m. It is located 100 m below ground and weighs 7 000 t. Different layers of detector subsystems are concentrically built around the collision point of the particle beams at the center of the detector to measure particle trajectories and their properties. Large magnets bend the paths of charged particles to measure their momenta with high precision. A schematic overview of the ATLAS detector is shown in Figure 4.2.

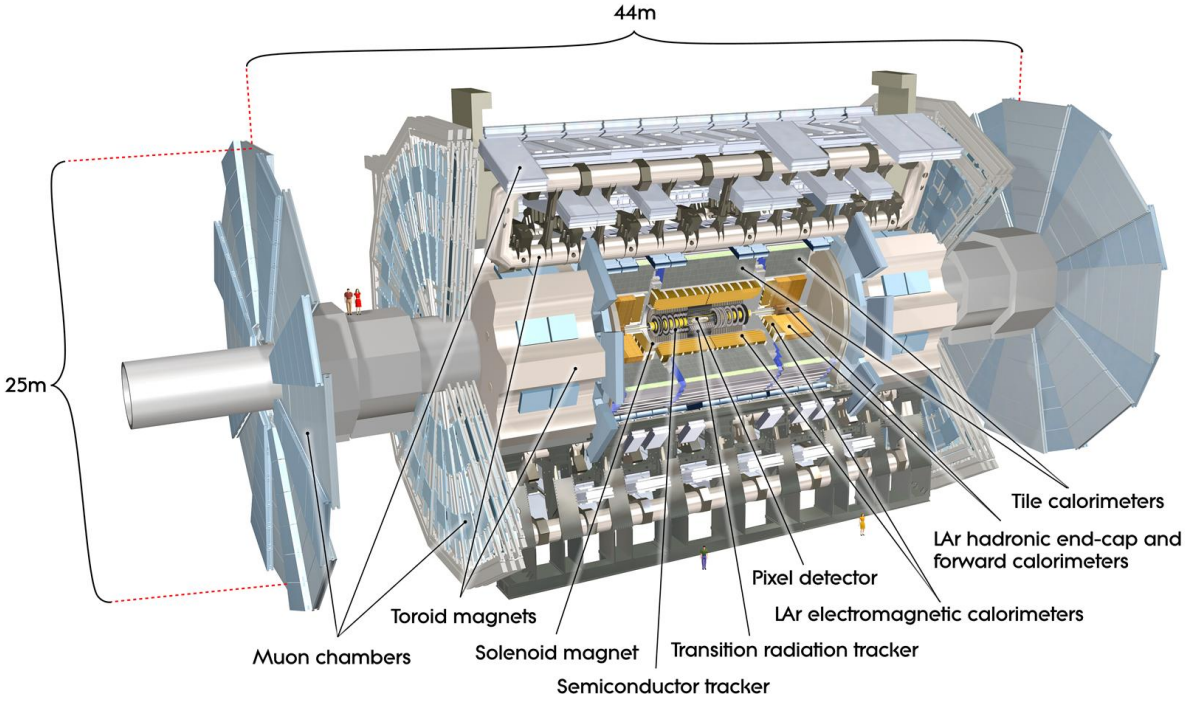

Figure 4.2: Schematic overview of the ATLAS detector. Figure taken from Ref. [73].

4.2.1 Coordinate System

A right-handed coordinate system is used to describe the ATLAS detector and the particles observed with it. The nominal interaction point is located at the origin of the coordinate system. The z-axis follows the beam line, the positive x-axis points towards the center of the LHC and the positive y-axis points upwards. The azimuthal angle ϕ is measured around the beam axis and the polar angle θ is measured from the beam axis. The pseudorapidity η is defined as $\eta = -\ln\tan(\theta/2)$ and the distance ΔR as $\Delta R = \sqrt{\Delta\eta^2 + \Delta\phi^2}$. The transverse momentum p_{T} is defined orthogonal to the beam axis.

4.2.2 Inner Detector

The inner detector (ID) surrounds the interaction point and measures tracks of charged particles with high momentum resolution. The cylindrical ID covers the region $|\eta| < 2.5$. It is surrounded by a solenoid magnet providing a magnetic field of 2 T. Around the interaction point, the ID consists of concentrical cylinders. In the forward and backward regions, it consists of disks perpendicular to the beam line which form the endcap regions. A schematic overview of the inner detector of ATLAS is shown in Figure 4.3.

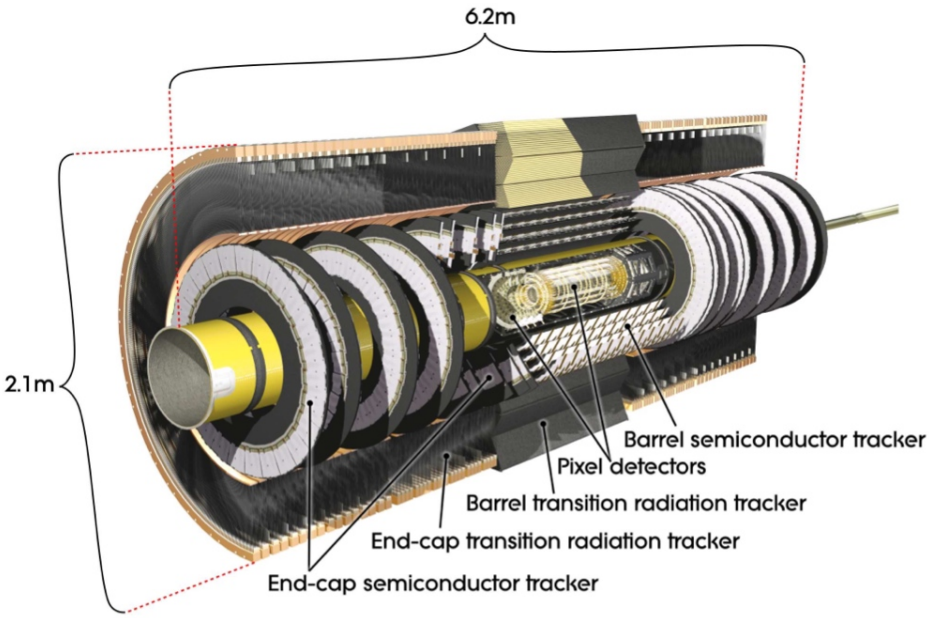

Figure 4.3: Schematic overview of the different subsystems of the ATLAS inner detector. Figure taken from Ref. [73].

The ID consists of three subsystems which complement each other. They are used for pattern recognition and reconstruction of particle tracks with high momentum resolution. The innermost subdetector consists of silicon pixel layers. With about 80.4 million readout channels it achieves

a high accuracy of 10 µm in the R-ϕ-direction and 115 µm in the z-direction. The pixel layers are surrounded by the SemiConductor Tracker (SCT) made of multiple silicon microstrip layers. Each particle track crosses 8 strip layers. The total number of SCT readout channels is about 6.3 million. Outside of these layers, there is the Transition Radiation Tracker (TRT) which consists of layers of 4 mm diameter gaseous straw tubes and transition radiation material [74]. When a charged particle traverses the radiation material made of polymer fibers or foils, transition radiation is created which is larger for electrons than for hadrons as it depends on the particle mass. The transition radiation leads to additional energy deposited in the gas which results in higher readout signals. The TRT is therefore used for electron identification. It also contributes to the tracking with an average of 36 hits per track, further enhancing pattern recognition and increasing momentum resolution. The obtained information in R-ϕ-direction has an accuracy of 130 µm. In the barrel region, the straws are 144 cm long and positioned parallel to the beam line. In the endcap region, the straws are 37 cm long and are arranged radially in wheels. The total number of readout channels of the TRT is about 351.000. The lower precision of each individual straw tube compared to the silicon detectors is compensated by a large number of measurements, large track lengths and timing information from the wire signals.

4.2.3 Calorimeter System

The ID is surrounded by the calorimeter system. It consists of different subsystems which are optimised for the measurement of different physics processes, covering almost the full solid angle up to $\eta < 4.9$. The different subsystems of the ATLAS calorimeter are shown in Figure 4.4.

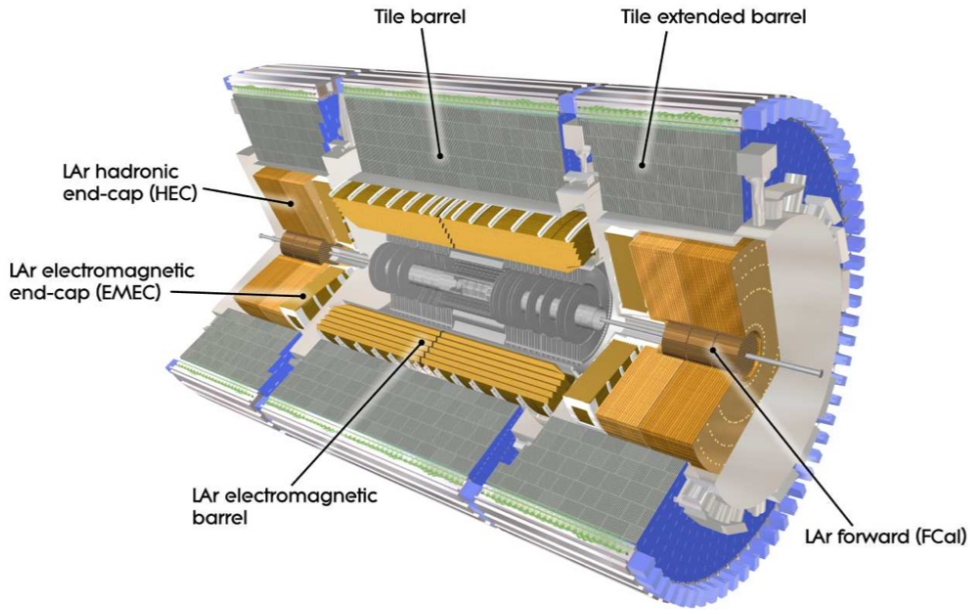

Figure 4.4: Schematic overview of the ATLAS calorimeter system. Figure taken from Ref. [73].

The electromagnetic (EM) calorimeter is the innermost part of the calorimeter. It has a high granularity over the same range $|\eta| < 2.5$ which is also covered by the ID which allows for very precise measurements of electrons and photons. The other parts of the calorimeter have a coarser granularity which suffices for jet reconstruction and $E_{\mathrm{T}}^{\mathrm{miss}}$ measurements which are discussed below.

The EM calorimeter is split in a barrel region ($|\eta| < 1.475$) and endcap regions ($1.375 < |\eta| < 3.2$). It is positioned outside of the central solenoid. The EM calorimeter is a lead-LAr (Liquid Argon) detector with kapton electrodes and lead absorber plates.

Outside of the EM calorimeter is the hadronic tile calorimeter. It is split into a barrel region covering $|\eta| < 1.0$ and the extended barrel regions $0.8 < |\eta| < 1.7$. It is made of scintillating tiles which are each read out at two sides by wavelength shifting fibres in two photomultiplier tubes.

The hadronic endcap calorimeter is positioned behind the electromagnetic endcap calorimeter. It is a LAr detector and consists of two wheels per endcap. Material gaps between subsystems are avoided by slight overlaps of the hadronic endcap calorimeter with the tile calorimeter, covering ranges up to $|\eta| = 1.5$. Similarly it extends up to $|\eta| = 3.2$, overlapping with the forward calorimeter which covers regions up to $|\eta| = 3.1$. Each wheel consists of 32 wedge-shaped modules which are made of copper plates interleaved with LAr.

The forward calorimeter (FCal) is located close to the beamline in forward and backward regions. It consists of three layers: one copper layer for electromagnetic measurements and two tungsten layers for measuring the energy of the hadrons. The electrodes are composed of concentric tubes and rods with LAr in between.

4.2.4 Muon System

The core principle of the Muon Spectrometer (MS) is the bending of the muon tracks due to the magnetic field of the toroid magnets. In the range $|\eta| < 1.4$, the large barrel toroid supplies the relevant magnetic field. In the range $1.6 < |\eta| < 2.7$, two smaller endcap magnets mainly provide the magnetic field. In between, a combination of both magnet types affects the magnetic bending of the paths. The three toroids each consist of 8 coils arranged radially and symmetrically around the beam axis. The resulting magnetic field is mostly orthogonal to the muon trajectories. Different subsystems are used to detect the muons in the barrel and endcap regions. The muon subsystems and magnets are shown in Figure 4.5. In the barrel region, there are three layers of concentric cylindrical detector layers.

In the endcap region, there are three layers perpendicular to the beam line. The muon tracks are measured by Monitored Drift Tubes (MDTs) over most of the η range. In the range $2 < |\eta| < 2.7$, Cathode Strip Chambers (CSCs) are used. These are multiwire proportional chambers where the cathodes are split into strips. The CSCs have higher granularity than the MDTs to withstand the high rate. Additionally, there are trigger chambers in the range $|\eta| < 2.4$. In the barrel region, these are Resistive Plate Chambers (RPCs) which have a high time resolution. In RPCs, a homogeneous electric field with high field strength is achieved in the gas chamber by adding plates of high electrical resistance to the insides of the electrodes. In the endcap region, Thin-Gap Chambers (TGCs) are used which are multi-wire chambers with a distance of 1.4 mm between the anode wire and the cathode plane. The trigger chambers provide p_{T} thresholds and measure the muon coordinate

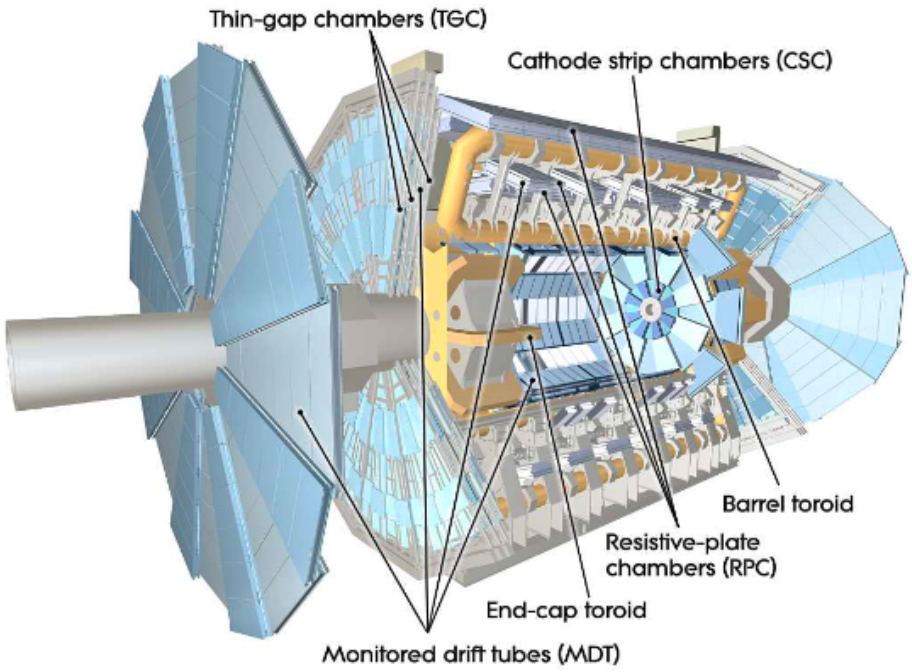

Figure 4.5: Schematic overview of the ATLAS muon system. Figure taken from Ref. [73].

orthogonal to that measured in the tracking-chambers.

4.2.5 Forward Detectors

The ATLAS forward region is covered by three additional forward detectors. LUCID (LUminosity measurement using Cerenkov Integrating Detector) is positioned at ±17 m from the interaction point. It measures the luminosity by detecting p-p-scattering in the forward region, making it the main online relative-luminosity monitor for ATLAS. ALFA (Absolute Luminosity For ATLAS) is located at ±240 m and measures pp elastic scattering at small angles. The ZDC (Zero-Degree Calorimeter) measures the centrality in heavy-ion collisions and is located at ±140 m.

4.2.6 Trigger and Data Acquisition System

The Trigger and Data Acquisition (TDAQ) system filters and stores the events detected at ATLAS. The TDAQ consists of multiple subsystems associated with different detector subsystems. Because of the large number of collisions taking place, not all of the resulting events can be saved. Instead, events containing potentially interesting physics need to be identified. The other events are filtered out. The ATLAS trigger system for Run 2 consists of two levels [75]. With each level, the choice of events passing the trigger level is further refined and additional selections applied. The data from the detector read out electronics arrives at a rate of 40 MHz and is reduced to 1 kHz for recording.

The Level-1 (L1) trigger is hardware based and uses information from the calorimeter and muon detectors. It reduces the rate to 100 kHz within a latency of 2.5 µs. Information provided by the muon spectrometer and the calorimeters is combined by the central trigger processor to make a trigger selection. The event data for an event accepted by the L1 trigger is read out by the front-end electronics. It is processed by the readout system and sent to the second stage of the trigger. Additionally, regions of interest (RoI) are defined by L1. These are η-ϕ-regions where interesting features were identified. Information about the RoI's type of feature and the criteria which were passed are stored. The RoIs are the investigated further by the second trigger stage. The High Level Trigger (HLT) is the software-based second stage of the trigger system. A combination of algorithms is used for the final selection including fast trigger algorithms for early rejection and more precise algorithms which require more computing power. Within the algorithms event-data fragments from within the RoIs are requested and a hypothesis algorithm is used to decide whether the trigger conditions are satisfied. The output rate of the HLT is on average 1.2 kHz and the throughput to storage 1.2 GB s^{-1}. The events passing the event filter are then stored at the CERN data center.

4.3 Object Reconstruction

The raw detector signals are then used to reconstruct basic physics objects: the tracks, vertices and topological clusters of calorimeter energy deposits. As a next step, these basic objects are converted into physics objects corresponding to the particles or particle signatures: photons, electrons, muons, jets and missing energy. This section describes the objects which are used in the search for heavy Z' resonances in four-top-quark final states. The objects can be identified with the final state particles of the physics process under study.

4.3.1 Basic Objects

The basic objects are the ingredients for the reconstruction algorithms to build physics objects. They describe specific patterns in the data recorded by the detectors.

Tracks

Charged particles leave hits in the different layers of the ID. Collectively, these hits describe the trajectory of the particle. Different algorithms are used to reconstruct the tracks originating from primary and secondary charged particles [76]. The inside-out algorithm is used for the reconstruction of primary charged particles. These are particles that are directly produced in pp-collisions or are decay products of very short-lived directly produced particles. The inside-out algorithm uses three hits in the silicon detectors as seeds. Moving away from the interaction point, hits are then added using a combinatorial Kalman filter [77]. Ambiguities in the track candidates are resolved and the tracks are extended into the TRT. The resulting tracks are required to have $p_{\mathrm{T}} > 400$ MeV.

In a second stage, back-tracking is applied. Back-tracking is used for secondary charged particles, which are decay or interaction products of primary charged particles. Segments reconstructed with

the TRT are used as starting points which are extended inwards to match silicon hits.

Vertices

Vertices describe points where particles interact or decay. They are identified with an iterative vertex finding algorithm [76]. The z-position of a track at the beamline is used as seed for the vertex algorithm. Vertices are required to contain at least two tracks. An iterative χ^2 fit is used to evaluate the compatibility of a vertex seed and a track. If the corresponding standard deviation is larger than 7σ, the track is considered as a new vertex seed. The algorithm continues until no further additional vertices can be found.

Topological Cluster

The basic objects measured by the calorimeters are clusters of topologically connected calorimeter cell signals (topo-clusters) [78]. They are used to reconstruct hadrons, jets and hadronically decaying τ-leptons. Topo-clusters are also used to represent the energy flow from softer particles needed to reconstruct the missing energy $E_{\mathrm{T}}^{\mathrm{miss}}$. The algorithm used to reconstruct the topo-clusters makes use of the spatial distribution of signals in order to gain information about the direction, location and shape of the cluster. If only individual cells are hit without seeing a similar signal in the neighbouring cells, these hits are considered to be noise and are discarded.

The seeds used in the topo-cluster algorithm are selected by requiring a signal significance above a certain threshold. These seeds are then considered to be proto-clusters. All neighbouring cells which again satisfy a minimum signal efficiency are then added to the proto-cluster. If a cell is matched to two proto-clusters, the proto-clusters are merged. This process is continued until all neighbouring cells with sufficient signal efficiency are matched to a proto-cluster. These three stages of topo-cluster formation are visualized through simulation in Figure 4.6.

If a proto-cluster has two or more local signal maxima, it is split according to these maxima. Here, a local signal maximum is defined as $E_{\mathrm{cell}}^{\mathrm{EM}} > 500\,\mathrm{MeV}$. Additionally, the cell is required to have at least four neighbouring cells with no neighbouring cell having a larger signal. Multiple local maxima indicate the presence of multiple close-by particles. Separating these clusters gives higher resolution information and allows to distinguish close-by particles.

4.3.2 Electrons

Electrons loose energy when traversing the detector material due to bremsstrahlung. Photons are radiated off in this process which again can produce electrons and positrons through pair production. Because of their common origin, these electrons, positrons and photons are often reconstructed as one electromagnetic cluster due to their spatial proximity. Consequently, multiple tracks can be identified with the same primary electron.

A sketch of the path of an electron through the ATLAS detector is shown in Figure 4.7. Electrons are reconstructed from charged-particle tracks in the ID and EM topo-clusters. The tracks need to be matched to the clusters in the $\eta \times \phi$ plane [79]. The reconstruction can be split into several steps.

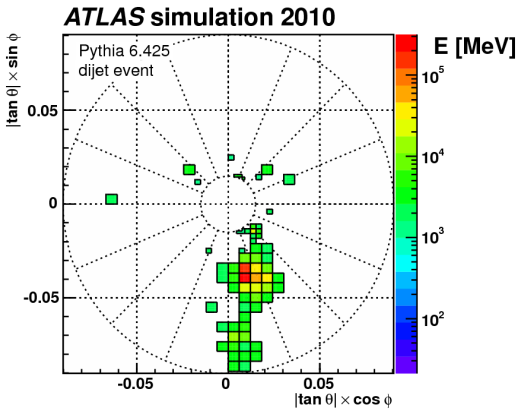

(a) Seeds passing the first signal efficiency criterion.

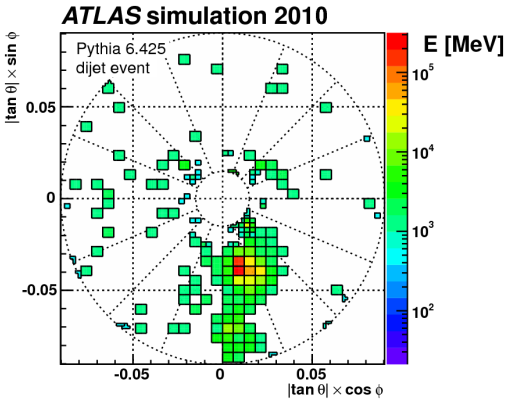

(b) Proto-clusters passing the second signal efficiency criterion.

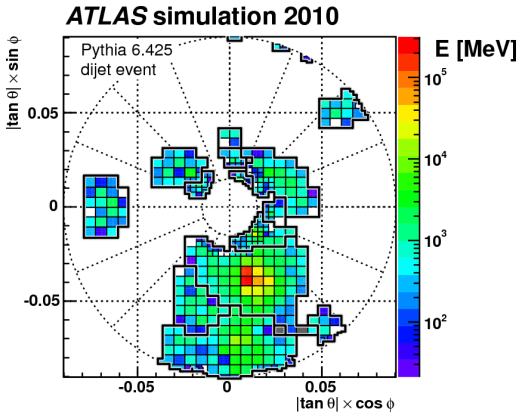

(c) All topo-clusters after merging.

Figure 4.6: Steps of topo-cluster formation. (a) First, the seeds are selected by requiring a signal efficiency above a certain threshold. (b) Next, proto-clusters are formed by adding neighbouring cells to the seed which again satisfy a signal efficiency criterion. (c) Final topo-clusters after having added all neighbouring cells with sufficient efficiency. Figure taken from Ref. [78].

Seed-Cluster Reconstruction

The first step is to reconstruct seed clusters. The EM calorimeter is split into 200 × 256 towers in the $\eta \times \phi$ space consisting of the three layers of the EM calorimeter. The energy of such a tower is the summed energy of the three layers in that area. EM energy clusters are seeded from collections of 3×5 towers in $\eta \times \phi$ with a combined energy larger than 2.5 GeV. Using a sliding window algorithm [80], the center of the seed is moved to identify local energy excesses. This process is performed on every element of the calorimeter. If two seeds are found close to each other, the one with the higher total energy is kept if their energy difference is larger than 10 %. If their energy difference is less than 10 %, the candidate with the highest central tower is kept.

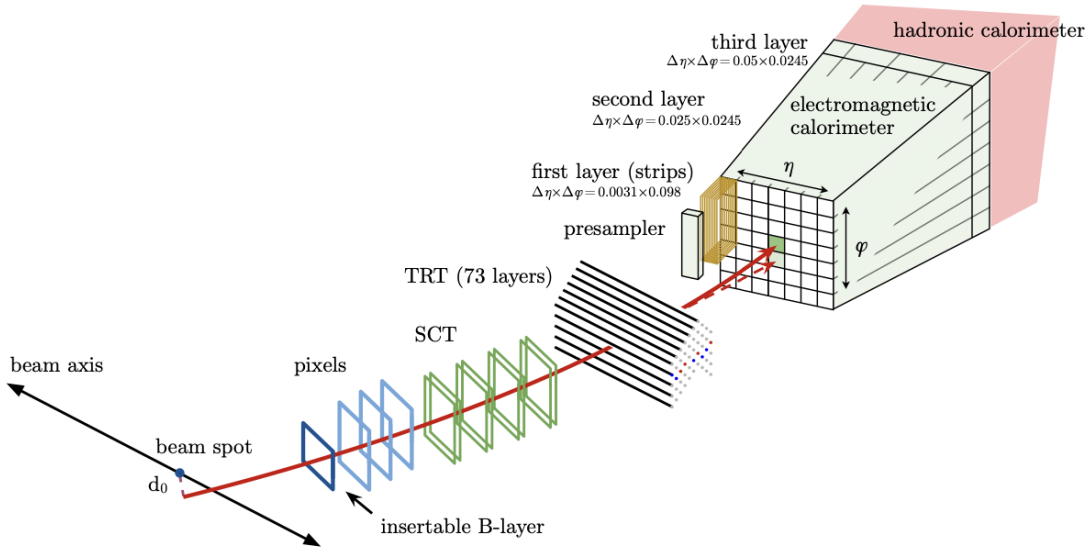

Figure 4.7: Sketch of the path of an electron through the ATLAS detector. It first passes the pixel detector, the SCT and the TRT. It then enters the calorimeter. The red dashed line indicates a photon which is radiated off by the electron. Figure taken from Ref. [79].

Track Reconstruction

Multiple hits of charged particle in the ID are collected in clusters for reconstruction in the pixel and SCT detectors. Three-dimensional objects called space-points are then created out of the clusters. Three space-points in the silicon-detector layers are combined into a track seed. Energy losses due to bremsstrahlung are taken into account by the means of pattern recognition. After that, a Gaussian-sum filter (GSF) [81] is applied to the clusters to combine the effects of energy loss and the track measurements. Only tracks with at least four silicon hits which are loosely matched within $|\Delta\eta| < 0.05$ and $-0.20 < \Delta\phi < 0.05$ to an EM cluster are used in this step.

Electron-Candidate Reconstruction

The final step is to combine the EM seed cluster and the GSF-track candidate. The matching requirement in ϕ is slightly tightened to $-0.10 < \Delta\phi < 0.05$. If there are several tracks that fulfil this criterion, the primary electron track is chosen with a dedicated algorithm. This algorithm takes into account the distance in η and ϕ of the tracks and the cluster barycenters in the second layer of the calorimeter as well as the number of hits in the silicon detectors. If the primary electron is matched to a secondary vertex and has no hits in the pixel detector, it is likely a converted photon and categorized as such.

Electron Identification

A likelihood-based (LH) identification including tracking and calorimeter information is used to select prompt electrons in the central region of the detector ($\eta < 2.47$). This identification allows to discriminate electrons against other objects with similar signature, electrons from photon conversion and non-prompt electrons coming from hadron decays. The LH identification also allows for correct identification of prompt electrons that would fail a cut-based selection due to a single criterion.

LH-Identification Working Points

Different working points are defined for the LH-identification which meet different criteria on signal efficiency and background rejection. The so-called *Loose*, *Medium*, and *Tight* operating points are defined to provide 93 %, 88 %, and 80 % reconstruction efficiency for an electron with $E_{\mathrm{T}} = 40\,\mathrm{GeV}$, respectively. For these three operating points, at least two hits in the pixel detector are required as well as seven hits in the pixel and silicon-strip detector combined. For the *Medium* and *Tight* operating points, the innermost pixel layer must have been hit. The electron identification efficiency for the different working points as function of E_{T} are measured using the well-understood benchmark processes $J/\Psi \to ee$ and $Z \to ee$. The electron identification efficiency for different operating points is shown in Figure 4.8.

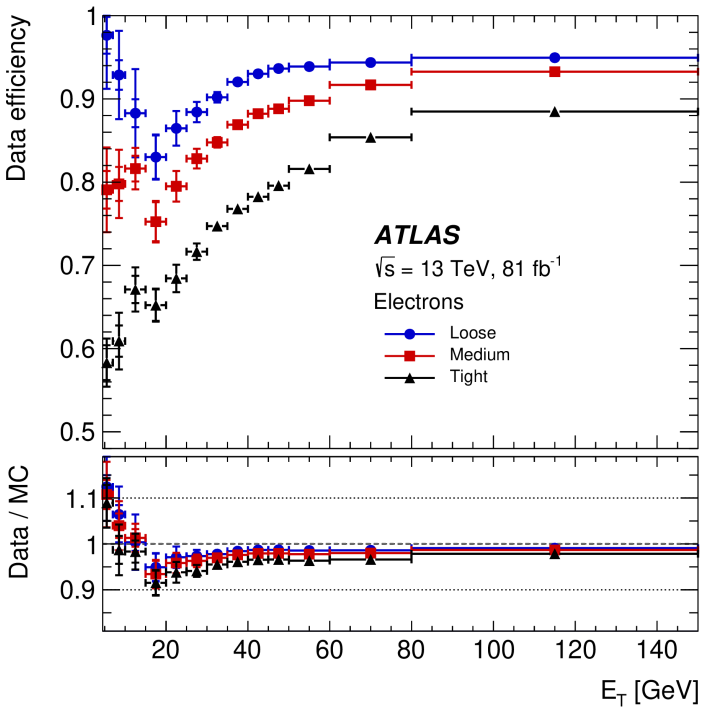

Figure 4.8: The electron identification efficiency for the different working points as function of E_{T}. Figure taken from Ref. [82].

Electron Isolation

An electron candidate also needs to be differentiated from other processes such as misidentified hadrons or photons converting into e^+e^--pairs. An electron can be distinguished from other processes through isolation. The electron candidate is required to meet isolation criteria of little activity in a surrounding $\Delta\eta \times \Delta\phi$ region around the potential electron. The amount of such activity can be determined by using topo-clusters or tracks. When using topo-clusters, the transverse energy of calorimeter clusters is measured within a cone of radius ΔR around the electron candidate excluding itself. In the track-based approach, the activity surrounding the electron candidate is determined by summing the transverse momenta of tracks aligning with that of the electron candidate excluding itself. The energy or momentum of the electron candidate is then subtracted from the full energy or momentum of the cone to obtain the isolation variables $E_{\mathrm{T}}^{\mathrm{iso}}$ and $p_{\mathrm{T}}^{\mathrm{iso}}$. Three operating points are defined for the isolation. The isolation efficiency is defined as the number of electrons passing the isolation criteria divided by the number of identified electrons. For the *Loose* working point, a fixed value of isolation efficiency is targeted, uniform in E_{T} and η. For *Gradient* isolation, an isolation efficiency dependent on E_{T} but uniform in η is targeted. For *Fixed* isolation, fixed values for the isolation variables are chosen.

4.3.3 Muons

Muon reconstruction is performed by combining information from the ID and the MS. The reconstruction of muons in the ID is equivalent to that of other charged particles which has been described before. Therefore, only the reconstruction with information from the MS [83] will be described in the following.

Muon Reconstruction in the MS

First, hit patterns in the muon chambers are identified which form muon track segments. Segments in different layers are then combined into muon track candidates. A segment can be shared by multiple tracks and is then either removed or identified as a shared segment by an overlap removal algorithm. The hits are fit to the track with a global χ^2 fit. If the resulting χ^2 satisfies the selection criteria, it is accepted. Otherwise, the hits with large contributions to the χ^2 are removed and the fit is repeated.

Combined Muon Reconstruction

The reconstruction is then performed based on ID and MS information leading to four categories of muons:

- *Combined (CB) muons*: Tracks reconstructed in the ID and the MS are combined in a global fit where MS tracks can be added or removed if that increases the fit quality. The tracks are usually first reconstructed in the MS and then extended inward.

- *Segment-tagged (ST) muons*: If a track reconstructed in the ID is matched to a local track segment of the MDT or the CSC, it is considered a muon. This type is used if the muon only crosses one MS layer.
- *Calorimeter-tagged (CT) muons*: If a track reconstructed in the ID is matched to an energy deposit of a minimum-ionizing particle in the calorimeter, it is considered a muon. This type is used for areas of the MS where it is not instrumented well.
- *Extrapolated (ME) muons*: The only requirement for this type is that it is loosley matched with the interaction point using the MS track. This type is usually used for the range $2.5 < \eta < 2.7$ which the ID does not cover.

Overlaps between the different types are removed by prioritizing CB muons, followed by ST and CT muons. Overlaps with ME muons are removed based on the better fit quality of the track using the corresponding hits.

Muon Identification

Prompt muons which originate from hard scattering processes are distinguished from muons originating from kaon and pion decays by certain quality criteria. The background muons from kaon and pion decays can often be identified by a "kink" in the ID where the hadron decays. Several variables based on ID and MS measurements of muon properties like p_{T} offer good discrimination between prompt and background muons. Additionally, certain numbers of hits are required in the different sub-detectors. Four muon identification categories with varying degrees of selection efficiency and background rejection are defined:

- *Medium muons*: For this selection, only CB and ME muon tracks are used. This selection reduces uncertainties originating from reconstruction and calibration. ID and MS momentum measurements need to be compatible according to a loose selection to suppress misidentified hadrons. This is the default selection in ATLAS.
- *Loose muons*: For this selection, all muon types are used. It is optimized for the reconstruction of a Higgs boson decaying to four leptons and to maximize reconstruction efficiency.
- *Tight muons*: For this selection, CB muons with hits in at least two MS stations that also satisfy the *Medium* selection criteria are used. It maximizes the purity of the muons.
- *High-p_T muons*: For this selection, CB muons with hits in at least three MS stations that also satisfy the *Medium* selection criteria are used. It maximizes the momentum resolution for tracks with $p_{\mathrm{T}} > 100\,\mathrm{GeV}$ and was optimized for direct searches of hypothetical Z' bosons.

Muon Isolation

The techniques used to select isolated muons are similar to those employed for electrons. An isolation variable based on the track $p_{\mathrm{T}}^{\mathrm{iso}}$ is defined as well as an isolation variable based on the calorimeter $E_{\mathrm{T}}^{\mathrm{iso}}$. There are seven muon isolation working points which are optimized for different requirements of the analyses: *LooseTrackOnly*, *Loose*, *Tight*, *Gradient*, *GradientLoose*, *FixedCutTightTrackOnly* and *FixedCutLoose*. They are defined based on different criteria on the isolation variables.

4.3.4 Jets

Quarks and gluons cannot be observed individually with particle detectors due to color confinement. Instead, they form bound states as color-neutral hadrons and initiate a shower of particles (see Section 3.2.2). The corresponding signature in particle detectors is called a jet. The basic principle is to collect the signals of the different hadrons in one object and associate that with the quark or gluon the hadrons originated from. The jets allow to connect the signatures that can be measured with the detector with the quarks and gluons from the hard scattering processes. This translation requires a good jet calibration to correctly reconstruct the processes, including an accurately determined Jet Energy Scale (JES) as well as high angular and energy resolutions [84].

Since protons are collided at the LHC, jets are very important objects for identifying certain signals of interest. In addition, they also contribute to the backgrounds that analyses have to take into account.

Pileup

At the high luminosities that are reached at the LHC, an effect called pileup plays an important role. It describes the presence of multiple interactions which are associated to one bunch crossing. Additional contributions are typically soft and have to be separated from the hard interaction of interest. Pileup interactions are grouped into two categories. When additional proton-proton collisions apart from the hard scatter interaction take place within one bunch crossing, these are called in-time pileup. Out-of-time pileup comes from energy deposits in the calorimeters from other bunch crossings.

Particle Flow Jets

Most analyses investigating the data collected in Run 1 of the LHC use so-called EM-topo jets which are reconstructed from topo-clusters corrected by a JES correction factor [85]. The particle flow (PFlow) jets which are now widely used are instead reconstructed with combined information from the tracker and the calorimeter. First, the energy from all charged particles is removed from the calorimeter. Particle objects are then created which consist of the remaining energy of the calorimeter and tracks matched with the interaction point of the hard scatter process. The jet reconstruction is then performed with these objects.

Using the particle flow objects which includes information from the tracker has several advantages. The resolution of the calorimeter energy in the center of the detector for energies and momenta in GeV is [86]

$$\frac{\sigma(E)}{E} = \frac{50\,\%}{\sqrt{E}} \oplus 3.4\,\% \oplus \frac{1\,\%}{E}. \tag{4.1}$$

The resolution of the inverse transverse momentum is

$$\sigma\left(\frac{1}{p_\mathrm{T}}\right) \cdot p_\mathrm{T} = 0.036\,\% \cdot p_\mathrm{T} \oplus 1.3\,\%. \tag{4.2}$$

The resolution of the tracker is therefore higher than that of the calorimeter for low energy particles. At high energy, the calorimeter resolution is higher. Including the tracker information in the reconstruction of jets can therefore increase their resolution.

In addition, softer particles that would not have passed the energy threshold of the calorimeter can be reconstructed with tracks. Furthermore, higher angular resolution can be achieved using tracker information. Also charged particles that originate from hadronic jets can be included in the reconstruction which would not reach the calorimeter because their paths are bent by the magnetic field. Finally, additional particles from pileup can be excluded by associating the tracks to vertices.

These different advantages motivate using information of the calorimeter and the tracker to reconstruct jets. In a particular reconstruction, either of the two measurements is used. However, every track needs to be associated with its corresponding calorimeter signal to avoid double counting. If a track measurement is used, the corresponding energy needs to be removed from the calorimeter. This is achieved with a cell-based energy subtraction algorithm.

The different steps of the PFlow algorithm are shown in Figure 4.9. These steps are applied to tracks ordered in decreasing p_T, starting with tracks with a single topo-cluster matched to it.

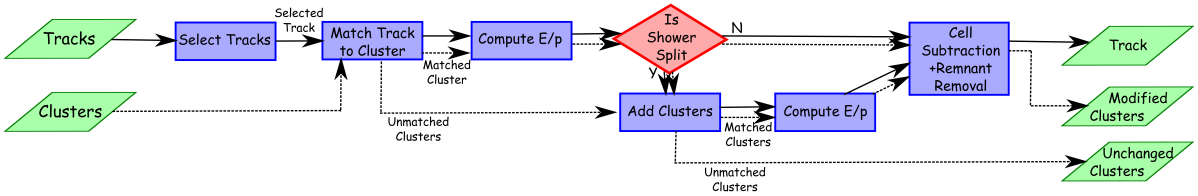

Figure 4.9: Different steps of the particle flow algorithm. More details about each step can be found in the text. Figure taken from Ref. [84].

At first, tracks are selected by requiring a number of criteria. As this algorithm is designed for hadronic tracks, tracks associated with an electron or muon are not selected. The selected tracks need to have at least nine hits in the silicon detectors and no hit at a position in the detector layers where one would be expected given the particle trajectory in the pixel detector [76]. The tracks further need to be within $|\eta| < 2.5$ and have $p_\mathrm{T} > 0.5\,\mathrm{GeV}$. If the tracks have $p_\mathrm{T} > 40\,\mathrm{GeV}$, they are excluded because such particles are typically not isolated from other particles. Isolation is however necessary to correctly subtract the energy in the calorimeter at a later step.

Next, the tracks are matched to single topo-clusters. For each topo-cluster the distances $\Delta\phi$ and $\Delta\eta$ between the track and the barycenter of the topo-cluster is computed and extrapolated to the second layer of the EM calorimeter. The distance metric defined as

$$\Delta R' = \sqrt{\left(\frac{\Delta\phi}{\sigma_\phi}^2\right) + \left(\frac{\Delta\eta}{\sigma_\eta}^2\right)} \tag{4.3}$$

is used to rank the topo-clusters. Here, σ_ϕ and σ_η are the angular widths of the topo-clusters defined as the standard deviation of the distance in ϕ and η of topo-cluster cells removed from the topo-cluster barycenter. These widths are affected by the granularity of the calorimeter and can therefore differ for different calorimeter subsystems. For the matching, a first requirement of

$$\frac{E^{\text{clus}}}{p_{\text{T}}^{\text{trk}}} > 0.1 \tag{4.4}$$

is set for the ratio of the topo-cluster energy E^{clus} and the track momentum $p_{\text{T}}^{\text{trk}}$. Then, the preselected topo-cluster yielding the smallest $\Delta R'$ is matched to the track. In most cases for particles with $p_{\text{T}} > 5\,\text{GeV}$, this matching allows to find the correct topo-cluster for the track. If a track cannot be matched to a topo-cluster with $\Delta R' \leq 1.64$, it is assumed that this particle did not form a topo-cluster. Such tracks are collected in a list of tracks and no energy subtraction is performed.

After that, the algorithm computes the expected energy in the calorimeter from the track momentum and the position of the topo-cluster. The average energy deposited by a particle

$$\langle E_{\text{dep}} \rangle = p_{\text{T}}^{\text{trk}} \langle E_{\text{ref}}^{\text{clus}} / p_{\text{T, ref}}^{\text{trk}} \rangle \tag{4.5}$$

is used to subtract the energy in the calorimeter if the track is used for reconstruction. The expectation value $\langle E_{\text{ref}}^{\text{clus}} / p_{\text{T, ref}}^{\text{trk}} \rangle$ is estimated with dedicated single particle samples. These are samples of simulated events which describe the interactions of single particles while neglecting additional activity due to pileup. Using these samples, the energies of topo-clusters of $\Delta R = 0.4$ around the track which are extrapolated to the second layer of the EM calorimeter are summed up. These measurements are binned in η and p_{T} as well as the Layer of Highest Energy Density (LHED) to take into account the detector geometry.

It is possible that not all of the energy of a particle is deposited in one topo-cluster. The probability of having multiple topo-clusters associated with the same track is therefore computed. If necessary, more topo-clusters are added. The most common case is that two topo-clusters are matched to the same track.

Tracks with a single topo-cluster associated to it and tracks with multiple topo-clusters associated to it can be separated by computing the significance of the difference between the expected energy and the topo-cluster energy

$$S(E^{\text{clus}}) = \frac{E^{\text{clus}} - \langle E_{\text{dep}} \rangle}{\sigma(E_{\text{dep}})}. \tag{4.6}$$

Clusters with $S(E^{\text{clus}}) > -1$ typically contain the majority of a particle shower. If $S(E^{\text{clus}}) < -1$,

only clusters within $\Delta R = 0.2$ around the track position extrapolated to the second layer of the EM calorimeter are considered. However, the full energy is subtracted in the following step.

The energy in the calorimeter produced by the particle that created the track is then subtracted cell by cell. Clusters with $\langle E_{\text{dep}} \rangle$ larger than the total energy of the matched topo-clusters are simply removed. Otherwise, starting at the extrapolated track position in the LHED, rings are formed around it in η, ϕ space. These rings correspond to only one calorimeter layer and contain at least one calorimeter cell. They are then subtracted in decreasing energy density order. The process ends if the ring has more energy than what still needs to be removed to reach $\langle E_{\text{dep}} \rangle$. If that is the case, the energy of each cell in the ring is scaled down to the expected energy of the particle.

Finally, topo-cluster remnants are removed. It is assumed that the topo-cluster or topo-clusters were produced from a single particle if the energy in the remaining cells after subtraction is consistent with the width of the $E^{\text{clus}}_{\text{ref}}/p^{\text{trk}}_{\text{ref}}$ distribution. Consequently, the remaining energy is attributed to shower fluctuations and is removed. Otherwise, it is assumed that the topo-cluster system corresponds to multiple particles in close proximity. In this case, the remnant topo-clusters collected in the subtraction step are retained.

Jet Reconstruction

The resulting topo-clusters after the energy subtraction step and the selected tracks are used in a jet reconstruction algorithm. The tracks are selected by matching them to the vertex of the hard scatter event if $|z_0 \sin\theta| < 2\,\text{mm}$ where z_0 is the distance of the track to the vertex in z-direction. This condition removes tracks originating from pileup.

The reconstruction is typically carried out using the anti-k_t algorithm [87] with a radius parameter of 0.4. The anti-k_t algorithm belongs to a broader class of sequential recombination jet algorithms. The basic components for these algorithms are distances d_{ij} between pairs of jet candidates called protojets and distances between a protojet and the beam axis d_{iB}. They are defined as

$$d_{ij} = min(k^{2p}_{\text{T}i}, k^{2p}_{\text{T}j}) \frac{\Delta^2_{ij}}{R^2}, \tag{4.7}$$

$$d_{iB} = k^{2p}_{\text{T}i}, \tag{4.8}$$

where $\Delta^2_{ij} = (y_i - y_j)^2 + (\phi_i - \phi_j)^2$, R is the jet radius, $k_{\text{T}i}$ is the transverse momentum, y_i is the rapidity and ϕ_i is the azimuth angle of the particle. The parameter p determines the relative power of the energy versus Δ_{ij}. For the anti-k_t algorithm, $p = -1$. For each protojet obtained with the PFlow algorithm, the two quantities d_{ij} and d_{iB} are computed and the minimum of these d_{min} is determined [88]. If the minimum is a d_{ij}, the two protojets are merged into a new protojet. If the minimum is a d_{iB}, the protojet is moved to a list collecting the final jets. The process is repeated until no protojet remains. A notable feature of the anti-k_t algorithm is its resilience towards soft contributions, resulting in exclusive sensitivity of the jet shape to hard particles.

Jet Calibration

The jets produced with the anti-k_t algorithm need to be calibrated to account for effects like pileup or energy contributions that were missed by the detector [89]. The calibration is based on MC simulated particles called truth particles that can be matched to the reconstructed jets by requiring $\Delta R < 0.3$ between the two objects. The different steps of the jet calibration for $R = 0.4$ anti-k_t jets are shown in Figure 4.10.

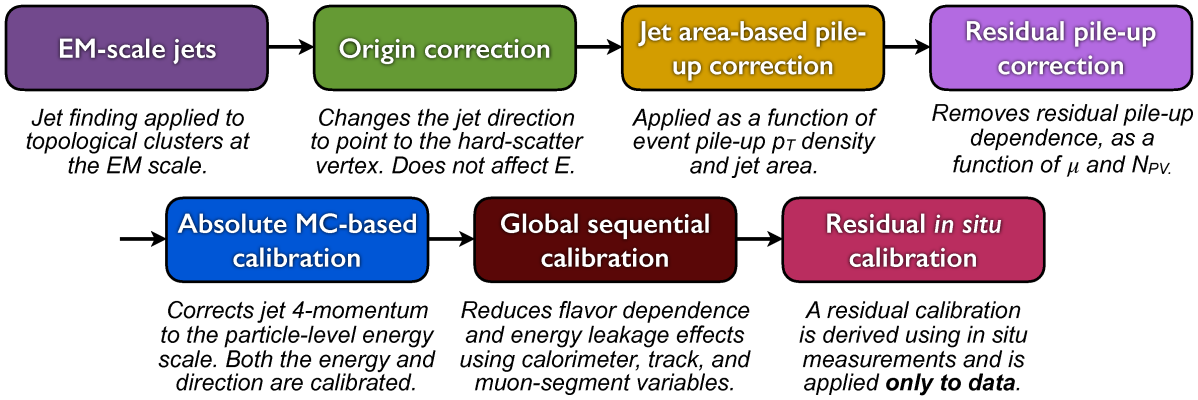

Figure 4.10: Steps of the jet calibration of $R = 0.4$ anti-k_t jets. More details about each step can be found in the text. Figure taken from Ref. [84].

The first step of the calibration is origin correction. The sum of four momenta of the constituents of the jet is corrected for constituents of the jet that are displaced from the corresponding hard-scatter vertex. This correction mainly improves the pseudorapidity resolution as the beam spread is larger along the beamline than in the transverse direction. The energy of the jet remains unchanged.

The next step is pileup correction. The pileup contribution is estimated per jet and per event as product of the event p_{T}-density ρ and the jet area A in (η, ϕ)-space. The jet area is calculated with FastJet 2.4.3 [90] and is approximately πR^2 for the almost conical jets produced by the anti-k_t algorithm. The pileup contribution ρA is then subtracted from the jet p_{T}.

After that, a MC-based JES calibration is applied to correct the reconstructed jet energy to the truth jet energy. A calibration function $c_{\mathrm{JES}}(E_{\mathrm{reco}}) = 1/\mathcal{R}(E_{\mathrm{reco}})$ as function of E_{reco} is computed in bins of the reconstructed η and the truth energy. The jet energy response $\mathcal{R}(E_{\mathrm{reco}}) = \langle \frac{E_{\mathrm{reco}}}{E_{\mathrm{truth}}} \rangle$ is obtained by a functional fit to the measured distribution of $\mathcal{R}$ for each value of E_{truth}. After the correction is applied, the calibration function is computed again. Three such iterative corrections are necessary to achieve optimal closure.

Next, the Global Sequential Calibration (GSC) characterizes fluctuations in the jet particle content arising from different production modes using calorimeter and tracker information. A correction to the jet response depending on any variable x that affects the jet response can be carried out, such as the number of tracks associated to a jet. A correction of the form $c(x) = k/R(x)$ is applied, where k is a constant ensuring that the jet energy remains unchanged and $R(x)$ is the jet response. These corrections are further parametrized in p_{T} and remove the dependence on x. Multiple such

corrections can be carried out sequentially. The resulting p_{T} is the product of the initial p_{T} and the corrections

$$p_{\mathrm{T}}^{\mathrm{GSC}} = p_{\mathrm{T},0} \prod_{j=1}^{N} c_j(p_{\mathrm{T},j-1}, x_j), \tag{4.9}$$

where $p_{\mathrm{T},0}$ is the p_{T} before the GSC.

The final step is the in situ calibration. The jet response and Jet Energy Resolution (JER) are computed and corrections between data and simulation are applied [91]. The residual correction factors for each η bin are obtained from data and simulations as $c = \mathcal{R}^{\mathrm{data}}/\mathcal{R}^{\mathrm{MC}}$. The p_{T} of the jet is corrected such that it is balanced against well-measured reference objects. The in-situ calibration consists of three steps, each focusing on a different p_{T} range. In the η-intercalibration the JES of forward jets with $0.8 < |\eta| < 4.5$ is corrected to that of central jets with $|\eta| < 0.8$. The Z/γ+jet balancing determines the recoiling jet response against a well-calibrated Z or γ of jets in the central region with p_{T} up to $\approx 950\,\mathrm{GeV}$. The multijet balancing calibrates central jets with$|\eta| < 1.2$ and $300\,\mathrm{GeV} < p_{\mathrm{T}} < 2\,000\,\mathrm{GeV}$ against well-calibrated low-p_{T} jets.

Identification of Jets Containing b-Hadrons

Jets containing hadrons that likely originated from a b-quark are important objects in many analyses for example in Higgs decays or for the identification of top quarks. The process of associating a jet with a b-quark is referred to as b-tagging. Different b-tagging algorithms are optimized for the conditions of different analyses. The b-tagging algorithm DL1r which is used in the analysis presented in this thesis is based on a deep neural network. It uses the outputs of a Recurrent Neural Networks (RNN) [92] as input variables. Using an RNN-based algorithm allows to make use of the correlations of different tracks associated with the same b-hadron.

The tracks used in the b-tagging algorithm are matched to jets when their distance ΔR is smaller than a certain p_{T} dependent value. They further need to fulfil $p_{\mathrm{T}} > 1\,\mathrm{GeV}$, $|d_0| < 1\,\mathrm{mm}$ and $|z_0 \sin\theta| < 1.5\,\mathrm{mm}$. In addition they need to have at least seven silicon hits, at most two silicon holes, and at most one hole in the pixel detector. A hole is a hit that was expected but is not present. There is no limit on the number of tracks. The following parameters enter the RNN:

- S_{d_0}: Lifetime signed transverse impact parameter significance defined as $S_{d_0} = d_0/\sigma d_0$. d_0 is the transverse displacement relative to the primary vertex and σd_0 its uncertainty. Its sign indicates whether the point of closest approach is in front (positive) or behind (negative) the primary vertex.
- S_{z_0}: Lifetime signed longitudinal impact parameter significance defined as $S_{z_0} = z_0/\sigma z_0$. d_0 is the longitudinal displacement to the primary vertex and σd_0 its uncertainty. Its sign indicates whether the point of closest approach is in front (positive) or behind (negative) the primary vertex.
- Category: tracks are categorized based on the numbers of observed, expected and missing hits in the layers of the silicon pixel and strip detectors.

- $p_{\mathrm{T}}^{\mathrm{frac}}$: Fraction of p_{T} carried by the track $p_{\mathrm{T}}^{\mathrm{track}}/p_{\mathrm{T}}^{\mathrm{jet}}$.
- ΔR(track, jet): Angular distance between track and jet $\sqrt{(\phi_{\mathrm{track}} - \phi_{\mathrm{jet}})^2 + (\eta_{\mathrm{track}} - \eta_{\mathrm{jet}})^2}$.

Of these parameters, the first three were already used in previous b-tagging algorithms used by ATLAS and the last two are added for the RNN approach.

The tracks are ordered in $|S_{d_0}|$ and this list is transformed into a fixed-size vector using a Long Short-Term Memory unit. A feed-forward fully-connected layer then gives the probability of a b-jet (p_b), c-jet (p_c) and light jet (p_u). The final discriminant DL1r is defined as [93]

$$\mathrm{DL1r} = \log\left(\frac{p_b}{p_c f_c + p_u(1 - f_c)}\right), \tag{4.10}$$

where f_c is the charm fraction which can be tuned for a trade-off between charm and light jet rejection.

Four working points are defined corresponding to the average efficiency: 70 %, 77 %, 80 % and 85 %.

Reclustered Jets

When particles like the W, Z, Higgs and the top quark have high p_{T} and decay hadronically, they create jets of a larger radius than those discussed previously. Reclustered (RC) jets are jets with a larger radius that are reconstructed from a collection of smaller radius jets [94]. The radius of an RC jet in the analysis presented in this thesis is $R = 1$, which captures a large fraction of the decay products of the heavy particle.

The RC jets are reconstructed with the anti-k_t algorithm using small radius jets $R = 0.4$ as inputs and a larger distance parameter. Uncertainties and calibrations are directly propagated from the small-R jets to the RC jets. Compared to large radius jets which are directly reconstructed from topo-clusters and tracks, the RC jets offer the possibility to optimize their size and grooming procedures.

The small-R jets considered for reclustering need to have $p_{\mathrm{T}} \geq 25\,\mathrm{GeV}$ and $|\eta| < 2.5$. After the RC jets are produced with the anti-k_t algorithm, they are trimmed. Small-R jets are removed from an RC jet if their transverse momentum is less than 5 % of the untrimmed RC's transverse momentum.

4.3.5 Taus

Tau leptons have a short lifetime of about 3×10^{-13} s [33]. At particle detectors, they are therefore identified by reconstructing their decay products [95]. For leptonically decaying taus, these are the electrons and muons which are reconstructed as described before. Hadronically decaying taus decay mainly into one or three charged pions. The typical signatures are therefore a narrow jet or a spray of particles in the calorimeter which can be associated with one or three tracks in the ID.

The anti-k_t algorithm is applied to obtain jets which are the starting points for the reconstruction of hadronic taus. A dedicated Tau Vertex Association algorithm is used to identify the vertex associated with the tau. Jets from taus are distinguished from other jets with an RNN [96]. It uses

information of reconstructed charged-particle tracks and energy clusters in the calorimeter which are associated to a tau candidate as inputs. Three working points *Loose*, *Medium* and *Tight* are defined according to the identification efficiency based on the RNN output.

4.3.6 Missing Transverse Momentum

In addition to the particles that were detected as described before, also the particles that escape detection hold valuable information. In the collision of the two proton beams, their combined momentum in the transverse plane is zero as they are moving along the z-axis prior to the collision. Due to momentum conservation, all outgoing particles combined should also have zero momentum in the transverse plane. Any imbalance arises from particles that could not be detected and is called missing transverse momentum. Its magnitude is referred to as missing transverse energy $E_{\mathrm{T}}^{\mathrm{miss}}$. Neutrinos cannot be detected directly because they only interact weakly and are neutral. Also particles that were out of acceptance contribute to the missing transverse momentum. It is furthermore an important observable in searches for new particles. A missing transverse momentum larger than expected could hint at new particles that escape direct detection because of their properties.

The missing transverse momentum is reconstructed using two components [97]. The first is the sum of energies of all prompt objects originating from the hard-scatter process. These are objects that are fully reconstructed and calibrated as discussed before. The second component consists of tracks that are matched to a vertex but not to any prompt object from the hard-scatter process. The x- and y-components of the transverse missing momentum is defined as

$$E_{\mathrm{x/y}}^{\mathrm{miss}} = -\sum_{i\in\{\text{hard objects}\}} p_{\mathrm{x/y},i} - \sum_{j\in\{\text{soft signals}\}} p_{\mathrm{x/y},j}, \tag{4.11}$$

where $p_{\mathrm{x/y},i}$ are the x- and y-components of the different p_{T} contributions. The magnitude $E_{\mathrm{T}}^{\mathrm{miss}}$ and direction ϕ^{miss} in the transverse plane are correspondingly

$$E_{\mathrm{T}}^{\mathrm{miss}} = \sqrt{(E_x^{\mathrm{miss}})^2 + (E_y^{\mathrm{miss}})^2} \tag{4.12}$$

$$\phi^{\mathrm{miss}} = \tan^{-1}\left(\frac{E_y^{\mathrm{miss}}}{E_{\mathrm{x}}^{\mathrm{miss}}}\right). \tag{4.13}$$

The entering detector signals need to be mutually exclusive to avoid double counting contributions. This is realized by a selection sequence and a rejection mechanism. The sequence is typically: electrons, photons, hadronically decaying taus and jets. Since muons are reconstructed from ID and MS tracks with associated calorimeter signals, they have little or no overlap with any of the other particles. If a lower priority particle shares the calorimeter signal with a higher priority particle, it is rejected.

Different selection criteria defined for different analyses affect the objects entering $E_{\mathrm{T}}^{\mathrm{miss}}$. The missing transverse momentum is in ATLAS therefore defined as the vectorial sum of the missing transverse energy terms from the different contributions

$$\mathbf{E}_T^{\text{miss}} = \underbrace{-\sum_e p_{\text{T}}^e - \sum_\mu p_{\text{T}}^\mu - \sum_\tau p_{\text{T}}^\tau - \sum_\gamma p_{\text{T}}^\gamma - \sum_j p_{\text{T}}^j}_{\text{hard term}} \underbrace{- \sum_{\text{soft}} p_{\text{T}}^{\text{soft}}}_{\text{soft term}}. \tag{4.14}$$

It can be recalculated in case selection criteria for the different objects change. Depending on the requirements of an analysis, different $E_{\text{T}}^{\text{miss}}$ working points are defined based on different requirements for jets [98]. The *Loose* $E_{\text{T}}^{\text{miss}}$ working point requires jets to have a $p_{\text{T}} > 20\,\text{GeV}$ and pass an additional set of jet criteria if $|\eta| < 2.4$ and $p_{\text{T}} > 60\,\text{GeV}$. For the *Tight* $E_{\text{T}}^{\text{miss}}$ working point, forward jets with $|\eta| > 2.4$ and $20\,\text{GeV} < p_{\text{T}} < 30\,\text{GeV}$ are excluded. The *Tight* selection reduces the pileup dependence of $E_{\text{T}}^{\text{miss}}$ since in that region there are more pileup jets than hard scatter jets.

4.4 LHC High Luminosity Phase and ATLAS Upgrade

The LHC will undergo a substantial upgrade after Run 3 to enable it to achieve higher luminosities. The High-Luminosity LHC (HL-LHC) [72] will start operation in 2029. It will reach a peak instantaneous luminosity of $7.5 \times 10^{34}\,\text{cm}^{-2}\text{s}^{-1}$. The aim is to reach at least $250\,\text{fb}^{-1}$ each year in ATLAS and CMS. The resulting integrated luminosity over the expected run time of 10 years is $3\,000\,\text{fb}^{-1}$. This upgrade will further extend the reach for potential discoveries at the LHC. A larger data set will allow for even higher precision in the measurements. It also opens up the possibility to search for very rare processes that could not be discovered with current data sets.

As introduced in Eq. 3.7, different beam parameters can be tuned to increase the luminosity. The beam intensity will be increased to 2.2×10^{11} protons per bunch. A reduction of the beta function value β^* will be achieved with stronger quadrupole magnets to focus the beam which reduces the transverse beam size. Reducing β^* will however lead to a larger crossing angle which in turn reduces the geometric luminosity reduction factor F. Crab cavities are used to mitigate this effect. They generate transverse electric fields which turn the beam, optimizing the overlap at the collision point. These modifications increase the number of proton-proton collisions per bunch crossing up to 200.

The main hardware upgrades of the LHC take place over a length of 1.2 km. The insertion regions around ATLAS and CMS will be almost completely replaced. New quadrupole magnets with the corresponding cooling and vacuum systems will be installed in these regions. Other major new features include the installation of the new cavities and new collimators. The beam injection and extraction systems will be modified and new beam instrumentation equipment installed. Additionally, major civil engineering work is required to accommodate for the technical infrastructure both underground and at the surface.

In order to achieve similar detector performance in the much harsher environment of the HL-LHC, several upgrades of the detectors are necessary. These are collectively referred to as Phase II upgrades. The environment at the HL-LHC necessitates comprehensive upgrades of all sub-systems of the ATLAS detector [99]. The trigger and data acquisition systems need to be modified for the higher data rates and increased data volume at the HL-LHC. This includes a split L0/L1 hardware

trigger. Information from upgraded readout electronics of the different sub-systems will be used in the new trigger system. The expected particle fluxes and deposited energies in the calorimeters will be higher than the LHC design values. The radiation damage acquired over the past years and the new trigger system require a replacement of the front-end and back-end electronics of the LAr calorimeters. Similarly, the readout electronics of the hadronic tile calorimeter will be replaced. The performance of the components of the muon system needs to be increased considerably. The MDT readout system will therefore be replaced to obtain high precision coordinates of the muons.

The upgrade also includes the replacement of the entire inner tracking detector as the current ATLAS ID would exceed its limitations in the high luminosity environment [100]. The ID was designed to reconstruct the trajectories and vertices for 23 proton-proton-interactions per bunch crossing. At the HL-LHC there will be up to 200 *pp*-interactions per bunch crossing [72] which also means a larger number of tracks and vertices which need to be reconstructed. With the current ID, nearby tracks would be difficult to resolve and the efficiency in pattern recognition would be reduced. The identification of primary vertices as well as the matching of these to reconsturcted objects becomes challenging as well. A higher granularity of the ID is therefore required to correctly reconstruct the large number of tracks. Furthermore, the maximum number of hits that can be dealt with by the read-out electronics will be surpassed and consequently parts of the detector could not be read out. Tracking information of the new tracker can be used as additional input to the L1 trigger described in Section 4.2.6 which currently does not include any information of the ID. Another challenge is the expected radiation damage. The current ID was designed to withstand the radiation damage equivalent to an integrated luminosity of 400 fb^{-1}. The predicted neutron fluence equivalent corresponding to an integrated luminosity of 4 000 fb^{-1} is shown in Figure 4.11 for a quarter segment of the detector.

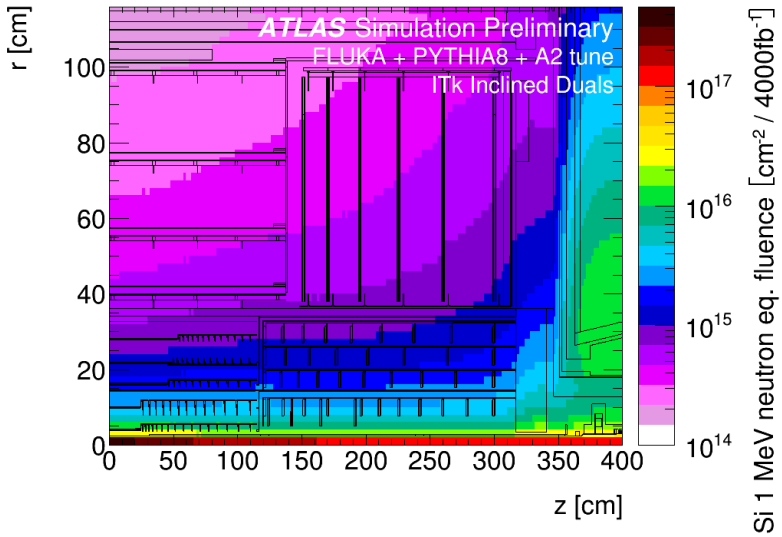

Figure 4.11: The 1 MeV neutron fluence equivalent per 4 000 fb^{-1} as a function of the horizontal distance from the interaction point in the beam direction z and the radial distance from the beam pipe r. The highest fluences occur in the inner-most part of the ID. Figure taken from Ref. [101].

CHAPTER 5

ATLAS Inner Tracker Endcap Service Trays

A general overview of the ATLAS Inner Tracker (ITk) and its mechanical framework is given in this chapter focusing on the endcap structure. The ITk endcap service trays which are components of the endcap structure are described in detail. The development of their design and the studies carried out by the author to fullfill the production requirements are discussed. Finally, the service trays to be installed in the endcaps are presented.

5.1 The Inner Tracker (ITk)

The ITk [100] is designed to withstand the harsh conditions of the HL-LHC. It is an all-silicon detector and covers a pseudo-rapidity range of up to $|\eta| = 4$. Extending the η range with respect to the range covered by the ID enhances the physics reach of the detector in the forward region. The ITk design is 6 m long and 2 m in diameter. It will hold approximately 18 000 silicon modules and 60 million readout channels. The ITk consists of a pixel detector at small radius close to the beam line and a strip detector at larger radius. Both detectors are split into two subsystems covering the barrel and endcap regions. A visualization of the ITk is shown in Figure 5.1. The regions covered by the pixel and strip detector for the barrel and endcap regions are shown in Figure 5.2 for a quarter segment of the detector. This design provides the required granularity to resolve tracks in the HL environment.

5.1.1 ITk Pixel Detector

In the barrel region, the pixel detector consists of five layers of silicon planes arranged in concentric cylinders around the interaction point. In the endcap regions, there are four ring layers consisting of 16 to 19 rings. Pixels as small as $50 \times 50\,\mu m^2$ are used to achieve the high granularity. The two innermost barrel layers and the innermost endcap ring layer can be replaced after some runtime if necessary. These are the components facing the largest radiation damage. The other components of the pixel detector are designed to operate for the full HL-LHC lifetime.

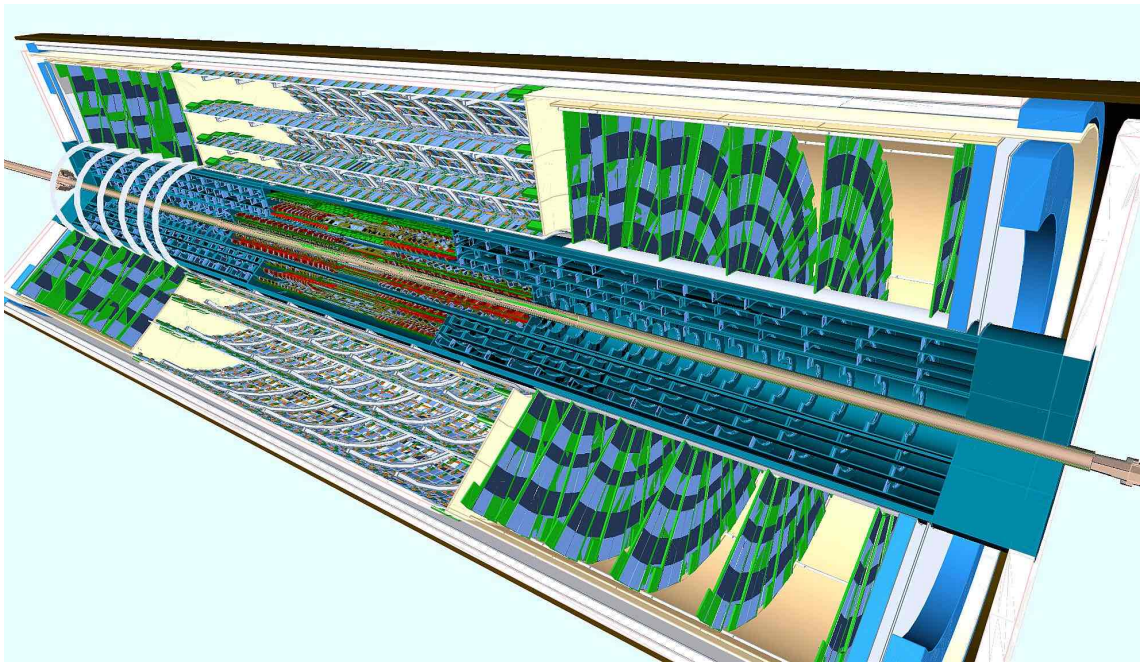

Figure 5.1: Schematic overview of the ITk detector. Figure taken from Ref. [100].

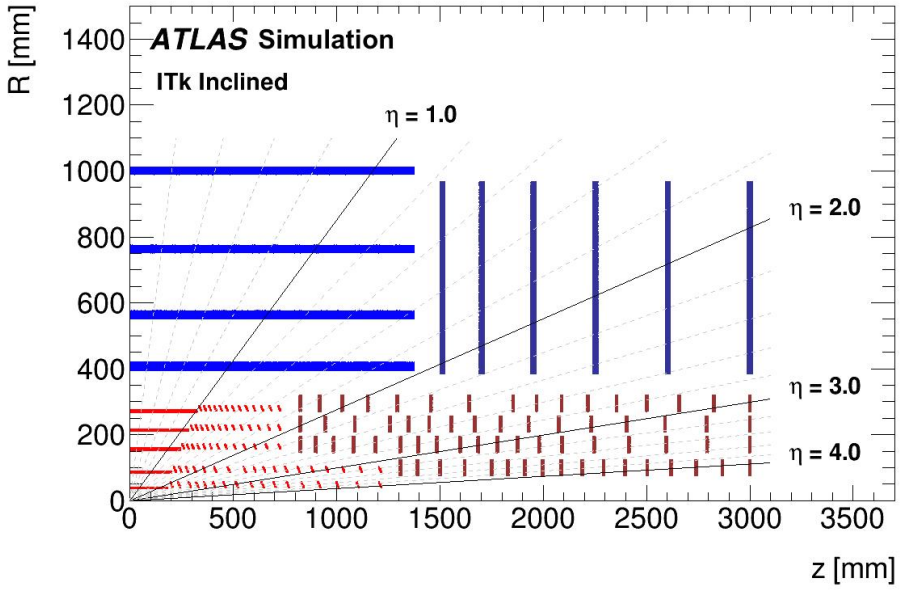

Figure 5.2: Layout of the ITk shown as a profile view with the horizontal distance from the interaction point in the beam direction z and the radial distance from the beam pipe r. The pixel detector components in the barrel region are shown in red and in the endcap region in dark red. The strip detector components of the barrel are shown in blue and of the endcap in dark blue. Figure taken from Ref. [100].

5.1.2 ITk Strip Detector

The strip detector is made of four barrel layers surrounding the interaction point and two endcaps in the forward regions. The basic building blocks are the rectangular staves for the barrels and the wedge-shaped petals for the endcaps as shown in Figure 5.3.

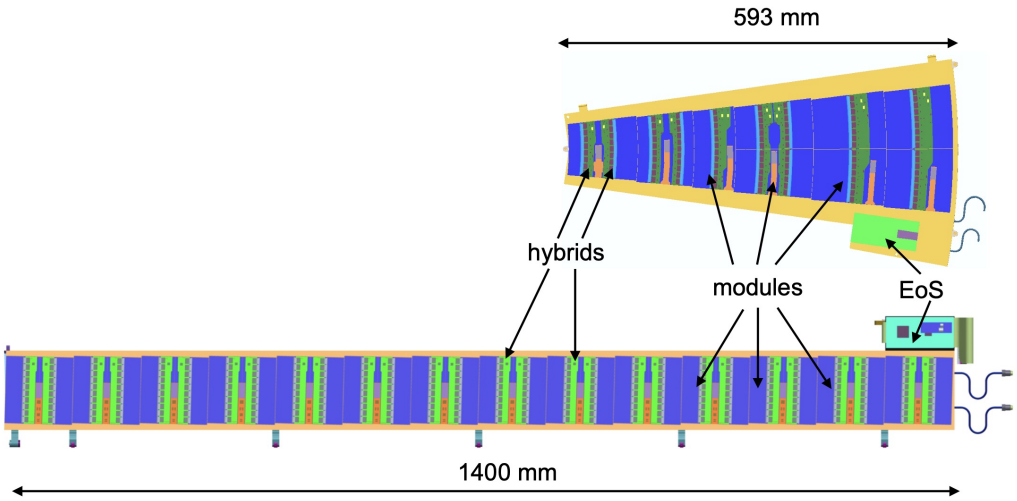

Figure 5.3: An endcap petal (upper) and a barrel stave (lower) with their components as presented in [100].

The barrel detector consists of 392 staves. Each of the two endcaps is made of six disks which each hold 32 petals, resulting in a total of 384 petals. Both the petals and staves are built from the same main components which are described in the following.

Local Supports The local support structures provide the mechanical support and hold the electrical, optical and cooling services. They also provide fixation points for correct alignment. The purpose of alignment is to determine the exact geometrical location of the detector elements to ensure precise reconstruction of the particle tracks. The petal and stave cores are two types of local supports with different geometrical properties but the same conceptual design.

The cores have a sandwich-structure with a carbon fiber-based layer on each side. In between is a low-density carbon fiber honeycomb structure and the titanium cooling pipes embedded in thermally conductive foam. These structures can be cooled down to −35 °C with CO_2 cooling.

Bustape and End-of-Substructure Card A polyimide tape called bustape is glued to both sides of the local supports. The bustape holds the electrical transmission lines which converge in the End-of-Substructure (EoS) card on each side of the core. The EoS provides the power and data transmission and is the interface to the electronics outside of the detector.

Modules Each stave holds 28 identical silicon modules, 14 on each side. Shorter strip modules of 24.1 mm length are used on the two inner barrel layers. Longer strips of 48.2 mm length are used on the two outer cylinders.

Each petal holds 18 modules, 9 on each side. There are six different sensor geometries used for the petal due to its wedge shape.

The modules hold one silicon strip sensor, one or two printed circuit boards and a powerboard to power the electronics. An example of a strip barrel module with the three main components is shown in Figure 5.4.

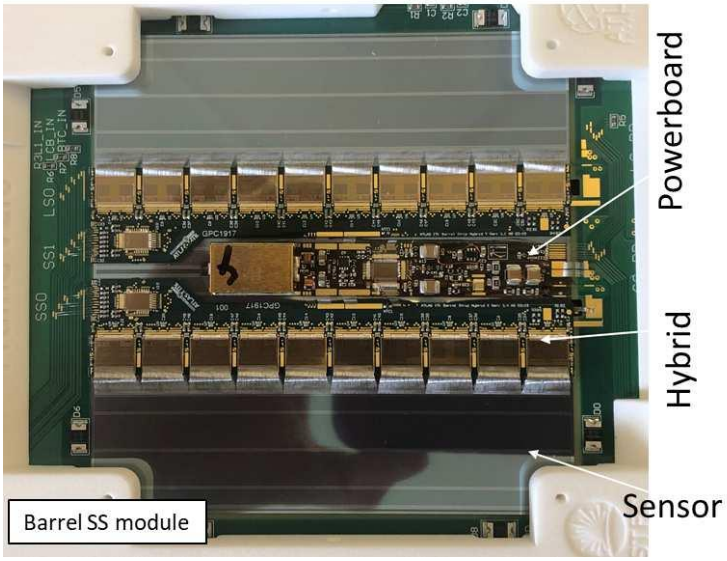

Figure 5.4: A barrel stave module consisting of a sensor, a printed circuit board (labeled hybrid) and a powerboard as presented in Ref. [102].

The petals and staves are loaded into global structures to form the strip barrel detector and the strip endcaps. A fully equipped endcap is shown in Figure 5.5. The structures of the barrel detector and the endcaps are supported by the ITk strip detector global structure.

5.2 ITk Strip Detector Global Structure

The Outer Cylinder (OC) is the outermost global structure supporting the ITk and is part of its Faraday cage. It houses the strip barrel and endcap structures. The OC is 7 m long and has a diameter of 2 m. The full strip detector global structure is shown in Figure 5.6. The barrel structures are supported by the OC through interlinks. The endcap structures are supported through a semi-kinematic rail system. The OC is closed at both ends by end plates called structural bulkheads. The pixel detector is located inside of the inner tube. The inner tube is connected to the bulkheads on each side. The structures are largely made of Carbon Fiber Reinforced Polymer (CFRP) to provide high mechanical stability and robustness despite large temperature variations.

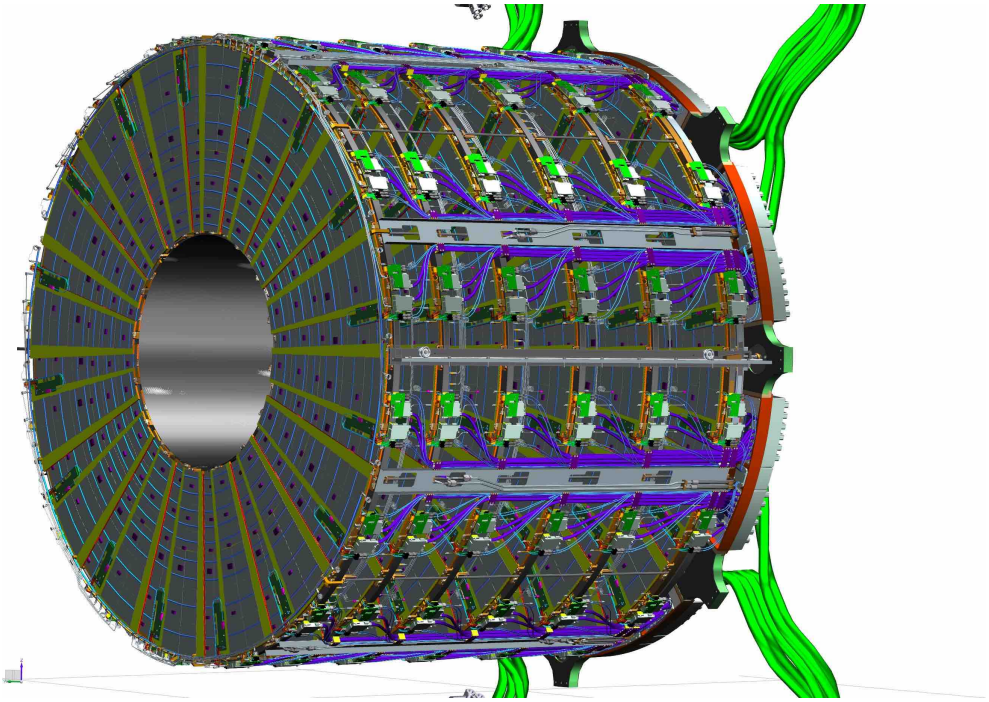

Figure 5.5: Fully equipped endcap including petals, electrical and cooling services.

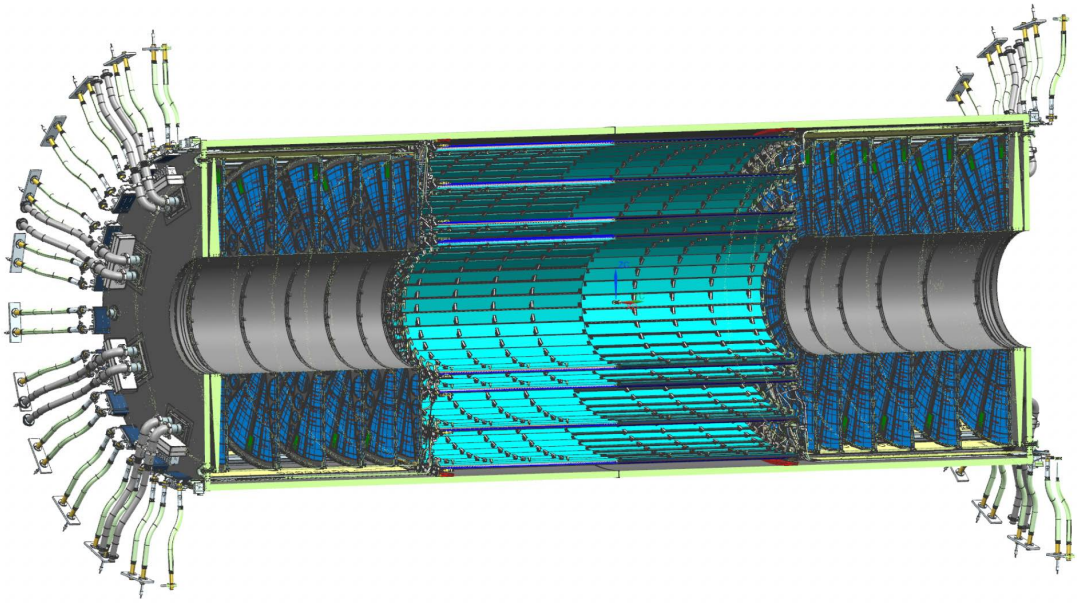

Figure 5.6: Global structure of the ITk strip detector consisting of the outer cylinder closed by the bulkheads, the barrel structure and the endcap structures. The pixel detector is inside the inner tube. Figure taken from Ref. [100].

5.2.1 Barrel Structure

The mechanical structure of the barrel holds the staves. It consists of four concentric cylinders connected with interlinks which are specifically designed clamping systems. The cylinders are made of a single layer of CFRP. Flanges at the ends of each cylinder allow to attach the interlinks and maintain its circular shape. Locking points to attach the staves are located on the outside of the cylinders.

5.2.2 Endcap Structure

The endcap structure provides the mechanical support for the petals, the electronics required to power and read out the petal modules and the cooling system. It consists of an inner tube, six wheels, two insertion rails, a stiffening disk at one end and eight service trays on the outside of the structure. The global structure of an endcap is shown in Figure 5.7.

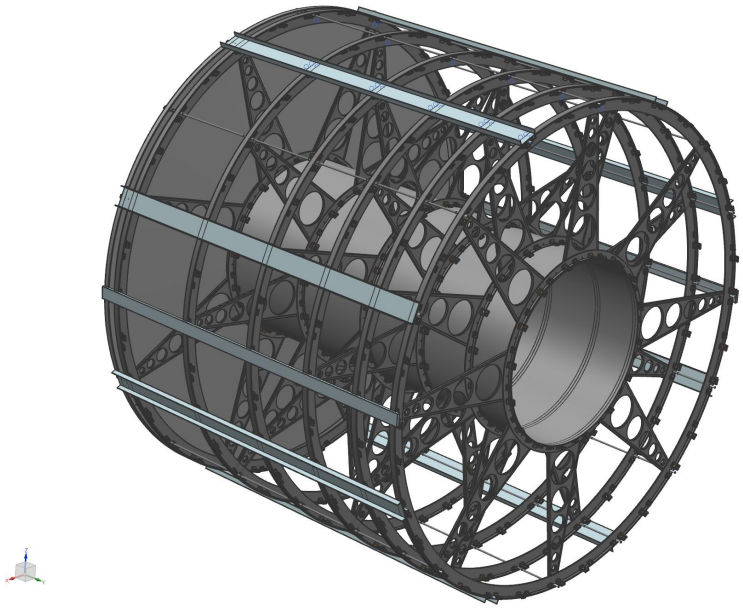

Figure 5.7: Mechanical structure of the endcap consisting of the inner tube, six wheels to hold the petals, two insertion rails the stiffening disk at one end and eight service trays on the outside of the structure. Figure taken from Ref. [100].

The wheels hold the petals which together form the disks of the endcap. Multiple locking-points on the wheels and locators on the petals allow for precise positioning of the petals.

Each wheel consists of an outer ring with a radius of 98.9 cm and an inner ring with a radius of 37.1 cm. The rings are produced by winding carbon fiber threads soaked in epoxy resin around an aluminum mold. They are connected by eight blades as shown in Figure 5.8.

Inside of the inner rings is the cylindrical inner tube. It defines the z-positions of the wheels and prevents rotations of the wheels around the z-axis. The current baseline design foresees three layers

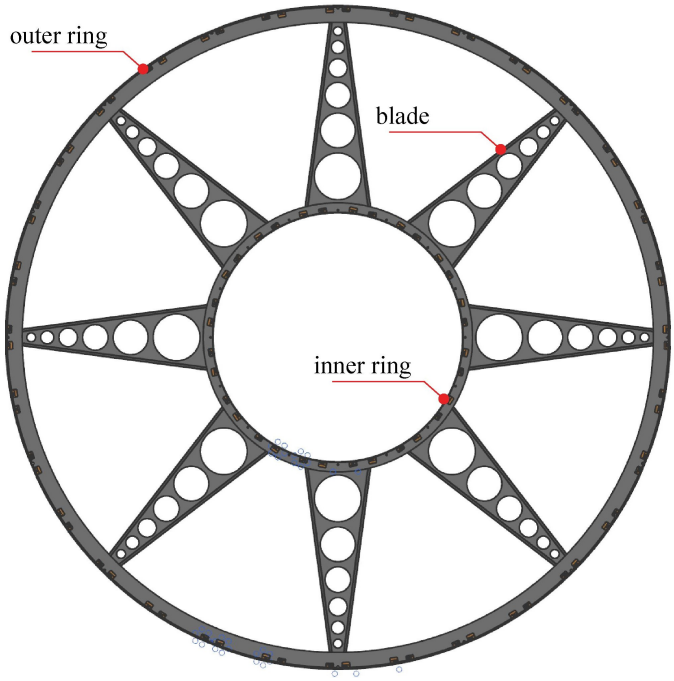

Figure 5.8: Endcap wheel consisting of an inner and an outer ring connected by blades. Figure taken from Ref. [100].

of carbon fiber windings to obtain the required mechanical stability with the minimal amount of material.

The stiffening disk is attached to the inner tube and located at the outside of the endcap, farthest away from the interaction point. It adds mechanical stiffness in z-direction and acts as thermal barrier. It is made of carbon fiber sheets.

The service trays are located on the outside of the cylinder of the mechanical structure and extend over the full length of the endcap structure as shown in Figure 5.7.

5.3 ITk Endcap Service Trays

The ITk endcap service trays hold the cooling pipes of the petals and guide their electronics. In addition, they add to the mechanical stability of the endcap structure. They also provide a low electrical resistance path between the cooling pipes and the wheels or stiffening disk. This allows for these parts to be connected to the Faraday cage formed by the OC and the bulkheads of the ITk global structure for grounding and shielding purposes. The service trays are built at DESY (Deutsches Elektronen Synchroton). Studies on the service tray requirements, material studies and the expected performance are documented in ATLAS internal reports.

There are eight service trays per endcap. The baseline design of the service trays is a C-shaped profile with cutouts at the disk positions as shown in Figure 5.9. The technical drawing of the

service tray can be found in Appendix A. Modifications of the baseline design in order to satisfy the component requirements are discussed in the respective sections below.

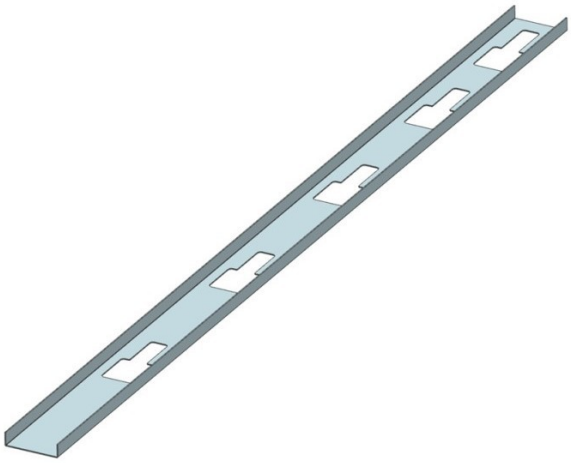

Figure 5.9: Baseline design of a service tray.

The cooling pipes extend through the cutouts to reach the petals they are servicing. There are five cutouts for six disks as the outermost disk can be directly accessed by the cooling pipes without entering the service tray first. Twelve pairs (inlet and outlet) of cooling pipes are needed to supply the six disks as each pair of cooling pipes supplies 16 petals which corresponds to half a disk. Each of the eight service trays therefore holds one or two pairs of cooling pipes.

The design of the service trays is guided by the required specifications which are summarized in Table 5.1.

Table 5.1: Specifications of the ITk endcap service trays.

Objective	**Specification**
Envelope model boundaries	1 396.5 mm × 20 mm × 80 mm
Grounding and shielding	electrical resistance < 20 Ω between wheel, service tray and cooling pipes
Bending stiffness	$> 1.5 \times 10^3$ N/m
Thermal and humidity stability	deformation < 100 µm for a 45 °C ΔT (20 °C to −25 °C) and a dew point of −60 °C
Radiation hardness	7×10^5 Gy

Some of these requirements are fullfilled by the choice of material. Studies confirming that the materials satisfy the safety requirements described below are reported in ATLAS internal documents.

Carbon fibers pre-impregnated with resin (prepregs) are used to build the service trays. A prepreg with woven fibers is chosen to ensure the same mechanical stability and thermal expansion in the vertical and horizontal directions. The targeted lamination thickness of the cured service tray is 1.6 mm in order to achieve the required mechanical stiffness. This is accomplished by using eight layers of a EX-1515 cyanate ester resin system [103] with T300 fibers [104]. The second and seventh layers are rotated by 45° to obtain a similar mechanical and thermal stability in all directions of the final component. The selected materials satisfy the specifications for thermal and humidity stability. Prepregs similar to the described one have a Coefficient of Thermal Expansion (CTE) of around 1.8 µm/K [105]. For a temperature difference of 45 °C and a CTE of 1.8 µm/K, the expected expansion would be 81 µm which satisfies the specification. The EX-1515 prepreg is shown to be radiation hard up 1×10^7 Gy and fire resistant. It complies with the CERN safety rules for fire safety and radiation resistance. For the test samples made of this prepreg six layers were used to achieve the targeted lamination thickness.

The fullfillment of two of the specifications require further studies. The first is the optimization of the design in order to achieve high mechanical stability. The second is the achievement of the low resistance path between the cooling pipes and the wheels.

5.3.1 Manufacturing Procedure

The studies discussed in the following sections require dedicated CFRP test samples which are produced similarly to the service trays. The different manufacturing steps are described here for one of the service trays using a designated mold and the previously described prepreg. The design of the mold is discussed in Section 5.3.2. The service trays are built without cutouts and are then machined. Machining the trays after curing allows for a simpler mold and easier unmolding compared to a procedure where the prepreg is cut before curing. The eight prepreg layers needed for a service tray are therefore rectangular sheets. The width of the prepreg sheets increases slightly the further out the layer is. The mold is covered with multiple layers of a liquid release agent and a release wax which allows for easy removal of the service tray after curing. Each of the eight layers is individually aligned on the mold using marking points and placed on the previous layer. The innermost layer has three copper pads co-cured to it which will be on the inside of the tray. The copper pads are required for the low electrical resistance path between a cooling pipe and a wheel which is discussed in Section 5.3.3. They are covered with tape to protect them from being coated with resin during curing. The first prepreg layer is placed directly on the mold as shown in Figure 5.10.

After the third layer of prepreg, the air is evacuated once as described below for the full set of layers. This intermediate pumping further compresses the first layers which leads to a higher density of the final product. After the last layer is placed, further copper strips are placed on the outside of the tray and are protected with tape. The stack is then covered with a layer of porous release film. It allows excess resin to be drained through it and can be easily removed from the component after curing. On top of the release film, a layer of peel ply is placed for a smooth surface. It also bleeds the sample and absorbs some of the resin during the co-curing process. This leads to a higher mechanical stiffness of the component. The setup is then covered with a breather cloth. This layer is added to create an optimal vacuum since it facilitates evacuating the air at the edges and corners

of the sample. The layers added on the prepreg for the co-curing process are shown in Figure 5.11.

Figure 5.10: First layer of the prepreg directly placed onto the mold.

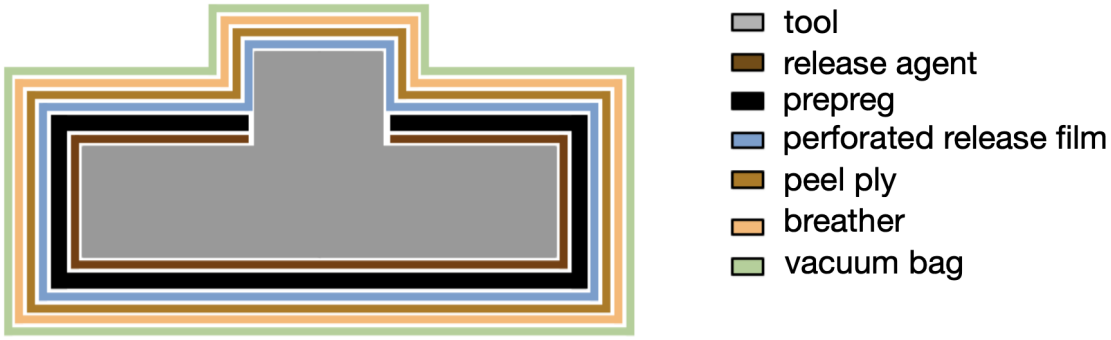

Figure 5.11: Layers on the prepreg while co-curing. The prepreg layers placed on the mold are covered with the release film which is subsequently covered with the peel ply and the breather.

Finally, the sample is bagged with a sealed vacuum bag. The air is then evacuated with a vacuum pump as shown in Figure 5.12. The service trays are co-cured in an autoclave which controls the temperature and pressure at which the curing takes place while maintaining a vacuum. The autoclave can also be seen in Figure 5.12. For the curing process, the temperature is increased in two steps. The curing temperature of 125 °C is then held for 60 min. Finally, it is cooled down until room temperature is reached. A pressure of 2 bar is applied during the cycle. The curing cycle of a service tray is shown in Figure 5.13. After co-curing, the breather, the peel ply and the release film are removed. The service tray is separated from the mold and the tape on the copper strips is removed.

Figure 5.12: Evacuating the air out of the sealed vacuum bag.

Figure 5.13: Autoclave curing cycle used for co-curing the service trays.

5.3.2 Modified Service Tray Design

The overall mechanical stiffness of the C-shaped service tray is studied in simulations. Under specific conditions it is possible that the material next to the cutouts buckles as this is the weakest part. This behavior can be seen in simulations where the tray is clamped on one end and a force is applied perpendicular to the tray at the other end. The service tray design therefore needs to be modified to provide the desired mechanical stability. The results of the simulations shown in Figure 5.14 compare the behavior under the described force of a C-shaped service tray and a service tray with a cover.

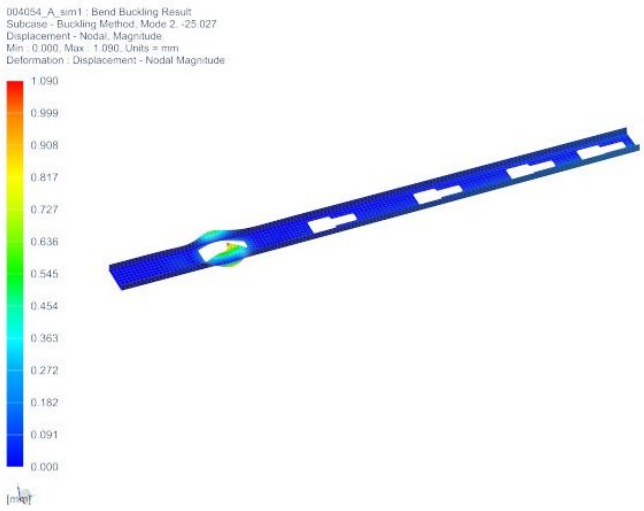

(a) Without cover, the sides of the cutouts can buckle as they are the weakest parts.

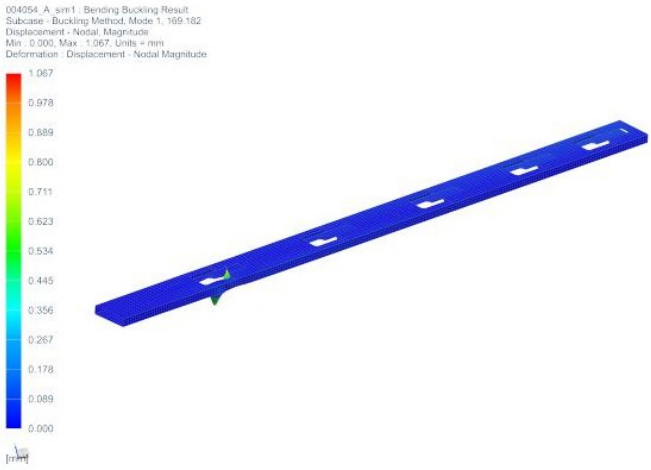

(b) With a cover, no buckling is observed.

Figure 5.14: Simulations showing buckling of the service tray without and with cover. The magnitude of displacement is normalized in the simulations.

Without a cover, a smaller force is required until the parts next to the cutouts buckle as shown in Figure 5.14(a). When a cover is added, this force increases considerably as shown in Figure 5.14(b). Furthermore, the parts next to the cutouts do not stand out as substantially weaker compared to other parts of the service tray any longer.

A cover plate of 1.4 m length and 8 cm width is built to further study its effect on the overall mechanical stability of the service tray. The cover plate itself does not have a very high mechanical stiffness and shows a large gravitational sag as shown in Figure 5.15. Additionally, the cover would add another step in the assembling procedure and would need to be removable in case of maintenance work on a cooling pipe.

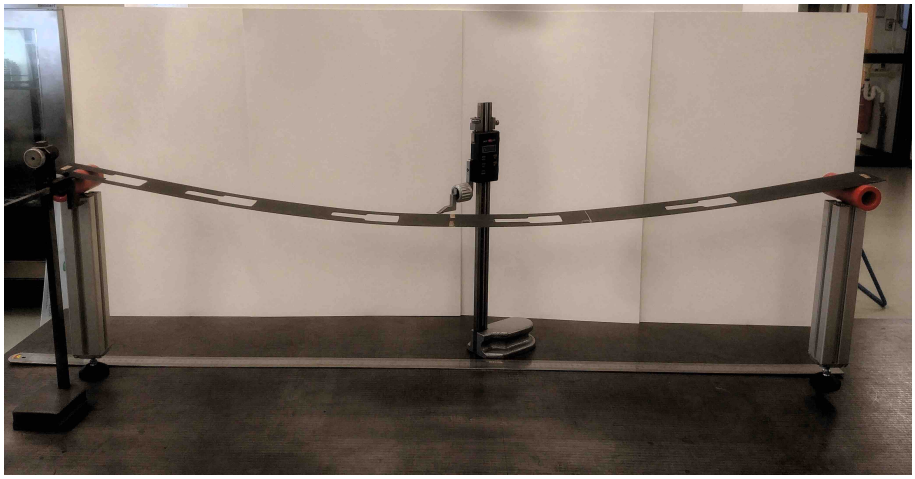

Figure 5.15: Real-size cover with low mechanical stiffness resulting in a considerable gravitational sag.

Instead of introducing a cover, the design of the service tray itself is therefore modified. Flanges are introduced at the edges which strongly increase the mechanical stability of the structure.

Besides the additional flanges, the shape of the cutouts also need to be modified to avoid collisions of the service tray and the cooling pipes passing through the cutouts. It is shown in Figure 5.16 including a profile view. The circular copper pads which are co-cured to the inside of the service tray are shown in the figure as well.

Building a service tray with the updated design requires a specific mold. The flanges hinder an easy removal of a mold consisting of one piece after curing. The first design of the mold therefore consists of two parts that are cut diagonally and fastened with screws. After curing, the screws are removed and the two diagonally cut parts can then be pushed out of the tray in opposite directions. A short prototype of approximately 30 cm length of such a mold is built to test the functionality of this setup. It is shown in Figure 5.17.

Several short service tray prototypes were successfully produced with this mold. For easier removal of the approximately 1.4 m long service trays, the real-size mold for the production is split in three parts instead of two as shown in Figure 5.18. The three parts are cut in such a way that the center part obtains a wedge shape. They are again secured with screws. After curing, the screws are removed and the center part of the mold is taken out first. This leaves enough space to push out the

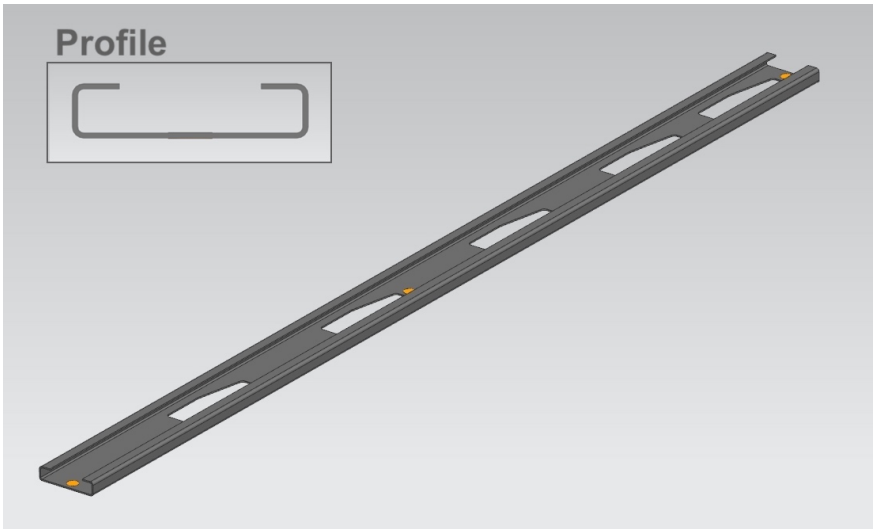

Figure 5.16: Updated design of the service tray including flanges and a profile view of the service tray.

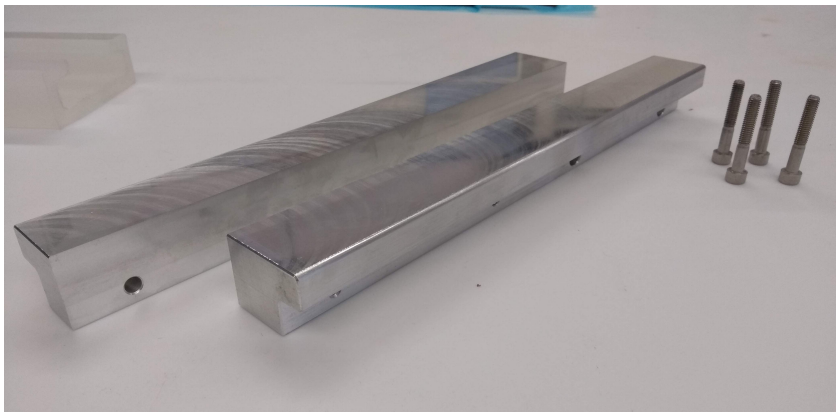

Figure 5.17: Aluminum mold of 30 cm length consisting of two components connected with screws.

other two parts of the mold through the empty center.

The first tray produced with the previously described mold was used to confirm that the bending stiffness specification of the component is satisfied. It is defined as the ratio of the applied force in the center of the component over the resulting sag. The ends of the component are supported but not clamped. The specification requires a bending stiffness of more than 1.5×10^3 N/m. The service tray was therefore supported at both ends and a weight placed on its center as shown in Figure 5.19. For the weight of 11.7 kg used in this test, the maximum sag of the service tray which still satisfies the specification is

$$d_{\text{max}} = \frac{F}{S_{\text{min}}} = \frac{11.7\,\text{kg} \times 9.81\,\text{N kg}^{-1}}{1.5 \times 10^3\,\text{N m}^{-1}} = 77\,\text{mm}. \tag{5.1}$$

The measured sag is 17 mm and thus lies within the specification.

(a) Mold split in its components.

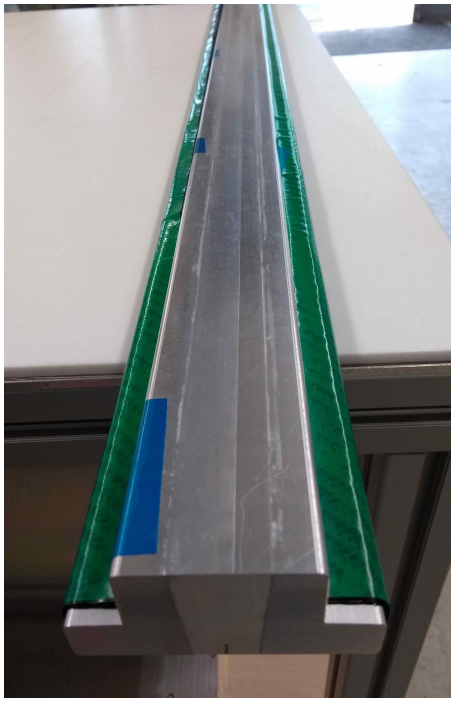

(b) Mold with one layer of prepreg around it.

Figure 5.18: The aluminum mold for the production of the service trays.

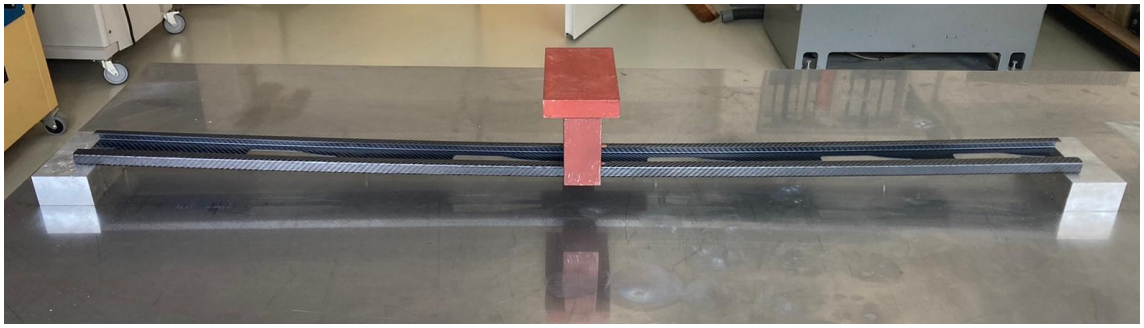

Figure 5.19: Setup to test bending stiffness of the service tray.

5.3.3 Low Electrical Resistance Path

The connection between the wheel and the cooling pipes is required to have an electrical resistance $< 20\,\Omega$ in order to connect the components to the global Faraday cage. The different parts of the global structure are electrically connected. The service trays provide the electrical connection between the wheels as well as the connection of the global structure to the cooling pipes. The cooling pipes provide the direct connection of the global structure to the Faraday cage. Two different kinds of connections have to be electrically conductive to fulfill this specification. The first connection

is between a wheel and a service tray. The second connection is between the service tray and the cooling pipes.

For both cases, it is necessary to be able to connect electrically to the service trays. The fibers in a CFRP component are highly conductive but are covered in insulating resin. Exposing the fibers is therefore necessary to establish electrical connections to such components. A direct contact to the fibers can also be established by co-curing copper strips to their surface. The copper pads used for the service trays are made of 1 oz copper which has a thickness of 35 µm.

The copper piece is placed on the prepreg before co-curing during which the copper is pressed against the fibers. The copper is covered with tape to protect it from resin leaking out during the curing process. The tape is removed after co-curing, exposing the copper which is now connected to the fibers.

Electrical conductivity measurements with the setup shown in Figure 5.20 confirmed this procedure to yield low resistance connections of two points on a CFRP plate. All resistance measurements shown in this section have an uncertainty of $\mathcal{O}(0.1\,\Omega)$ corresponding to the uncertainty of the multimeter used for the measurement. They are carried out through a four point measurement to eliminate the cable and contact resistance.

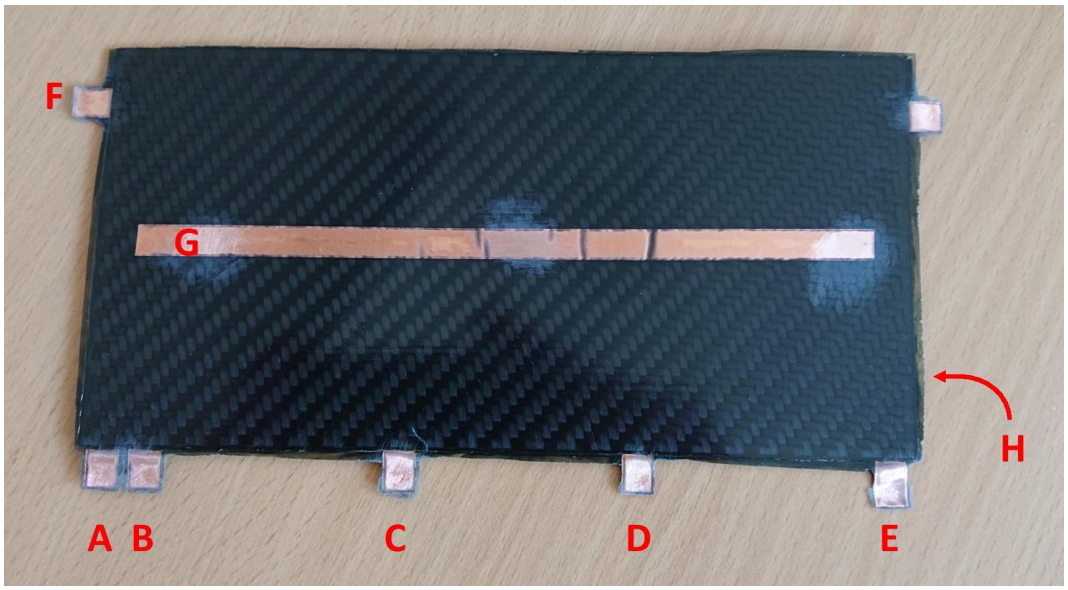

Figure 5.20: CFRP plate with co-cured copper strips to demonstrate low resistance between two such strips.

The plate is using six layers of woven prepreg. The copper strips A-F are positioned between layers 3 and 4, while the strips G and H are located on the outsides of the sample. The electrical resistance is measured between all combinations of pairs of co-cured copper strips shown in the figure. The measured resistances were below 0.2 Ω for all measurements between the different copper strips as demonstrated in Table 5.2.

In addition, two samples with a length of 60 cm and a width of 2.5 cm are produced to study the electrical resistance of a longer path in a CFRP component. A copper strip is co-cured at both ends

Table 5.2: Electrical resistance measurements through a CFRP plate using copper strips.

	Electrical resistance [Ω] of path					
Measurement	**A→B**	**A→C**	**A→D**	**A→E**	**A→F**	**G→H**
Cu strips in CFRP plate	0.05	0.13	0.14	0.16	0.08	0.04

of each sample. The electrical resistance of these samples is about 1.4 Ω for both samples. For comparison, the electrical resistance over the full length of 1.4 m of the cover plate described in Section 5.3.2 is measured between copper strips co-cured to each end of the plate. The measured resistance is 1.5 Ω. It can be concluded that the low electrical resistance is maintained over the full length of the service trays.

Electrically Conductive Glued Connection of a Wheel to a Service Tray

The wheel and the service tray are glued together. This connection needs to be electrically conductive to satisfy the corresponding specification. The wheels are built by winding carbon fibers wetted with resin around a mold and are cured at room temperature. The wheels and the stiffening disk are milled at the positions where the service trays are glued onto them in order to obtain a flat surface and expose the fibers. The service trays have copper pads co-cured to their surface at the positions where they are glued to the wheels and the stiffening disk as shown in Figure 5.21.

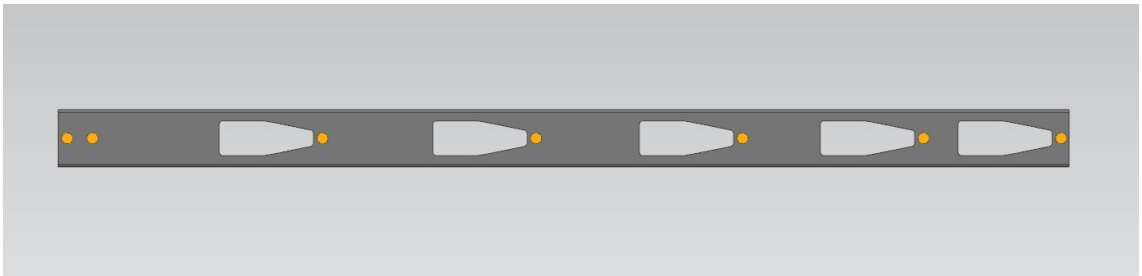

Figure 5.21: Copper strips at wheel positions and stiffening disk position on the outside of the service tray.

Consequently, both surfaces are electrically conductive. The glued connection between each of the eight service trays and the six wheels and the stiffening disk needs to be electrically conducting. It is therefore necessary to find a baseline method for the glued connection that yields low and reproducible electrical resistance results which allows for a fast assembly.

For the glued connection between service tray and the wheel Hysol adhesive [106] is used which is shown to be radiation safe [107]. Two options for obtaining an electrically conductive glue layer are compared in the following. Hysol loaded with graphite yields an electrically conductive adhesive and is used for other parts of the ATLAS detector. The chosen percentage of 25 % graphite powder ensures the electrical conductivity of the mixture. For the second option a 100 µm Carbon Fiber (CF) mat is placed on top of a layer of Hysol. Unidirectional CF mats [108] are used with an area

density of 20 g/m^2 and a thickness of 100 µm. When the two components are glued together with this setup, the mat touches both surfaces and connects them electrically.

Alternative options including higher percentages of graphite and Hysol loaded with milled carbon fibers were also studied but ruled out. The carbon fibers do not mix well with the adhesive and it cannot be assured that they are distributed evenly throughout the glue. At high percentages of fibers and graphite, the mixture becomes very viscous and cannot be applied in even layers.

The electrical resistance of the two options for the glued connection is studied with a setup of two plastic plates covered with copper foil. A glue layer of 150 µm thickness is applied over an area of 3 cm × 3 cm using a stencil which is then removed. For the samples with graphite loaded Hysol, 90 µm thick spacers are then applied. They ensure that a sufficiently thick glue layer is maintained which is necessary for its conductivity and adhesive strength. Using a spacer thinner than the stencil ensures that the full surfaces of both components make contact with the adhesive. For the samples with the CF mat, no spacers are necessary as in this case the mat itself acts as a spacer of 100 µm. The second plate is then pressed onto the glue layer and a weight of 1 kg is placed on the pair of plates while curing at room temperature for 24 h. The setup without the weight is shown in Figure 5.22.

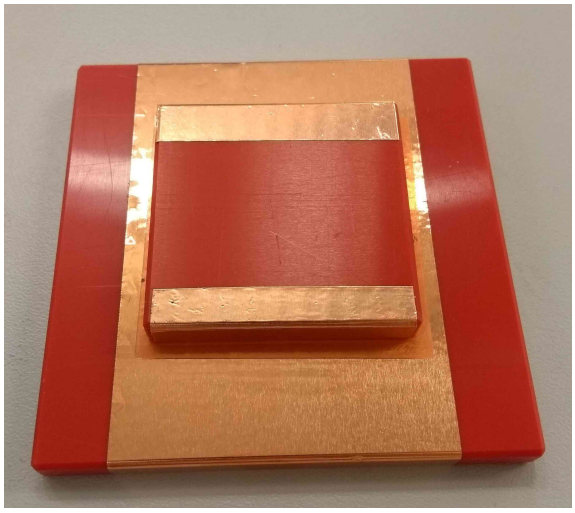

Figure 5.22: Test setup to study the conductivity of a glued connection with graphite loaded Hysol and Hysol with a CF mat. The glue layer is applied between two plastic plates covered with copper foil.

The electrical resistance is measured between the copper foil on the lower plate and the copper foil on the upper plate. Two samples were produced with Hysol loaded with 25 % graphite. Five samples were produced with the less conventional approach using Hysol and a CF mat. The electrical resistance measurements of these samples are shown in Table 5.3. Both options, the 25 % graphite loaded Hysol with a 90 µm spacer and Hysol with a CF mat provide a low electrical resistance of 3 Ω or less. The specification on the electrical resistance of the connection would therefore be satisfied with both options.

Table 5.3: Electrical resistance of glue test samples with 25 % graphite powder using a 90 µm spacer or a 100 µm thick CF mat.

	Electrical resistance [Ω] of sample				
Electrically conductive glue option	**I**	**II**	**III**	**IV**	**V**
Graphite powder 25 %, 90 µm spacer	3.0	2.0	-	-	-
100 µm CF mat	0.9	1.5	1.0	0.7	1.2

For a more realistic test of the glued connection dedicated CFRP samples are built. Each sample pair consists of a part representing the wheel and a part representing the service tray. The overlapping area to glue the two parts together is approximately the size of the overlap of the tray and the wheel. The wheels are 2.4 cm wide and the stiffening disk is 2.8 cm wide. The service trays are 8 cm wide. The samples used for these tests are shown in Figure 5.23.

(a) Samples shown with glued surface facing upwards. The CF mat is shown in the middle.

(b) Samples shown with the outside facing upwards.

Figure 5.23: Real-size glue test samples representing the wheel (top) and the service tray (bottom).

The size of the glue layer tested with these samples is 3 cm × 8 cm. The samples representing the wheel are milled 300 µm deep on an area of 3 cm × 8 cm. The samples representing the tray have a copper strip co-cured to one side of the full size of the overlapping area. Smaller copper strips are co-cured on the back of both samples to measure the electrical resistance after the two parts are glued together. The two parts are glued together with 25 % graphite loaded Hysol or with Hysol and a CF mat the size of the entire glue area. The glue layers are applied as described before. For

the samples with graphite loaded Hysol, spacers with a diameter of 130 µm are used that can be placed in the glue layer.

Two samples with graphite loaded Hysol and three samples with Hysol and a CF mat are built. The electrical resistance is measured between the copper strips on the outsides of each sample pair. The results of the resistance measurements are shown in Table 5.4.

Table 5.4: Electrical resistance measurements of the real-size glue area samples.

	Electrical resistance [Ω] of sample		
Electrically conductive glue option	**I**	**II**	**III**
25 % graphite loaded Hysol	29	23	-
Hysol and CF mat	0.7	0.9	0.8

The electrical resistances for the samples with the CF mat are all below 1 Ω and satisfy the specification. The samples with the graphite loaded Hysol have electrical resistances larger than 20 Ω exceeding the specification. A possible explanation for the considerably higher electrical resistance compared to the previous test is that the spacers may have been too thick for the applied glue layer preventing ideal contact of the surfaces. Nevertheless, the need for a spacer for the samples with graphite loaded Hysol introduces an additional production step.

Although the two tests described before show that low resistances can be achieved with both options for the glued connection, the Hysol and CF mat yielded low resistance results more consistently. Less preparation steps are involved as no spacer is required, resulting in a faster assembly of the endcap structure using this method. The chosen baseline method for the glued connection of the service tray and the wheel is therefore using Hysol and a CF mat.

Larger Gap Between Wheel and Service Tray

When manufacturing the wheels, small deviations from the expected shape can arise due to uneven winding of the fibers around the mold and the gravitational sag while curing. Instead of connecting directly, gaps between a wheel and a tray arise which can be up to 1 mm wide. Additionally, the surfaces of the wheels are not machined flat in this case to avoid increasing the gap even further. As a result, the surfaces where the trays are glued onto the wheels are not necessarily flat as can be seen in Figure 5.24.

Instead, the curvature of the wheel leads to the gap being larger at the edges of the area where the wheel and tray are glued together and smaller in the middle of it. These gaps of varying size need to be bridged with the glued connection of the tray and the wheel while maintaining the low resistance path. The baseline approach for this connection is a combination of Hysol adhesive with one layer of a CF mat. Therefore, it is studied whether using multiple such mats and a larger amount of the adhesive would sufficiently bridge the gap and maintain the low resistance of the connection. Using the same test setup as shown in Figure 5.22, three samples with five layers of CF mat and Hysol adhesive are produced. The electrical resistances of these samples are shown in Table 5.5.

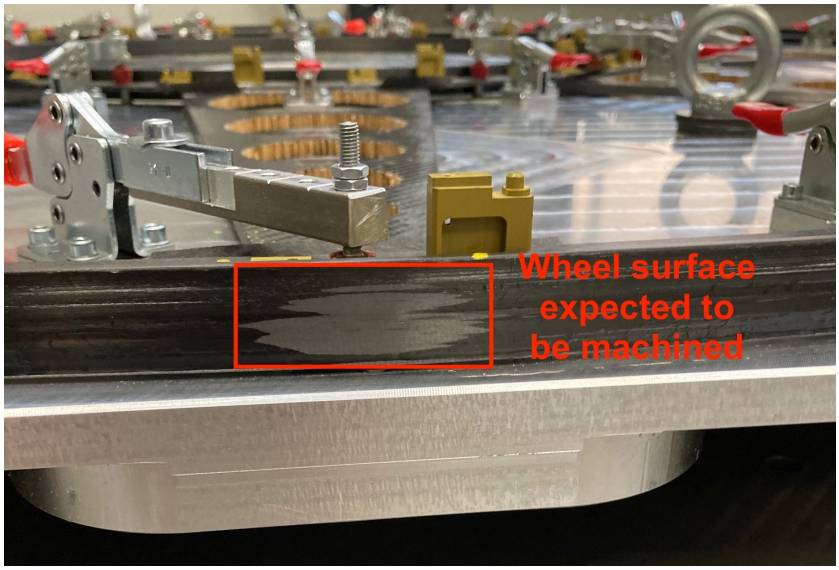

Figure 5.24: Surface of the wheel where the tray is supposed to be connected. The machined surface is smaller than the overlapping area of tray and wheel because of the slight deformation of the wheel.

Table 5.5: Electrical resistance measurements of glue samples with 5 layers of the CF mat.

	Electrical resistance [Ω] of sample		
Electrically conductive glue option	**I**	**II**	**III**
Hysol and 5 layers of CF mat	0.8	0.8	0.9

The measured electrical resistances are of the same order as with one layer of the CF mat. Multiple layers of the CF mat can therefore be used to achieve a low resistance connection of the wheel and the tray.

A second test is carried out to study the connection when the surface of the wheel is not as flat as expected. For this test, parts of a prototype inner wheel were used because these were readily available. The curvature of these samples is therefore the opposite of that of the outer wheel. In the endcap, the service trays are glued to the outside of the outer wheel. In this test setup, a plate representing the tray is glued to the inside of the inner wheel. The resulting gap is larger in the center and smaller on the outsides. It is filled with a stack of five CF mats. The three pieces of the mat in the middle of the stack are narrower than the outer two layers to fill this gap. The test setup is shown in Figure 5.25.

Two such samples are produced. The electrical resistance is measured between the copper foil on the plate and the sanded surface of the wheel part. This technique is however not ideal to connect to the fibers as the resin is not sufficiently removed. The electrical resistance between two points on the wheel surface therefore cannot be measured precisely and is relatively large at about 20 Ω. Consequently, no precise measurement of the glued connection could be carried out in this case. However, the electrical resistance between the two parts was similar to the electrical resistance

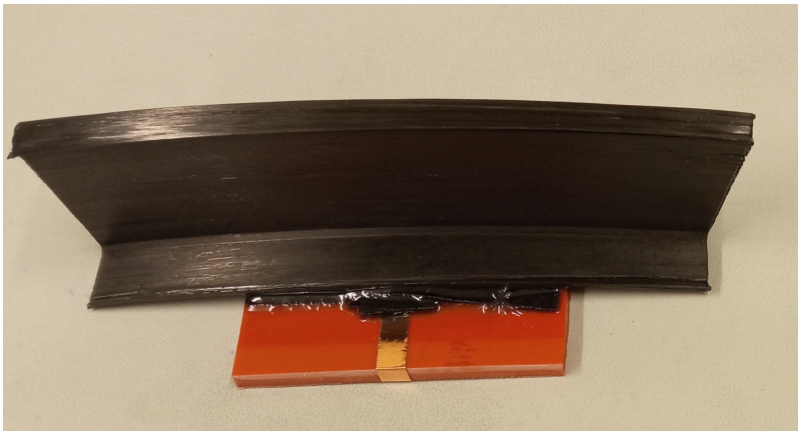

Figure 5.25: Test setup to bridge a larger and uneven gap between a wheel and a tray.

between two points on the surface of the wheel part. The electrical resistance of the glued connection in this test is therefore low.

In the endcap, the tray is on the outside of the wheel and the resulting gap could be bridged by a stack of CF mats adjusted to its shape. For a gap that is larger on the outside edges and smaller in the center, more layers can be placed on the outside and fewer layers in the middle.

Electrical Connection of a Service Tray and a Cooling Pipe

The second connection that needs to have a low electrical resistance is the connection between a service tray and a cooling pipe. The CFRP sample pairs described before are used to investigate how this can be achieved. A cable is soldered to the copper strip on the back of the sample representing the tray. This cable is then clamped to a stainless steel pipe representing the cooling pipe. The setup is shown in Figure 5.26.

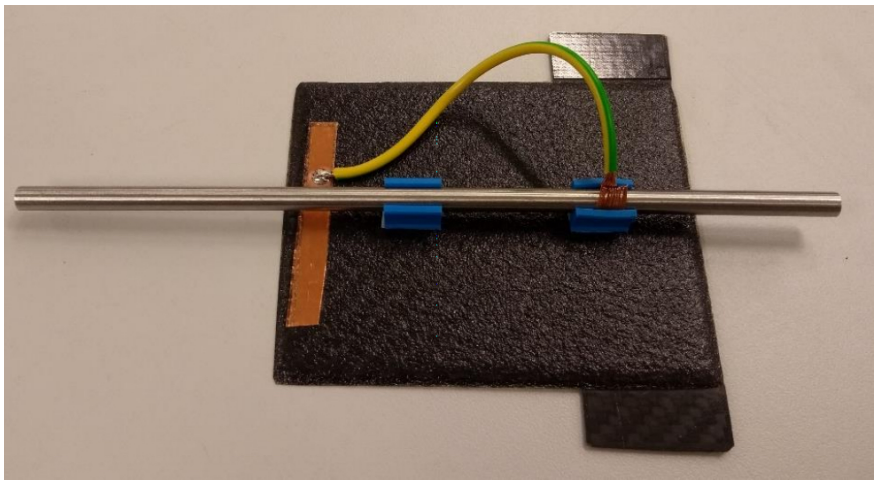

Figure 5.26: Test setup to electrically connect wheel, tray and pipe.

The connection to the pipe did not add any measurable resistance to the connection. The baseline for this connection is therefore a thin cable or copper strip which is soldered to a copper pad co-cured to the inside of the service tray and then clamped to the cooling pipe. Three copper pads are co-cured to the inside of each tray to provide multiple options where the cooling pipes can be connected.

One copper pad is located at each end of the tray and one copper pad is located in the middle. The positions of the copper pads co-cured to the service tray are shown in Figure 5.27.

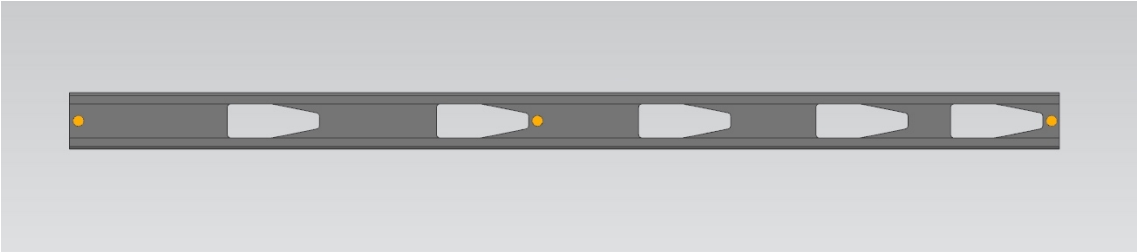

Figure 5.27: Positions of the Cu pads co-cured to the inside of the service tray to connect it to the cooling pipes.

5.3.4 Mechanical Stability of the Glued Connection

Despite giving satisfying results regarding the electrical conductivity using the CF mat, the mechanical strength of the connection as described is not optimal. The co-cured copper strip in the tests with the real-size connection covered the entire glue area. Its smooth surface reduces the strength of the glued connection. Detailed lap joint studies are carried out to find a solution that yields low electrical resistance and high mechanical strength.

First tests compare the mechanical strength of different types of conductive connections with a glue area of 2.5 cm × 2.5 cm. The samples used for these lap joint tests are 11 cm long and 2.5 cm wide. They consist of 6 layers of prepreg with additional tabs of 5.5 cm length which also consist of 6 layers of prepreg. These tabs ensure that the force is applied symmetrically by the tensile testing machine. A sketch of a sample for the lap joint test is shown in Figure 5.28.

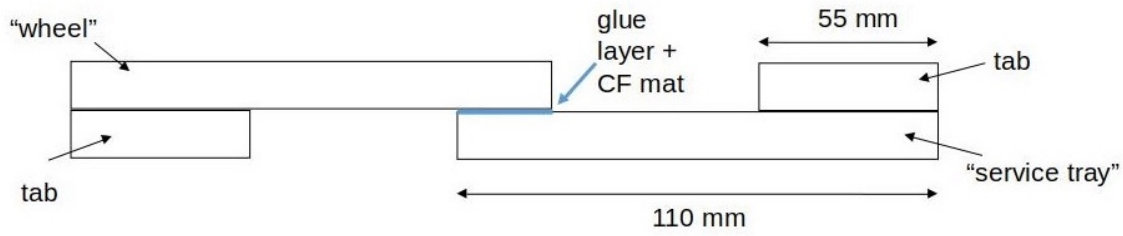

Figure 5.28: Sketch of the samples used in the lap joint tests.

One part of the sample again represents the wheel. The surface of these samples is milled for an area of the same size as the glue area. The other part represents the service tray and has a

copper strip co-cured to its surface. Different sizes and shapes of the copper strip co-cured to the service tray are studied to optimize the mechanical strength of the connection while maintaining its electrical conductivity. Following the results from the glue tests described in Section 5.3.3, the lap joint tests are carried out only with Hysol and CF mat to realize a low electrical resistance of the glued connection. In addition, a small piece of copper foil is co-cured below the glue area of both samples to measure the electrical resistance of the connection once the two samples are glued together. The applied glue layer has a thickness of 150 µm. The samples are cured at 70 °C for 1 h. An example of a lap joint sample after the two parts are glued together is shown in Figure 5.29.

Figure 5.29: Lap joint sample after gluing.

After the samples are glued together, their mechanical strength is measured in a tensile test. The tensile testing machine and a sample clamped into it is shown in Figure 5.30. The uncertainty on the force until failure measured with the tensile testing machine is of $\mathcal{O}(0.01\,\mathrm{kN})$.

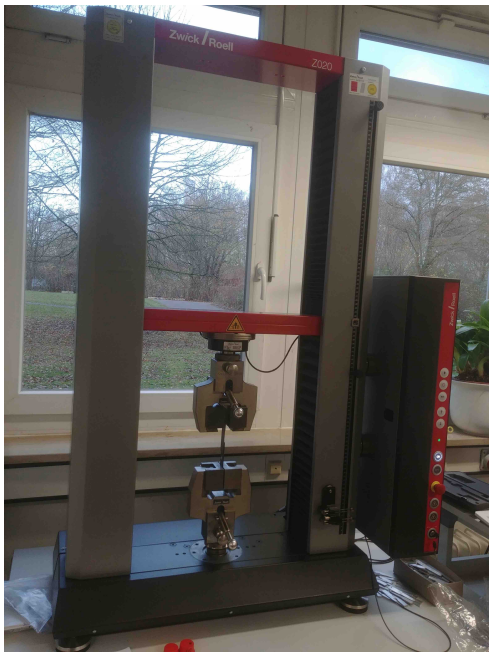

(a) Tensile testing machine used for the lap joint tests.

(b) Sample clamped in the tensile testing machine.

Figure 5.30: Setup for lap joint tests with tensile testing machine.

Lap Joint Tests Comparing Different Sizes of Copper Pads

The first lap joint tests investigate the effect of the size of the copper pad on the mechanical strength of the connection. Three different sizes of rectangular copper strip are tested on the part of each sample pair that represents the service tray. For comparison, additional sample pairs are created where both parts are milled. The different types of sample pairs are shown in Figure 5.31. The results of the tensile tests and the electrical resistance for each of these samples are shown in Table 5.6.

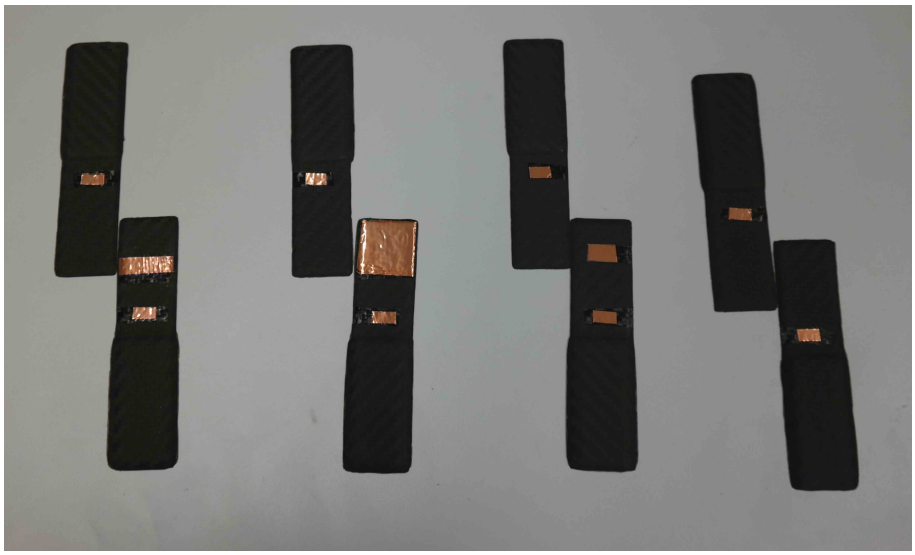

Figure 5.31: Lap joint samples with different sizes of rectangular copper strips co-cured to the sample representing the service tray before gluing.

Table 5.6: Results of the electrical resistance measurements and the tensile tests comparing different sizes of co-cured copper foil.

Electrically conductive surface option	**Electrical Resistance** [Ω]	**Applied Force Until Failure** [kN]
Cu foil 25 mm × 25 mm I	1.0	0.53
Cu foil 25 mm × 25 mm II	1.0	0.31
Cu foil 25 mm × 25 mm III (sanded)	1.0	1.10
Cu foil 8 mm × 25 mm I	3.0	1.01
Cu foil 8 mm × 25 mm II	1.6	0.83
Cu foil 8 mm × 10 mm I	1.7	1.15
Cu foil 8 mm × 10 mm II	1.6	1.12
milled I	1.0	2.46
milled II	1.0	3.26
milled III	2.7	1.24

For one sample with a copper piece of 25 mm × 25 mm, the copper strip is sanded. This roughens the surface and is expected to increase the mechanical stability of the connection. Considering these results only, the samples where both parts are milled appear to yield the best results. However, close examination of all samples shows that the connection of these samples failed in a different way compared to the other samples. For samples failing at higher forces, cohesive failure is the reason for the breakage. In these cases, the mat is torn apart. For samples that failed after a lower mechanical force is applied, adhesive failure is the cause of the breakage. The CF mat is almost or completely intact. Closeup views of these two cases are shown in Figure 5.32. These tests show that the glue layer thickness may need to be increased to strengthen the adhesive bond between the two parts.

(a) Sample pair after tensile test where the CF mat is torn.

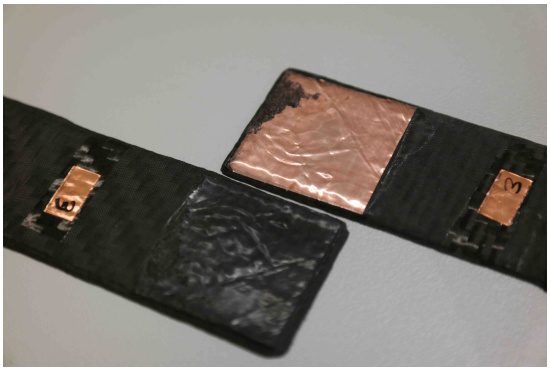

(b) Sample pair after tensile test where the CF mat remains mainly intact.

Figure 5.32: Comparison of cohesive and adhesive failure of the connection after tensile test.

Lap Joint Tests With Real-size Glue Area

After these first tests, samples pairs are created with a real-size glue area of 3 cm × 8 cm. For these samples, circular copper pads with a diameter of 2 cm are co-cured to the part representing the service tray. The circular shape increases the area without copper which results in better mechanical stability of the glued connection. In addition, the coefficient of thermal expansion is the same in all directions. The circular shape is therefore chosen over a rectangular shape. The surface of the other part of the sample pair is milled as described before and the two components are glued together with a CF mat. An example of such a sample pair with the CF mat before it is glued together is shown in Figure 5.33.

For these samples, the thickness of the applied glue layer is increased to 300 µm. In addition to the samples with circular copper pads, samples are created where the part representing the service tray is sanded using sanding paper. This option presents another alternative to obtain an electrically conductive surface as it also exposes the fibers. In addition, it gives the opportunity to study the mechanical behavior of the thicker glue layer independent of the co-cured copper pads.

The results of the electrical resistance measurements and the lap joint tests of these samples are summarized in Table 5.7.

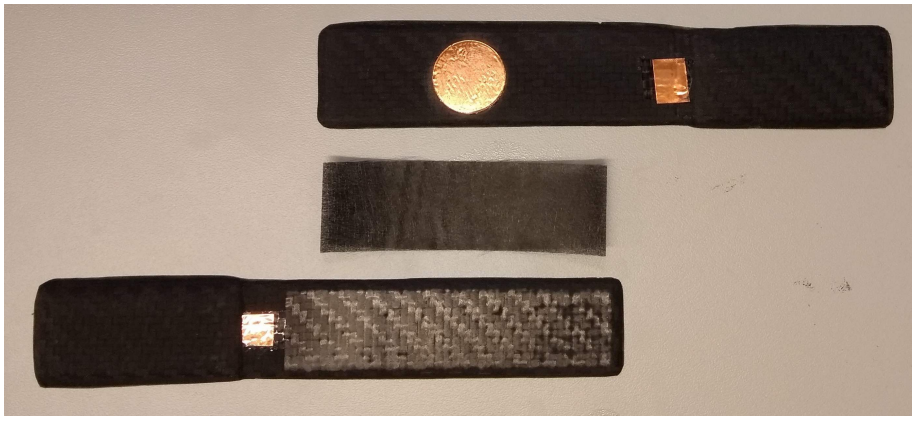

Figure 5.33: Sample pair for a lap joint test with a circular copper piece co-cured to the part representing the service tray and a milled surface for the part representing the wheel. The CF mat used to realize the electrically glued connection between the two parts is shown in the middle.

Table 5.7: Results of the electrical resistance measurements and the tensile tests for sample pairs with a glue layer of 3 cm × 8 cm and a thickness of 300 µm.

Electrically conductive surface option	**Electrical Resistance** [Ω]	**Applied Force Until Failure** [kN]
circular Cu I	1.2	8.18
circular Cu II	1.2	7.34
sanded I	1.2	8.40
sanded II	1.5	7.55

These tests suggest that the increase of the glue layer thickness leads to a considerable improvement of the mechanical strength of the glued connection. The final design of the service trays therefore employs a thickness of the glue layer of 300 µm.

Both options yield similar results for the applied force and the electrical resistance. However, safety concerns arise due to CF dusts that are created when sanding or milling the service tray. This can be avoided when co-curing a circular copper pad to surface of the service tray. As this method also requires less preparation steps, it is chosen as baseline approach.

5.3.5 Service Tray for ITk Endcap System Test Setup

The first service tray that was built and machined is be used for the ITk strip endcap system test setup. For the system test setup, an eighth slice of the endcap is built to test the interplay of the different components. It is a combined effort of DESY, Nikhef (Nationaal instituut voor subatomaire fysica) and IFIC (Instituto de Física Corpuscular). The corresponding mechanical structure shown in Figure 5.34(a) is equipped with 12 petals as shown in Figure 5.34(b).

(a) Mechanical structure of the system test setup built at Nikhef.

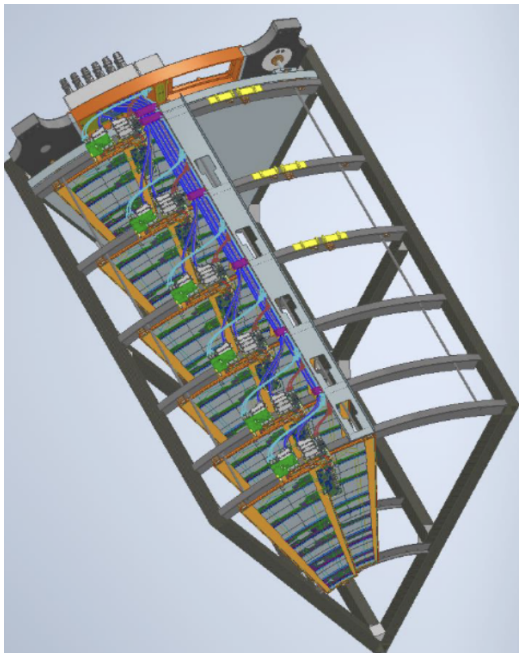

(b) System test setup including petals.

Figure 5.34: ITk strip endcap system test setup.

The setup is designed to be as similar as possible to that of the full endcap. The design also foresees electrical services for powering the detector modules and their read-out, as well as cooling services based on a custom CO_2 cooling machine. The entire structure will be surrounded by a thermal enclosure which also serves as Faraday cage. The system test setup also offers the possibility to test the petal insertion tool designed to facilitate loading the petals into the mechanical structure.

Its mechanical structure is currently being assembled and the petals will be installed in the system test setup in 2022. The endcap system test is first run on its own and will then be shipped to CERN where it can be combined with the barrel system test setup. It will also be used for training purposes during ITk operation.

A close-up view of the service tray for the system test setup is shown in Figure 5.35. It shows the inside and the outside of the tray with the various copper pads for the electrical connections. This service tray is integrated in the mechanical structure of the system test setup at Nikhef.

5.3.6 Production of the Service Trays

Finally, the 16 service trays for the two endcaps are produced following the manufacturing procedure described in Section 5.3.1. The service trays are built according to the updated design discussed in Section 5.3.2 to ensure a high mechanical strength. They are then machined to introduce the cutouts and remove superfluous material at the edges of the trays. After machining, the dimensions of each tray are measured as shown in Figure 5.36.

(a) Inside of the service tray.

(b) Outside of the service tray.

Figure 5.35: The system test setup service tray with the opening facing upwards (a) and downwards (b) showing the copper pieces at the different positions.

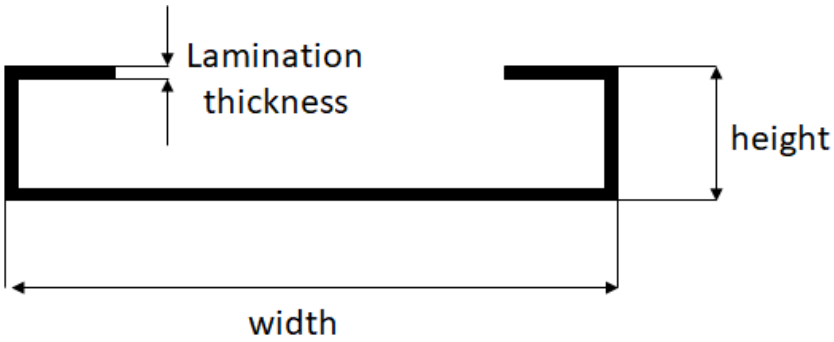

Figure 5.36: Service tray dimensions measured in quality inspection.

The width and height of each tray needs to be within the envelope as defined in the specifications as 80 mm and 20 mm. The width of the 16 service tray ranges between 79.25 mm and 79.60 mm. The height of the service trays ranges between 18.10 mm and 18.33 mm. The width and height are within the required envelope for all service trays. The lamination thickness ranges between 1.58 mm and 1.68 mm as targeted. The measurements of the width, height and lamination thickness of each service tray are shown in Table 5.8. The small variations of the dimensions show the high reproducibility obtained through the manufacturing procedure.

Table 5.8: Width, height and lamination thickness measurements of the service trays.

Service tray number	**Width [mm]**	**Height [mm]**	**Lamination thickness [mm]**
1	79.35	18.20	1.60
2	79.30	18.20	1.60
3	79.40	18.21	1.60
4	79.40	18.10	1.60
5	79.39	18.27	1.68
6	79.30	18.13	1.60
7	79.37	18.30	1.60
8	79.33	18.20	1.60
9	79.37	18.20	1.58
10	79.60	18.32	1.67
11	79.25	18.30	1.58
12	79.52	18.20	1.60
13	79.35	18.20	1.62
14	79.35	18.24	1.62
15	79.35	18.24	1.62
16	79.30	18.33	1.62

Additionally, the electrical resistance is measured between different combinations of copper pads and is below 2.5 Ω for all of these combinations. The service trays for the endcaps after machining are shown in Figure 5.37.

Figure 5.37: Final service trays after machining.

The 16 service trays for the endcaps will be assembled with the other components of the endcap structure at Nikhef. For the connections of the service trays to the wheels, the stiffening disk and the cooling pipes, the baseline methods defined in Section 5.3.3 and Section 5.3.4 are followed. These ensure the low electrical resistance path between the components as required. The assembly of the endcap global structure is planned to be completed in 2022 and the installation of the petals in the endcap will start shortly after. The full endcaps will then be shipped to CERN. The timeline currently foresees that the endcaps will be installed in the ATLAS detector in 2026 and that data taking with the ITk installed will start in 2029.

CHAPTER 6

Search for Heavy Resonances in Four-Top-Quark Final States

The analysis presented in this chapter investigates signatures with four top quarks for the presence of heavy resonances. The analysis strategy and the methods used to estimate contributions from the SM are described. The data and MC samples used in the analysis and the selections applied to them are presented. The statistical methods employed in the interpretation are summarized and tests of the chosen statistical model are discussed. The results are presented in terms of a search for new physics with minimal model dependence. Finally, the simplified model of a top-philic resonance introduced in Section 2.3.3 and referred to as $t\bar{t}Z'$ model is used for a model dependent interpretation. The results presented in this chapter are published in Ref. [4].

6.1 Motivation

Searches with top quarks are of particular interest because of high mass of the top quark and the corresponding large coupling to the Higgs boson. As a result, processes involving top quarks allow to further investigate the mechanism of electroweak symmetry breaking and the properties of the Higgs boson. Better understanding of these could help to explain the hierarchy problem as described in Section 2.2. Further insights could arise from new particles that couple to the top quark.

A typical approach to search for such particles is to look for resonances that decay to a top quark pair. Previous searches for resonances decaying to top quarks have typically focused on production through light quarks [109, 110]. This production mode requires a sizeable coupling between the new resonances and the lighter quarks. If the coupling to the lighter quarks is however suppressed, the resonance would mainly be produced through a pair of top quarks. In this case, the resonance is produced in association with another top quark pair resulting in four top quarks in the final state. These rare processes can now be studied with the large data set collected in Run 2 of the LHC, opening up new possibilities for discoveries of new particles. Recent evidence of the SM production of four top quarks [3] motivates the investigation of potential BSM contributions to this final state. Different models of top-philic resonances have been studied in previous analyses to investigate the

four-top-quark final state with no signs of BSM contributions so far [111, 112].

6.2 Analysis Strategy

Full Run 2 data collected by the ATLAS detector in the years 2015-2018 at a center-of-mass energy of 13 TeV is used in this analysis which corresponds to 139 fb^{-1}. This search targets top-philic heavy resonances in the mass range between 1 TeV and 3.2 TeV resulting in four top quarks in the final state. As the top quark can decay leptonically or hadronically, different combinations for the final decay products arise. The search presented here investigates the semi-leptonic final state where the resonance top quarks and one of the spectator top quarks decay hadronically while the other spectator top quark decays leptonically. The unique feature of the analysis presented here is the explicit reconstruction of such a resonance which allows for a search with minimal model dependence. The two top quarks from the resonance decay are expected to be boosted while the two spectator top quarks are expected to have lower momenta. A top-philic resonance could be observed as an excess over the steeply falling background distribution of the invariant mass m_{JJ} of the two reclustered jets used to collect the top decay products described in detail in Section 6.4.1. Excesses over the background distribution are searched for without relying on an explicit signal model. The distribution of m_{JJ} is shown in Figure 6.1 for the background split into the different components and the signal for the six resonance masses considered in this analysis.

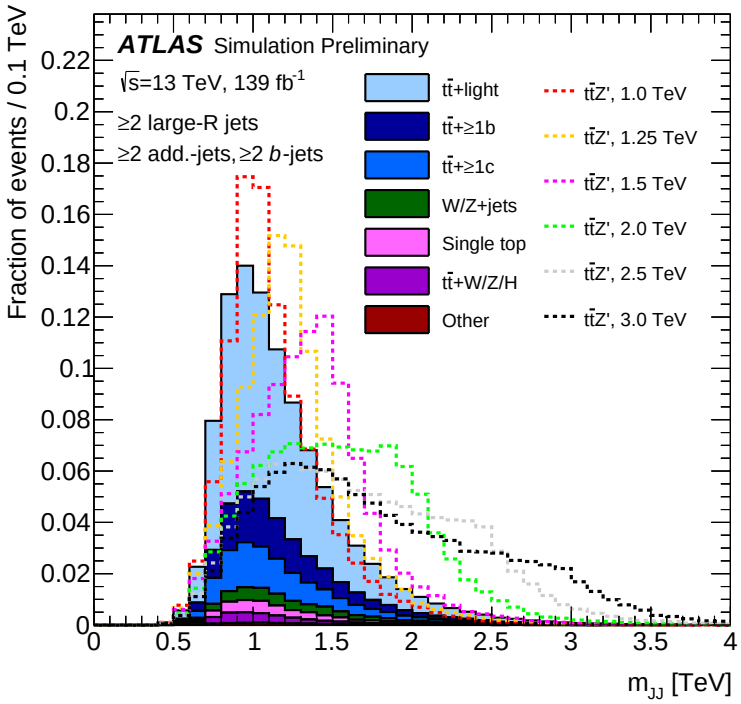

Figure 6.1: The m_{JJ} distribution for the background split in its different components and the signal for the six resonance masses. Figure taken from Ref. [4].

6.3 Data Samples and Monte Carlo Modeling

6.3.1 Data Samples

The data analyzed in this search was collected in the years 2015-2018 in pp collisions at $\sqrt{s} = 13$ TeV center-of-mass energy with 25 ns bunch spacing by the ATLAS detector. It corresponds to an integrated luminosity of 139 fb^{-1} with an uncertainty of 1.7 % [113]. All events contributing to the data set used in this analysis were recorded when the required quality criteria were fulfilled. These criteria ensure that all detector subsystems were operational and the beam conditions were stable.

6.3.2 Monte Carlo Simulated Events

Events simulated with MC are used in this analysis as part of the background estimate and to test the performance of the statistical model. Separate MC samples are produced to simulate the different background contributions and signal samples.

The largest background contributions after the preselection criteria are processes with $t\bar{t}$+jets. Other smaller backgrounds are processes with V+jets (with $V = W, Z$), single top (especially tW), a $t\bar{t}$ pair with a W, Z or H, diboson production (WW, WZ, ZZ) and the SM production of four top quarks. The samples are either produced using a full simulation of the ATLAS detector [114] based on GEANT 4 [61] or a faster simulation [115]. The simulated data sets undergo the same reconstruction algorithms and are further processed through the same analysis setup as the data.

Additional pp collisions are used to model the in- and out-of-time pileup in same or nearby bunch crossings. These additional collisions are produced with PYTHIA 8.186 [55] using the A2 tune of parameters [56] and the MSTW2008LO PDF set.

EVTGEN 1.2.0 [116] is used for generating top and charm quark decays in all samples except for those generated with SHERPA [54]. The NNPDF3.0NLO [117] set of PDFs is used unless specified otherwise.

The signal processes are simulated according to the simplified model discussed in 2.3.3 with MADGRAPH5_aMC@NLO 2.3.3 [59] at leading order with the PDF set NNPDF3.1LO [117]. The parton showering is simulated with PYTHIA 8.230 [55] using the A14 tune [118] and the NNPDF2.3LO [117] PDF set. As described in Section 2.3.3, for the first part of the model-dependent interpretation, the chirality parameter θ is set to $\pi/4$. The coupling between the resonance particle and the top quarks is set to $c_t = 1$. The narrow-width approximation is used resulting in a relative width of the resonance of 4 %. Samples for six different mass points are generated: 1.0 TeV, 1.25 TeV, 1.5 TeV, 2.0 TeV, 2.5 TeV and 3.0 TeV. For the second part of the model-dependent interpretation, the t-channel production as well as the production in association with tj or tW are included. Dedicated samples for these for different values of c_t and θ are generated.

The $t\bar{t}$ production is simulated with the POWHEG-hvq package for heavy quark production [119, 120] which uses the generator POWHEG-BOX 2 [60, 119, 121, 122] at NLO in QCD and the PDF set NNPDF3.0NLO [117]. The h_{damp} parameter which is set to the top quark mass m_{top} controls the p_{T} of the first additional emission.

For the parton showering of the $t\bar{t}$+jets sample, the A14 tune of PYTHIA 8.230 is used with the

NNPDF2.3LO [117] PDF set. The $t\bar{t}$+jets sample is further split according to the flavor of the jets in addition to the two top quarks. These split samples are only used for visualization purposes and to obtain the corresponding cross section uncertainties. Only jets outside of the two top quarks and not coming from a W-boson are classified in the following way. If at least one jet is matched within $\Delta R < 0.3$ to a b-hadron, the event is categorized as $t\bar{t}+\geq 1b$. If no such b-jet is identified, the event is categorized as $t\bar{t}+\geq 1c$ if at least one jet is matched within $\Delta R < 0.3$ to a c-hadron. All other events with two top quarks are labeled $t\bar{t}$+light.

The single-top sample is simulated with the Powheg-Box 2 generator at NLO in QCD and Pythia 8.230 using the A14 tune. Different setups are used for the different production modes. For the t-channel process the four-flavor scheme is used with the PDF set NNPDF3.0NLOnf4 [117]. In the four-flavor scheme, only the four light quarks can be part of the initial state while b-quarks can only be part of the final state. For the Wt channel and the s-channel, the five-flavor scheme is used with the the PDF set NNPDF3.0NLO [117]. In the five-flavor scheme, b-quarks are included in the initial state. In the nominal single-top sample, the "diagram removal" scheme [123] is applied to avoid double counting from the Wt and $t\bar{t}$ processes.

The $t\bar{t}H$ sample is simulated with the Powheg-Box generator at NLO with the PDF set NNPDF3.0NLO [117] interfaced with Pythia 8.230 using the A14 tune and the NNPDF2.3LO [117] PDF set. For the $t\bar{t}V$ samples, the MadGraph5_aMC@NLO 2.3.3 generator is used at NLO in QCD with the PDF set NNPDF3.0NLO [117] and Pythia 8.230 using the A14 tune with the NNPDF2.3LO [117] PDF set. The V+jets sample is produced using Sherpa 2.2.1 [54] with matrix elements at NLO-accuracy for up to two partons and LO-accuracy for up to four partons. The samples with VV final states are also simulated with Sherpa 2.2.1 [54]. The SM four top production $t\bar{t}t\bar{t}$ is simulated with MadGraph5_aMC@NLO 2.6.2 at NLO in QCD and the NNPDF3.1NLO [117] PDF set. For the parton shower, Pythia 8.230 is used with the A14 tune and the NNPDF2.3LO [117] PDF set. The tZ process is generated with the MadGraph5_aMC@NLO 2.6.2 generator at LO with the PDF set NNPDF3.0NLO [117] and Pythia 8.230 is used with the A14 tune as well as the NNPDF2.3LO [117] PDF set. The MC generators used for the different signal and background samples are summarized in Table 6.1.

Alternative Samples

Alternative MC samples are used to evaluate uncertainties on the MC generator and parton showering for the dominant processes $t\bar{t}$+jets and single-top-quark production. Further details on how the uncertainties are defined with these alternative samples can be found in Section 6.7. The uncertainty introduced by the choice of the MC generator is assessed with samples produced with MadGraph5_aMC@NLO where the parton shower is modeled with Pythia 8.230 as in the nominal samples. For assessing the effect of the parton shower modeling, separate samples are produced with the generator Powheg-Box 2 as for the nominal samples and Herwig 7.04 [57, 124] for the parton showering and hadronization. The H7UE set of tuned parameters is used [57] and the MMHT2014LO PDF set applied [125].

Table 6.1: Summary of MC generators used for the production of signal and background samples.

Sample	MC Generator + hadronization	PDF
BSM $t\bar{t}Z'$ signal	MadGraph5_aMC@NLO 2.3.3 (LO) + Pythia 8.230	NNPDF3.1 +A14
$t\bar{t}$+jets	Powheg-Box 2 + Pythia 8.230	NNPDF3.0 + A14
Single Top	Powheg-Box 2 + Pythia 8.230	NNPDF3.0 + A14
$t\bar{t}H$	Powheg-Box 2 + Pythia 8.230	NNPDF3.0 + A14
$t\bar{t}V$	MadGraph5_aMC@NLO 2.3.3 (NLO) + Pythia 8.210	NNPDF2.3 + A14
V+jets, VV	Sherpa 2.2.1	NNPDF3.0
SM $t\bar{t}t\bar{t}$	MadGraph5_aMC@NLO 2.6.2 (NLO) + Pythia 8.230	NNPDF3.1 + A14
tZ	MadGraph5_aMC@NLO 2.3.3 (LO) + Pythia 8.230	NNPDF3.0 + A14

6.4 Object Definition and Event Selection

This search investigates the final state where the two resonance top quarks as well as one spectator top quark decay hadronically while the other spectator top quark decays leptonically. This semi-leptonic final state makes up 42 % of four-top-quark events. Furthermore, requiring one lepton in the final state helps to reduce the QCD multi-jet background. Because of its large branching fraction and the additional power to control some of the backgrounds by requiring the presence of a lepton, this final state is chosen in this analysis. However, a large irreducible background remains from $t\bar{t}$+jets. The background estimation technique applied to describe it, is presented in Section 6.5.

6.4.1 Object Definition

The following objects are required in this analysis to enhance a potential signal contribution and to restrict the analysis to well-reconstructed and calibrated physics objects. The objects are reconstructed as described in Section 4.3. At least one vertex is required with at least two ID tracks and $p_{\mathrm{T}} > 500\,\mathrm{MeV}$. When several vertices are present, the vertex with the largest sum of the squared transverse momenta of the associated tracks is considered [126].

A combination of two single-lepton-triggers with different thresholds is used to select events with exactly one electron or muon. For the first trigger option, the leptons need to satisfy low transverse momentum p_{T} thresholds as well as low identification and isolation requirements. For the second option, they need to satisfy higher p_{T} thresholds and a looser identification criterion with no isolation requirement. Different minimum p_{T} requirements between 20 GeV and 26 GeV are applied for different data-taking periods and lepton flavors [127, 128]. The requirement on the transverse impact

parameter over its estimated uncertainty $|d_0|/\sigma(d_0)$ is less than five for electron candidates and less than three for muon candidates. The longitudinal impact parameter z_0 has to be $|z_0 \sin(\theta)| < 0.5\,\text{mm}$ for candidates of both lepton flavors. The electrons are identified with the *Tight* working point of the LH-identification and isolated using the *FixedCutTight* working point. The muons are identified with the *Medium* quality criteria and isolated using the *FixedCutTightTrackOnly* working point.

Small-radius jets constructed with the anti-k_t algorithm with radius $R = 0.4$ are required to have $p_\text{T} > 25\,\text{GeV}$ and $|\eta| < 2.5$. RC jets with a large radius parameter of $R = 1$ are created from small-radius jets and serve as proxies for the top quarks from the resonance decay. The b-jets arising from the top quark decays are selected with the DL1r algorithm [93] using the 77 % efficiency working point. They can be inside or outside of an RC jet. Small-radius jets outside of the two RC jets are expected from the spectator top quarks. They are considered to be outside of an RC jet if their distance from an RC jet is $\Delta R > 1$ and are referred to as *additional jets* in the following.

6.4.2 Object Overlap Removal

As a single detector response can be assigned to multiple objects, a sequential overlap removal is applied. First, electrons are removed that share a track with a muon candidate. Next, the jet with $\Delta R_y = \sqrt{(\Delta y)^2 + (\Delta\phi)^2} < 0.2$ which is closest to an electron is removed. Here, the rapidity y is defined as $y = \frac{1}{2}\ln(E + p_z)/(E - p_z)$ with the energy E and the the z-component of the momentum p_z. In the next step, electrons within $\Delta R_y = 0.4$ of a jet are removed. After that, jets with less than three associated tracks within $\Delta R_y = 0.2$ of a muon are removed. Finally, muons within $\Delta R_y = 0.4 + 10\,\text{GeV}/p_{\text{T}\,\mu}$ of a jet are removed.

6.4.3 Event Selection

The investigated semi-leptonic final state of a heavy top-philic resonance decay is characterized by a lepton as well as two higher and two lower transverse momenta top quarks which result in a large total number of jets. At preselection level, exactly one lepton with $p_\text{T} > 28\,\text{GeV}$ is required that matches the lepton that was triggered on. At least two RC jets are required to reconstruct the two hadronically decaying top quarks from the resonance. As the analysis targets heavy resonances which result in boosted top quarks, the RC jets need to have $p_\text{T} > 300\,\text{GeV}$, a mass $m > 100\,\text{GeV}$ and at least two constituent small-radius jets. The investigated final state leads to a large number of jets, therefore at least two additional jets and at least two b-tagged jets are required. Further event categorizations are introduced in the selections of the signal regions based on the numbers of additional and b-tagged jets to enhance the sensitivity to a signal contribution. The Feynman diagram of the signal process in the semi-leptonic four-top-quark final state is shown in Figure 6.2. The additional jets are highlighted in blue and the b-tagged jets are highlighted in orange.

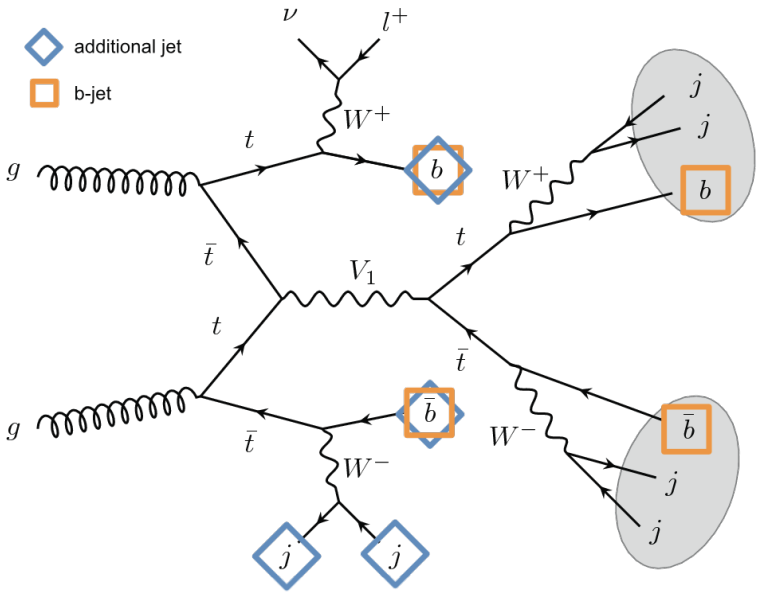

Figure 6.2: Feynman diagram of the semi-leptonic four-top-quark final state. Additional jets are highlighted in blue and b-tagged jets are highlighted in orange.

6.4.4 Signal Region Definition

The multiplicities of the additional jets and the b-tagged jets are used for discriminating between the signal and the background. Their distributions for the background and the signal for the six resonance masses are shown in Figure 6.3. The regions relevant for the analysis are defined by the number of additional jets and number of b-tagged jets. They are denoted as (Na,Mb), where N is the number of additional jets and M is the number of b-tagged jets, where N and M range from 2 to ≥ 4. The resulting nine regions are shown in a schematic overview in Figure 6.4.

The regions contain more relative expected signal with increasing number of additional and b-tagged jets. The region $(2a, 2b)$ therefore contains the least relative amount of signal, while the $(\geq 4a, \geq 4b)$ region contains the most relative amount of signal. The signal regions that are used for the final results of the search are highlighted in red. The control regions that are used to validate the analysis strategy before investigating the signal regions are shown in grey. The blue region is the most signal-depleted region called source region which is used for the background estimation described in the following.

6.5 Background Estimation

The largest background contribution in this analysis is due to top quark pair production in association with jets. Figure 6.5 shows the Feynman diagram of such a process with the production of the top quark pair in association with two b-tagged jets which most closely resembles the signal process of interest.

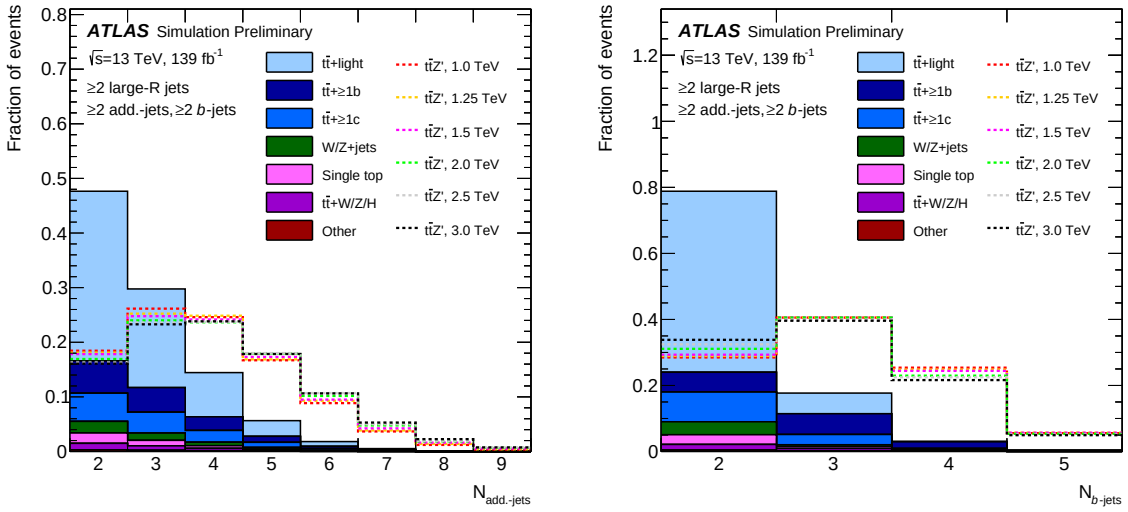

(a) Distributions of the number of additional jets.

(b) Distributions of the number of b-tagged jets.

Figure 6.3: The distributions of the additional jets and b-tagged jets at preselection for the background split in its different components and the signal for the six resonance masses. The distributions are normalized to unit area. Figure taken from Ref. [4].

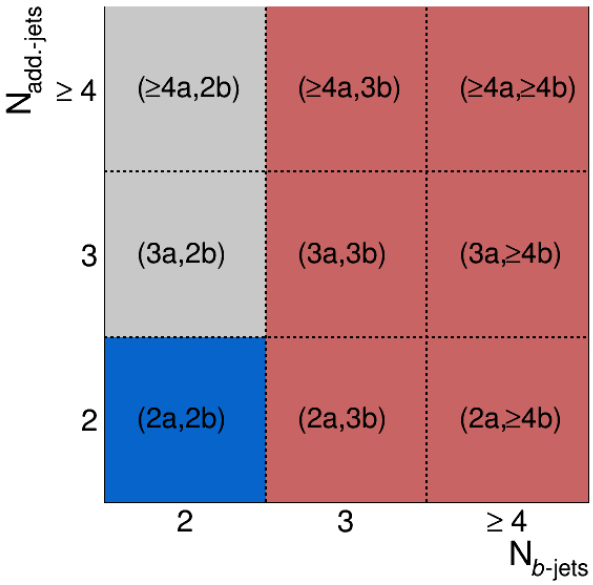

Figure 6.4: The nine regions defined in the analysis split by number of additional jets and number of b-tagged jets. The signal regions are highlighted in red and the source region is highlighted in blue. The notation used for the regions throughout this chapter is shown as well. Figure taken from Ref. [4].

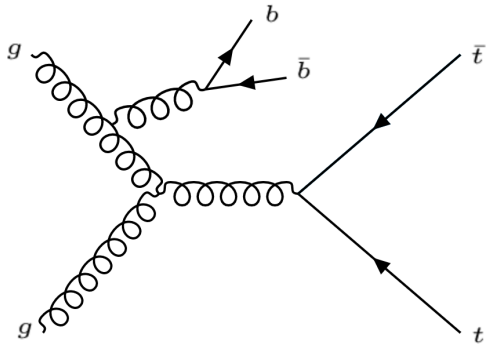

Figure 6.5: Feynman diagram of a background process with the production of the top quark pair in association with two b-tagged jets.

Depending on the flavor of the additional jets in the $t\bar{t}$+jets final state, this background is split into $t\bar{t}$+$\geq$1b, $t\bar{t}$+$\geq$1c and $t\bar{t}$+light. The different fractions of these contributions as well as other minor backgrounds for the different regions are shown in Figure 6.6 for each analysis region. The smaller backgrounds include single top processes, $t\bar{t}H$, $t\bar{t}V$ and V+jets. The background composition stays approximately the same for increasing number of additional jets. For increasing number of b-tagged jets, the fraction of $t\bar{t}$+light decreases strongly, while the fraction of $t\bar{t}$+$\geq$1b increases strongly. The fraction of $t\bar{t}$+$\geq$1c stays approximately the same.

While the MC simulations are necessary to obtain predictions for the expected distribution, it has been seen that $t\bar{t}$+jets processes are not modeled well [129]. The mismodeling is especially notable in the distributions of number of jets and number of b-tagged jets.

Therefore, the expected SM background in the m_{JJ} distribution is described by a data-driven method in this analysis instead of fully relying on the modeling obtained with simulations. The data-driven approach which is applied here, is based on a functional form fit to data in the most signal-depleted source region $(2a, 2b)$. The m_{JJ} range above 1 TeV is selected to avoid the "turn-on" in the distribution due to the RC jet p_T requirements. The background distribution falls steeply in this range which can be described well with a functional form fit. The template obtained with this fit is then extrapolated to the other regions. A necessary condition for such an extrapolation method is that the shapes of the m_{JJ} distribution in the signal regions and the source region agree. Although the background composition changes for different numbers of additional and b-tagged jets as shown in Figure 6.6, the shape similarity is confirmed in MC as shown in Figure 6.7.

The falling total background distribution is fit with a functional form. In this analysis, the dijet fit function is used which has been applied in dijet searches [130] and $t\bar{t}$ resonance searches [109]. It is defined as:

$$f(x) = (1-x)^{p_1} x^{p_2+p_3 log(x)}, \tag{6.1}$$

with $x = m_{JJ}/\sqrt{(s)}$ and $\sqrt{s} = 13$ TeV. The source region data with the dijet function as defined in Eq. 6.1 and fit to data is shown in Figure 6.8.

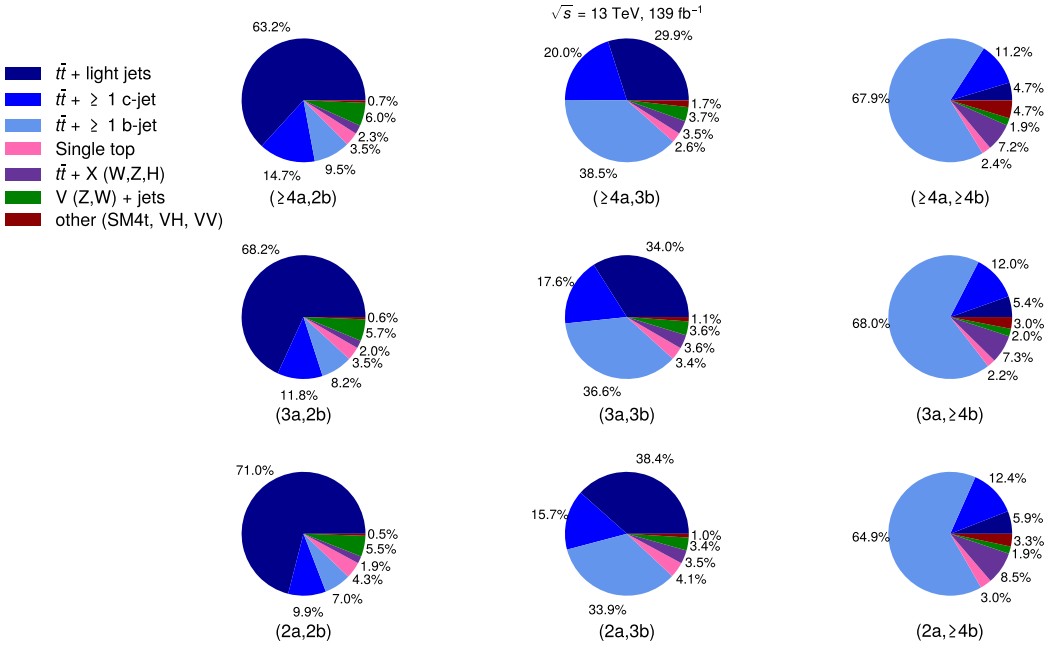

Figure 6.6: Fractions of background contributions in the analysis regions.

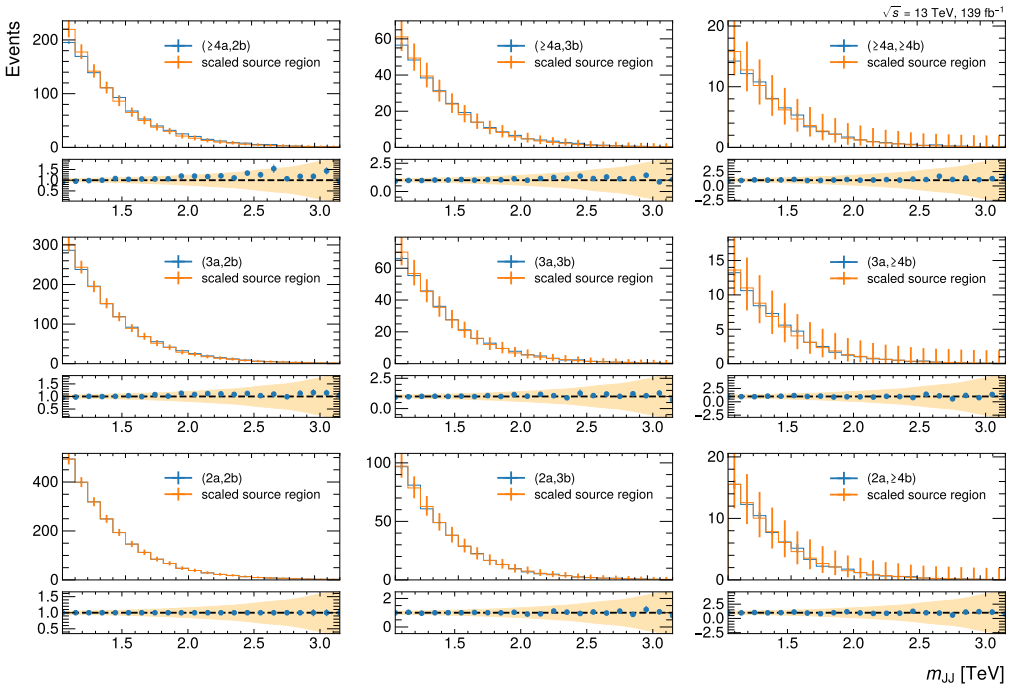

Figure 6.7: Shape comparison of simulated m_{JJ} distributions in source (orange) and analysis regions (blue). The distribution of the source region is scaled by the integral ratio to the respective region. The lower panel shows the ratio. The orange uncertainty band is the Poisson uncertainty of the denominator $(2a, 2b)$ scaled.

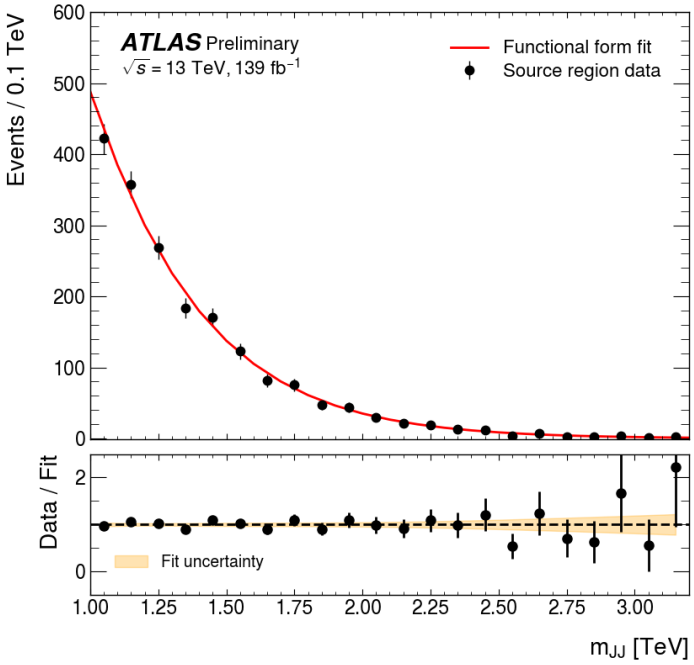

Figure 6.8: The m_{JJ} data distribution in the mass range 1 to 3.2 TeV in the source region with the corresponding dijet fit result. The lower panel shows the ratio of the data over the fit result with the corresponding uncertainty. Figure taken from Ref. [4].

The background estimation in each region is determined by the product of this dijet fit to source region data $f(m_{J\bar{J},i})$ multiplied with the extrapolation function $C^{\text{source}\to\text{reg}}(m_{J\bar{J},i})$ for the respective region:

$$B^{\text{reg}}(m_{J\bar{J},i}) = f(m_{J\bar{J},i}) \times C^{\text{source}\to\text{reg}}(m_{J\bar{J},i}). \tag{6.2}$$

The extrapolation functions are computed by taking the ratio of dijet functions as defined in Eq. 6.1 fit to MC simulated m_{JJ} distributions of the background in the respective signal and source region. The dijet fit results to MC distributions are shown for the $(2a, 2b)$ region and the $(\geq 4a, \geq 4b)$ region in Figure 6.9. The extrapolation functions $C^{\text{source}\to\text{reg}}(m_{J\bar{J},i})$ are then computed by taking the ratio of the two dijet functions to MC of signal and source region. The extrapolation functions for the analysis regions are shown in Figure 6.10.

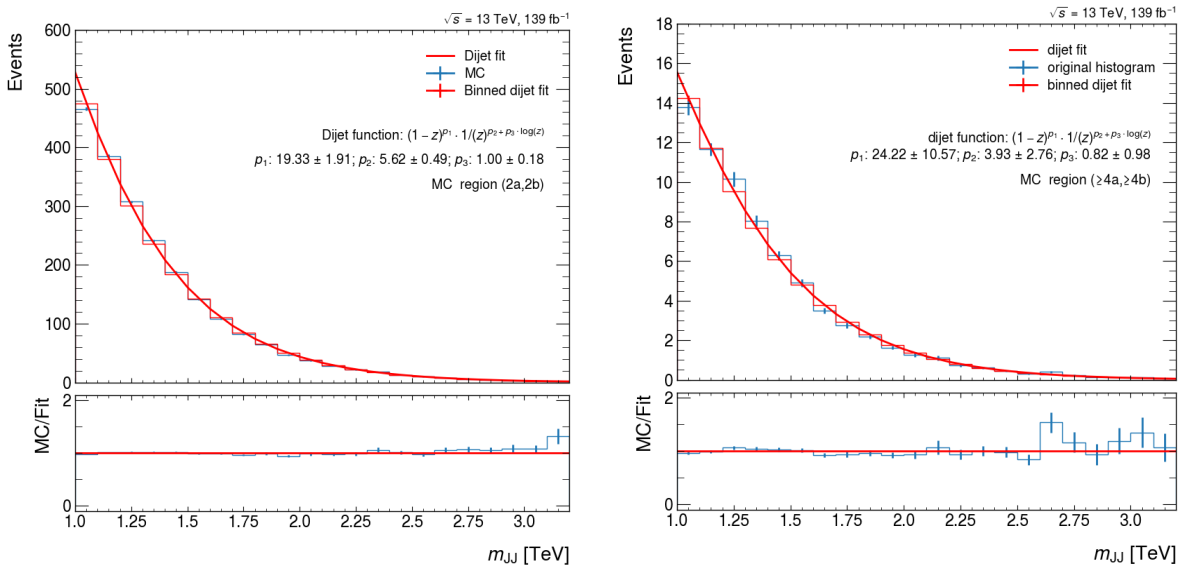

(a) Region $(2a, 2b)$. (b) Region $(\geq 4a, \geq 4b)$.

Figure 6.9: Dijet functions fit to source region $(2a, 2b)$ and signal region $(\geq 4a, \geq 4b)$ MC. The lower panel shows the ratio of the MC distribution and the djet fit.

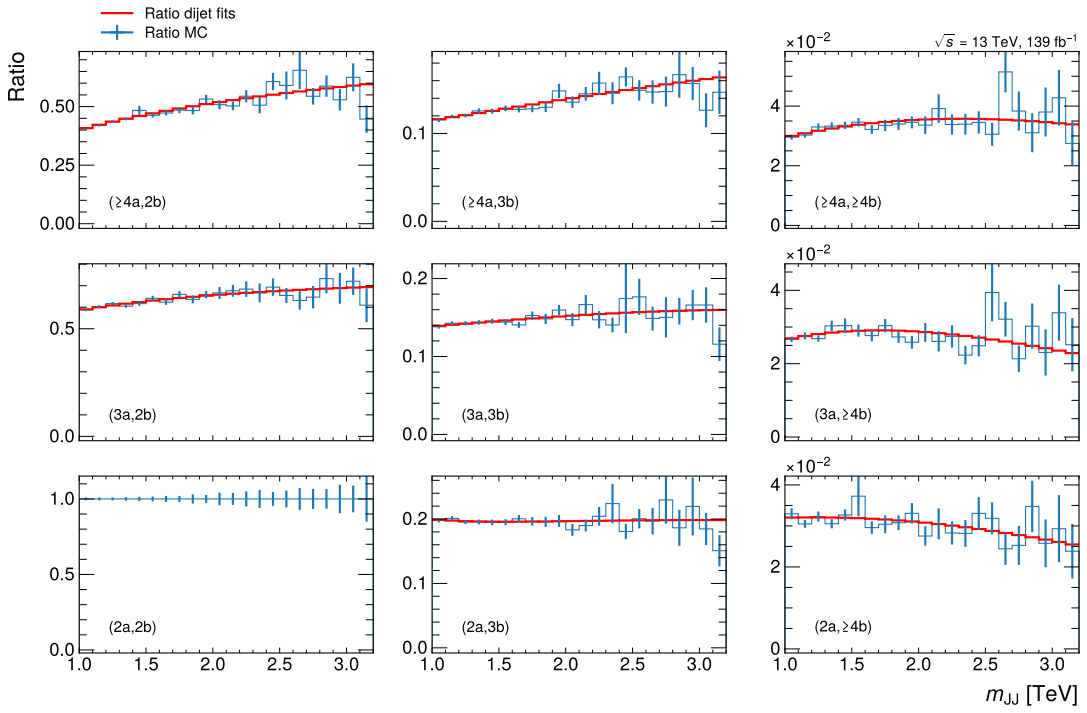

Figure 6.10: Extrapolation functions for all regions with uncertainties. For illustration, also the direct ratio of MC distributions is shown in blue.

6.6 Statistical Analysis

The statistical analysis is based on a hypothesis test to determine whether the data is compatible with a certain hypothesis. In the following, the null hypothesis denoted as H_0 assumes only SM background contributions and no signal contributions from new particles.

A test statistic is defined which quantifies the difference between the data and the hypothesis by assigning a single number to it. Then a distribution of the test statistic is computed under the assumption of H_0 with pseudoexperiments. In the case of typical hypothesis tests like the χ^2-test, analytical functions have been defined to describe these distributions. The value of the test statistic determined from the comparison of the data to H_0 is compared to the distribution of the test statistic based on H_0. The p-value is then defined as the probability of the test statistic t to be equal to or larger than the value t_0 obtained from the data under the assumption of H_0:

$$p = P(t \geq t_0|H_0). \tag{6.3}$$

The probabilities are distributed according to the probability density function $\rho(t|H_0)$ which can be obtained by normalizing the distribution of the test statistic. If the analytical description of $\rho(t|H_0)$ is known, the p-value can be computed as

$$p = \int_{t_0}^{\infty} \rho(t|H_0)\mathrm{d}t. \tag{6.4}$$

If the probability density function needs to be estimated by pseudoexperiments, the p-value is approximated by the binomial success probability. For N pseudoexperiments of which S have $t \geq t_0$, it is defined as

$$P(p|N,S) = \binom{N}{S} p^S (1/p)^{N-S}(1+N). \tag{6.5}$$

The p-value can then be used as decision algorithm. By assigning a cutoff value $\alpha \in [0,1]$, a hypothesis can be ruled out at the confidence level α if $\mathrm{p} \leq \alpha$. Equivalently, the Type-I error probability which is the probability to wrongly rule out H_0, is α if there exists a solution such that

$$\int_{t_0}^{\infty} \rho(t|H_0)\mathrm{d}t = \alpha. \tag{6.6}$$

It is important to note here, that if the test statistic follows a continuous function $\rho(t|H_0)$, this statement holds true for all values of α:

$$P(p \leq \alpha|H_0) = \alpha \;\forall\; \alpha. \tag{6.7}$$

Consequently, when H_0 holds, the p-value is a uniformly distributed random variable.

6.6.1 Profile Likelihood Fit

The statistical analysis is performed with a profile likelihood fit [131] using histograms to describe the $\mathrm{m_{JJ}}$ distribution. The expected number of events in a certain bin i expressed by the number of

signal events s_i and number of background events b_i can be parametrized as

$$N_i^{exp} = \mu \cdot s_i(\boldsymbol{\theta}) + b_i(\boldsymbol{\theta}). \tag{6.8}$$

Here, $\boldsymbol{\theta}$ are the Nuisance Parameters (NPs) and μ is the signal strength. The NPs are additional parameters that describe the systematic uncertainties. They can be parametrized by Gaussian distributions. The signal strength is a multiplicity factor of the chosen signal model. The background-only hypothesis corresponds to $\mu = 0$ and the nominal signal hypothesis to $\mu = 1$. The likelihood function is the product of the Poisson probabilities for the expected number of events and Gaussian distributions for the nuisance parameters

$$L(n^{obs}|\mu, \boldsymbol{\theta}) = \prod_i^N \frac{(\mu s_i + b_i)^{n_i}}{n_i!} e^{-(\mu s_i + b_i)} \prod_{j \in syst} \mathcal{G}(0, \theta_j). \tag{6.9}$$

The distributions of NPs are usually determined by additional measurements. By convention, they are centered around 0 with one Gaussian standard deviation corresponding to the distribution where the uncertainty is taken into account. The profile likelihood ratio is motivated by the Neyman-Pearson lemma [132] and is defined as

$$\lambda(\mu) = \frac{L(\mu, \hat{\hat{\boldsymbol{\theta}}})}{L(\hat{\mu}, \hat{\boldsymbol{\theta}})}. \tag{6.10}$$

In the nominator, $\hat{\hat{\boldsymbol{\theta}}}$ is the value of $\boldsymbol{\theta}$ at which the likelihood is maximized for a specific μ. Therefore, $\hat{\hat{\boldsymbol{\theta}}}$ is the conditional maximum likelihood estimator of $\boldsymbol{\theta}$. The demoninator is the maximized unconditional likelihood. Here, $\hat{\mu}$ and $\hat{\boldsymbol{\theta}}$ are the maximum likelihood estimators. The presence of NPs in the profile likelihood function corresponds to a loss of information about μ because of the systematic uncertainties.

The profile likelihood ratio ranges between $0 \leq \lambda(\mu) \leq 1$. Good agreement of the data and the specific value of μ is reached when $\lambda = 1$. The test statistic q_μ is then defined as

$$q_\mu = -2 \ln \lambda(\mu). \tag{6.11}$$

Incompatibility between data and μ is implied by larger values of q_μ. The negative logarithm ensures that q_μ increases monotonically. As defined for the general case above, the p-value is then defined as

$$p_\mu = \int_{q_{\mu,\text{obs}}}^{\infty} f(q_\mu|\mu) dq_\mu, \tag{6.12}$$

where $q_{\mu,obs}$ is the value of q_μ observed with the data and $f(q_\mu|\mu)$ is the probability density function of q_μ.

An important special case is when $\mu = 0$ which probes the background-only hypothesis. The resulting test statistics q_0 can be defined as

$$q_0 = \begin{cases} -2 \ln \lambda(0) & \text{if } \hat{\mu} \geq 0, \\ 0 & \text{if } \hat{\mu} < 0. \end{cases} \tag{6.13}$$

Defined in this way, only excesses over the background are probed. The corresponding p-value is defined as

$$p_0 = \int_{q_{0,\text{obs}}}^{\infty} f(q_0|0) \mathrm{d}q_0. \tag{6.14}$$

According to Wilks' theorem [133], q_μ approaches a χ^2 distribution and can therefore be evaluated. The p-value can then be converted to a significance Z as

$$Z = \Phi^{-1}(1 - p), \tag{6.15}$$

where Φ is the quantile of the standard Gaussian defined as $\Phi(x) = \frac{1}{\sqrt{2\pi}} \int_{-\infty}^{x} e^{-\frac{1}{2}t^2} \mathrm{d}t$.

6.6.2 BumpHunter Algorithm

For the model-independent interpretation of the analysis, the BumpHunter algorithm [134] is used. It is designed to indicate excesses in data over the background prediction which could arise from the resonant production of a new particle. The interval that shows the largest discrepancy between background and data is identified and assigned a p-value which corresponds to its Type-I error probability. A hypothesis test based on the p-value is performed to determine the consistency of the data with a certain hypothesis. In addition, it makes use of a hypothesis hypertest which takes the so-called trials factor into account by combining multiple hypothesis tests.

Trials Factor

Depending on the definition of a hypothesis test, it is susceptible to different features when comparing data to a hypothesis. Depending on the way it evaluates the compatibility, the resulting p-values can therefore lead to different conclusions. When comparing histograms for example, a test statistic can be chosen that is sensitive to deviations in a certain bin. If a bin with a significant fluctuation is selected, the hypothesis H_0 would be ruled out based on this test even if H_0 were true. Consequently, each bin counts as a trial with a chance to trigger a discovery. These many trials therefore have to be considered which is referred to as trials factor.

The trials factor can be taken into account by carrying out a hypertest which combines many hypothesis tests. For the example above, each test can scan different bins. Each of the individual hypothesis tests entering the hypertest result in a value of their test statistic with a corresponding p-value. If N of these tests are independent of each other, the probability that there is at least one p-value smaller than a certain value α is:

$$P(\text{at least one test has } p \leq \alpha) = \prod_{i=1}^{N} P(p_i > \alpha) \tag{6.16}$$

$$= 1 - (1 - \alpha)^N. \tag{6.17}$$

This also means that the Type-I error probability in this case is $1 - (1 - \alpha)^N$ and not α. Therefore, it is insufficient to choose the smallest of these p-values and a new test statistic needs to be defined instead. The result of this new test statistic can then be converted into a proper p-value that is equal to the Type-I error probability.

BumpHunter Test Statistic

The test statistic used in the BumpHunter algorithm for this purpose is defined as

$$t = -\log\left(\min_i(\text{p-value}_i)\right). \tag{6.18}$$

The negative logarithm ensures that the test statistic increases monotonically for decreasing $\min_i(\text{p-value}_i)$ and could be replaced by any monotonically increasing function. Regarding the choice of hypothesis tests entering the hypertest one has to find a balance between more features that could be compared with increasing number of hypothesis tests and smaller sensitivity. Using more hypothesis tests in the hypertest means more signal is required to obtain a specific p-value. The BumpHunter algorithm uses a collection of hypothesis tests which compare different interval sizes or bin numbers at different positions.

The BumpHunter Algorithm

First, the range scanned by BumpHunter and the possible interval sizes are defined. The interval width may vary between $[2, \frac{N_{\text{bins}}}{2}]$, where N_{bins} is the number of bins in the considered range. For a fixed interval at a certain position with a chosen width, the number of data events (d) and number of background events (b) are determined. The test statistic is defined as

$$t = \begin{cases} 0 & \text{if } d \leq b \\ f(d-b) & \text{if } d > b, \end{cases} \tag{6.19}$$

where f can be any monotonically increasing function. The corresponding p-value is

$$\text{p-value} = \begin{cases} 1 & \text{if } d \leq b \\ \mathcal{P}(d,b) & \text{if } d > b. \end{cases} \tag{6.20}$$

Here, the probability $\mathcal{P}(d,b)$ is defined as

$$\mathcal{P}(d,b) = \sum_{n=d}^{\infty} \frac{b^n}{n!} e^b = \Gamma(d,b), \text{ if } d \geq b. \tag{6.21}$$

The p-value can be computed directly from d and b, so it is not necessary to compute the test statistic first.

Changing the position of the interval and the interval size, these steps are repeated. The result is a collection of p-values which are used to compute the BumpHunter test statistic according to Eq. 6.18. Comparing the observed value to a distribution of test statistics obtained from pseudoexperiments based on H_0, the final BumpHunter p-value is determined.

In the analysis presented here, the background distributions entering the BumpHunter algorithm are obtained from a profile likelihood fit to data assuming the background-only hypothesis. With this approach, the systematic uncertainties can be included in the search for an excess without assuming a specific signal model. In case of an excess present in the data, the profile likelihood fit carried out in this way would accommodate for a part of the signal. The search for excesses with BumpHunter loses sensitivity but could identify large excesses over the data. Therefore, the search is more conservative in claiming a potential discovery. The BumpHunter p-values for the comparisons of data to the background prediction for this analysis in the different signal regions are shown in Section 6.9.2.

6.6.3 Upper Limit Computation

A typical way to present the results of a particle physics search is the upper limit. It defines the largest possible amount of signal that can be present in a hypothesis including signal and background contributions which is still ruled out by the data at a certain chosen confidence level (CL). The evaluation of the upper limits for the model-dependent interpretation of the analysis presented here is carried out according to the CL_s method [135]. It is based on the probability distribution function of $f(q) = -\ln(q)$ with the test statistic $q = L(s+b)/L(b)$. Here, $L(b)$ is the likelihood of the null hypothesis which is the background-only hypothesis. $L(s+b)$ is the likelihood of the hypothesis including signal and background contributions. The p-value of this hypothesis is defined as the probability of obtaining a value of q that is equal or larger than q_{obs}

$$p_{s+b} = P(q \geq q_{\text{obs}}|s+b) = \int_{q_{\text{obs}}}^{\infty} f(q|s+b)\mathrm{d}q. \tag{6.22}$$

Similarly, the p-value under the background-only hypothesis can be defined as

$$p_b = P(q \leq q_{\text{obs}}|b) = \int_{-\infty}^{q_{\text{obs}}} f(q|b)\mathrm{d}q. \tag{6.23}$$

An exclusion statement based on this p-value can be made at a confidence level $1-\alpha$ which is typically chosen to be 95 % and excluding the hypothesis assuming signal and background contributions if

$$p_{s+b} < \alpha. \tag{6.24}$$

This approach is called the CL_{s+b}-method. However, the CL_{s+b}-method reaches its limitations when only a small number of signal events is expected. In this case, the distributions of $f(q)$ under both hypotheses will overlap significantly. Sketched distributions of $f(q)$ for the hypothesis assuming signal and background contributions and the background-only hypothesis are shown in Figure 6.11.

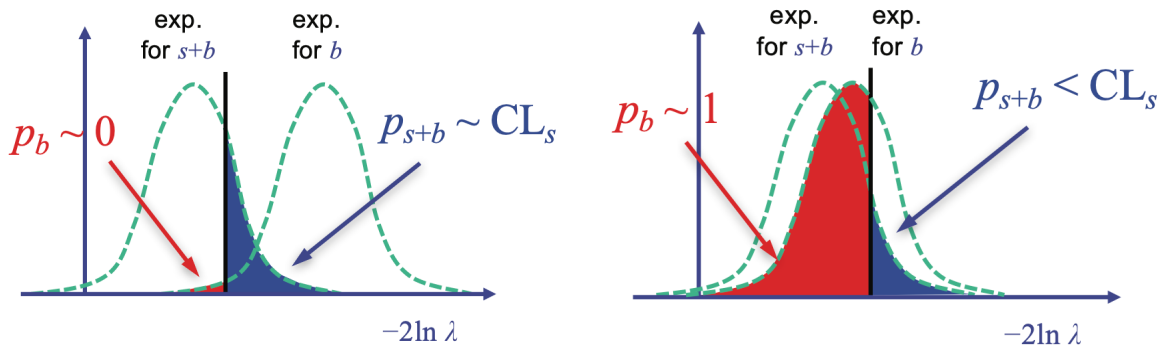

(a) For a large number of expected signal events the $f(q)$ distributions are clearly separated.

(b) For a small number of expected signal events the $f(q)$ distributions largely overlap.

Figure 6.11: Distributions of $f(q)$ under the hypothesis assuming signal and background contributions and the background-only hypothesis. Figure taken from Ref. [136].

If only a small number of signal events is expected, a small p_{s+b}-value could still be obtained with the CL_{s+b}-method. A specific hypothesis could thus be excluded although there is very little sensitivity to the signal. This can be avoided by applying the CL_s method instead and defining the quantity

$$CL_s = \frac{p_{s+b}}{1 - p_b} < \alpha. \tag{6.25}$$

A signal model is excluded at a certain confidence level α if $CL_s < \alpha$.

If the two $f(q)$ distributions are well separated, $1 - p_b$ is small and CL_s is close to p_{s+b}. However, if the expected signal is small, $1 - p_b$ becomes small and consequently CL_s becomes large. An exclusion is therefore avoided when there is little sensitivity to the signal model. It also follows from Eq. 6.25 that CL_s is always larger than p_{s+b}. Therefore, the CL_s method is a conservative approach.

6.7 Systematic Uncertainties

Multiple sources of uncertainty affect this search including experimental uncertainties from the detector, the reconstruction and calibration of the physics objects. Additional uncertainties arise from the MC simulations and the methods applied to model the expected m_{JJ} distribution. The systematic uncertainties can affect the normalization of the background and signal distributions as well as their shapes.

The nominal background estimate is based on the extrapolation functions which are obtained by taking the ratio of dijet fit functions which are fit to the MC simulated m_{JJ} background distributions in the signal and source regions. The systematic uncertainties are defined by similarly taking the ratio of dijet fit functions to MC simulated distributions using samples which include the effects of a specific uncertainty. The variations of the respective uncertainty are therefore obtained by applying alternative extrapolation functions in the background estimation. As for the nominal extrapolation functions, the alternative extrapolation functions are multiplied with the dijet function fit to data in the source region to obtain an alternative background estimate. These alternative background distributions then enter the statistical analysis as systematic uncertainties. Each systematic uncertainty leads to an NP in the profile likelihood fit. Some uncertainties are split into multiple components corresponding to multiple NPs as described below to distinguish the respective effects. One exception to this approach is the definition of the uncertainties related to the dijet fit function which are discussed separately in Section 6.7.3.

6.7.1 Experimental Uncertainties

The uncertainty on the luminosity of 1.7 % [113] applies only to the signal sample which is directly simulated with MC and is needed for the model-dependent interpretation. As the background is estimated by a functional form fit to data which is multiplied by a ratio of MC distributions, it is not affected by the luminosity uncertainty.

Further experimental uncertainties arise from the reconstruction of the different physics objects and corrections to the MC simulations. These uncertainties apply to both the background and signal processes.

Jet Uncertainties

Uncertainties regarding jets include effects on the Jet Energy Scale (JES), Jet Energy Resolution (JER) and Jet Vertex Tagging (JVT). A large number of uncertainties arises from the jet reconstruction and calibration carried out in the different steps described in Section 4.3.4. The uncertainties arising from JES calibration [137] are implemented as a reduced set of 29 NPs in this analysis. These include effects related to η-intercalibration, to the flavor of the jet and to pileup correction. For the JER uncertainties, a reduced set of nine NPs is used. They take into account uncertainties of the JER measurement and differences between data and simulation. The JVT uncertainty is estimated by varying the cut value of the dedicated JVT variable [138]. This uncertainty takes into account the contributions of any remaining pileup jets.

For the uncertainties from flavor tagging, a reduced set of eigenvector variations are used to obtain independent NPs. There are a total of 19 NPs related to flavor tagging corresponding to the b-, c- and light-jet flavor efficiency scale factors as well as the extrapolation of b- and c-tagging efficiency to higher p_T ranges.

Lepton Uncertainties

For electrons and muons, the uncertainties arise from differences in reconstruction, identification, isolation and trigger performances in data compared to MC. These differences are taken into account by computing dedicated scale factors with associated uncertainties. For the electrons, there are in total seven NPs which include the correction factors and additional uncertainties regarding the energy scale and energy resolution. For the muons, there are in total 13 NPs. They include the correction factors for the trigger, track-to-vertex association, identification and isolation efficiencies. Other muon uncertainties arise from inner detector track smearing, muon spectrometer track smearing, charge-independent scale momentum and the charge-dependent scale momentum.

Other Experimental Uncertainties

Uncertainties on the missing energy $E_{\mathrm{T}}^{\mathrm{miss}}$ are not included in this analysis, as $E_{\mathrm{T}}^{\mathrm{miss}}$ is neither part of the event selection nor the statistical analysis. Pileup modeling uncertainties arise from a reweighting that is carried out to match the number of additional pp interactions to that obtained from data. The uncertainties due to this reweighting cover deviations of the ratio of predicted over measured inelastic cross sections.

6.7.2 Theoretical Uncertainties

Theoretical uncertainties are included that affect the modeling of the different background components. The uncertainties on the predicted cross sections of the different background components are computed by increasing the respective component in the MC distributions used to calculate the extrapolation functions. The values chosen for the cross section uncertainties are summarized in Table 6.2. For $t\bar{t}W$, $t\bar{t}Z$ and $t\bar{t}H$, the values of the cross section uncertainties are motivated by Ref. [3, 139, 140]. The size of the uncertainty for V+jets is chosen following Ref. [141]. A conservative estimate on the uncertainty of single top production is motivated by the uncertainties arising from jet modeling of the large number of jets. The $t\bar{t}$+jets background processes are split into $t\bar{t}+\geq 1b$, $t\bar{t}+\geq 1c$ and $t\bar{t}$+light. The cross section uncertainties of the SM $t\bar{t}t\bar{t}$ component as well as the different $t\bar{t}$+jets components are selected according to the values chosen in the SM $t\bar{t}t\bar{t}$ analysis presented in Ref. [142]. For the processes VV and VH, a conservative cross section uncertainty of 50 % is applied.

Theoretical uncertainties related to the MC generator or parton shower modeling are included in the statistical model by recomputing the extrapolation functions using MC distributions simulated with an alternative generator or an alternative parton shower model. The uncertainty arising from the generator choice is estimated with samples generated with MadGraph5_aMC@NLO for the $t\bar{t}$+jets and single top components which are the main background components. The effects of the parton shower are estimated with alternative samples generated with Herwig 7 for the $t\bar{t}$+jets and single top components. As these are important uncertainties for the modeling of the main background $t\bar{t}$+jets, they are further split to address different effects. Both of these uncertainties are split into separate components for the $3b$- and $\geq 4b$-jets regions to account for the different fractions

Table 6.2: Cross-section uncertainties for the background processes and $t\bar{t}$ flavor composition uncertainties.

Background Process	Uncertainty
Single Top Quark	30 %
VV	50 %
VH	50 %
$t\bar{t}W$	60 %
$t\bar{t}Z$	15 %
$t\bar{t}H$	20 %
V+jets	59 %
SM $t\bar{t}t\bar{t}$	20 %
$t\bar{t}$+≥1b	50 %
$t\bar{t}$+≥1c	50 %
$t\bar{t}$+light	10 %

of $t\bar{t}$+≥1b, $t\bar{t}$+≥1c and $t\bar{t}$+light in these regions as observed in Figure 6.6. Separate components of these uncertainties are considered for the normalization and the m_{JJ} shape in the analysis regions. The described decorrelation scheme results in 4 NPs for the alternative generator uncertainty and 4 NPs for the alternative parton shower uncertainty.

Theoretical uncertainties arising from missing higher order QCD corrections are estimated by separately varying the renormalization and factorization scales and taking the envelope. Further uncertainties are related to the initial and final state radiation (ISR/FSR) modeling in the parton shower. They are obtained by varying the respective parameters of the A14 PS tune introduced in Section 6.3.2 and the factorization scale of the final state radiation. The PDF uncertainties are assessed by using the PDF4LHC systematic variations [143].

6.7.3 Dijet Fit Uncertainties

As the dijet fit plays a pivotal role in the background estimate, designated uncertainties are defined. The dijet fit function is used in the functional form fit to the source region data and for the computation of the extrapolation functions. For the fit to data, three independent NPs are obtained from the eigen-decomposition of the three fit parameters. These uncertainties are correlated among all signal regions as the fit to source region data has no dependence on the signal regions. The uncertainties for the dijet fits to MC which are used to compute the extrapolation functions are defined only for the nominal MC distributions. They are evaluated with toy distributions. The dijet fit is applied to each of these toy distributions and the central values of the three fit parameters are recorded. The eigen-decomposition of these central values is then computed to obtain the independent components. These variations are added to the dijet fit to the MC sample to obtain the final uncertainties. Separate uncertainties are defined for the dijet fits to MC in each signal regions as these are independent of each other.

As a result, there are three NPs for each of the six signal regions and three NPs for fit to MC in the source region, resulting in 21 NPs for the fits to MC. Together with the three NPs from the fit to source region data, there are in total 24 NPs from the dijet fit functions to data and MC distributions.

6.7.4 Signal Bias Uncertainty

For the model-dependent interpretation of the analysis, a dedicated signal bias uncertainty is defined. It takes into account a bias in the extracted signal strength μ arising from the background model. The bias in μ used to define the uncertainty is obtained from profile likelihood fits to pseudodata sampled around the background MC distributions. The signal template for the considered resonance mass is then multiplied with the bias in μ which is added to the nominal background estimate to define this uncertainty. Details on the evaluation of the signal bias uncertainty can be found in Section 6.8.4.

6.8 Background Model Validation

A series of tests has been carried out to validate the background model, using simulated events and validation region data. The results of these tests are presented in this section.

6.8.1 Alternative Functional Forms

Alternative fit functions are tested to confirm the choice of the three parameter dijet function as defined in Eq. 6.1. The alternative fit functions considered here are the dijet function with four parameters

$$f(x) = (1-x)^{p_1} \times x^{p_2+p_3 \log(x)+p_4 \log(x)^2} \tag{6.26}$$

and a function introduced by the UA2 collaboration [144]

$$f(x) = \frac{p_0}{x^{p_1}} \times e^{-p_2 x - p_3 x^2}. \tag{6.27}$$

The results of fitting either of these two functions to source region data in comparison to the fit of the dijet function with three parameters are shown in Figure 6.12.

The performance of the dijet function with four parameters compared to the one with three parameters is quantified by computing the profile likelihood ratio as presented in Ref. [145]. It is defined as

$$\lambda_F = -2 \log \frac{L_{\text{nom}}}{L_{\text{alt}}}, \tag{6.28}$$

where L_{nom} is the likelihood of the fit using the dijet function with three parameters and L_{alt} is the likelihood of the fit using the dijet function with four parameters. For this test, the alternative fit function is preferred if the p-value corresponding to the observed profile likelihood ratio is smaller

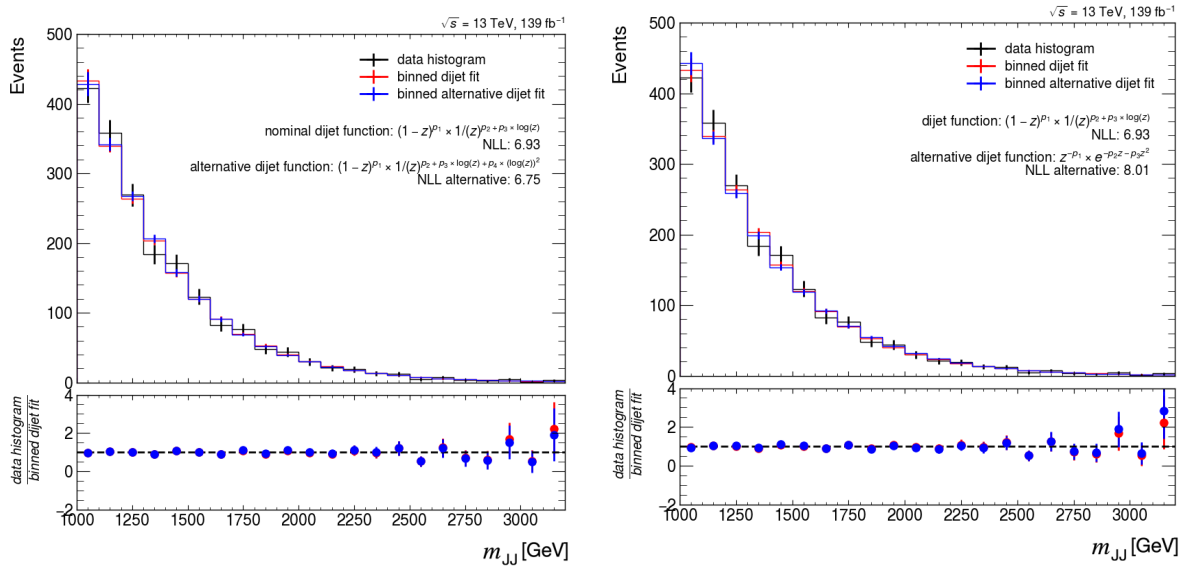

(a) Dijet function with four parameters.

(b) UA2 function.

Figure 6.12: Alternative functional forms fit to data in the source region $(2a, 2b)$. The dijet function with three parameters fit to the data is shown for comparison. The lower panels show the ratios of the data over the applied functional form.

than 0.05. The resulting p-value computed from the negative log-likelihoods is 0.54. This implies that the alternative fit function does not provide a better description of the data than the nominal fit function. Therefore, the dijet function with three parameters is used throughout the analysis.

The likelihood ratio as measure to compare two fit functions is only defined if the two functions belong to the same functional family. It can therefore not be applied to the comparison with the UA2 function. Here, only a quantitative comparison is possible, which is demonstrated in Figure 6.12(b). The alternative fit function does not show a clear advantage over the nominal function.

6.8.2 Validation of the Statistical Model

After defining the analysis strategy and the profile likelihood fit with the systematic uncertainties, multiple tests are carried out to probe the performance of the statistical model. Pseudodata generated from MC simulated distributions are used as proxies for the expected data distributions. The tests are split into two groups, the model-agnostic and model-dependent tests. This setup of two test phases is in line with the analysis strategy and data interpretation which will also be carried out in two steps, without and with a specific model assumption. In the first group of tests, the fit quality is studied and a generic search for discrepancies between pseudodata and background model is performed. For the model-dependent tests, an explicit signal model is assumed and the tests show the performance of the fit model in fitting this specific signal to the pseudodata. The results of the tests which are carried out for all signals with different resonance masses are shown here for the resonance signal with a mass of 1.5 TeV as representative examples. This signal is chosen as its m_{JJ}

distribution shows a maximum at the resonance mass which is at the center of the considered mass range. The same tests using the other resonance signal masses lead to similar conclusions.

For the tests using pseudodata shown in this section only five instead of six signal regions are included. The region $(2a, 3b)$ was considered as control region at first and only included in the statistical model for producing the final results using data which are shown in Section 6.9.

Pseudodata Generation

In the tests described in the following, the fit model is probed using pseudodata. This pseudodata is generated based on the MC distributions as described in Section 6.3.2. It can either be sampled from background distributions only or background distributions with a specific resonance mass signal distribution added. The latter represents the case where a signal is present in the data. For each test, 500 pseudodata sets are sampled to take into account statistical variations. The sampling is carried out in two steps and for each bin of the simulated distribution separately. First, each bin is sampled from a Gaussian distribution with a mean equal to the bin content of the MC distribution and width equal to the statistical uncertainty of the bin. Next, this value is varied by sampling from a Poisson distribution.

6.8.3 Model Agnostic Tests

For the following tests, no specific signal model is assumed. However, the m_{JJ} distribution is studied and a specific mass range is selected according to the analysis strategy which implicitly assumes certain model characteristics.

Goodness of Fit Test

The Goodness of Fit (GoF) test gives a measure of how well the (pseudo)data is described by the background distribution. The GoF is determined by comparing the likelihood of the nominal fit to that of a saturated model. The saturated model is defined such that it allows the fit to adjust to the data without the profile likelihood punishments of pulled nuisance parameters. It is therefore designed to perfectly accommodate for the data. The pseudodata is created based on background-only MC simulated distributions. For this analysis, the GoF test is considered passed if at most 10 % of the pseudodata sets have a p-value less than 0.05. The GoF p-value distribution is shown in Figure 6.13 and demonstrates that the GoF-based criterion is satisfied.

BumpHunter Results for Pseudodata With No Signal Injected

The first interpretation phase of the search is aimed at identifying deviations of the observed data from the background prediction. For this phase, the BumpHunter algorithm is used without assuming a specific signal model.

If there is an excess of data over the background, the interval with the largest deviation has a small BumpHunter p-value. In any case, the algorithm identifies the interval with the largest deviation.

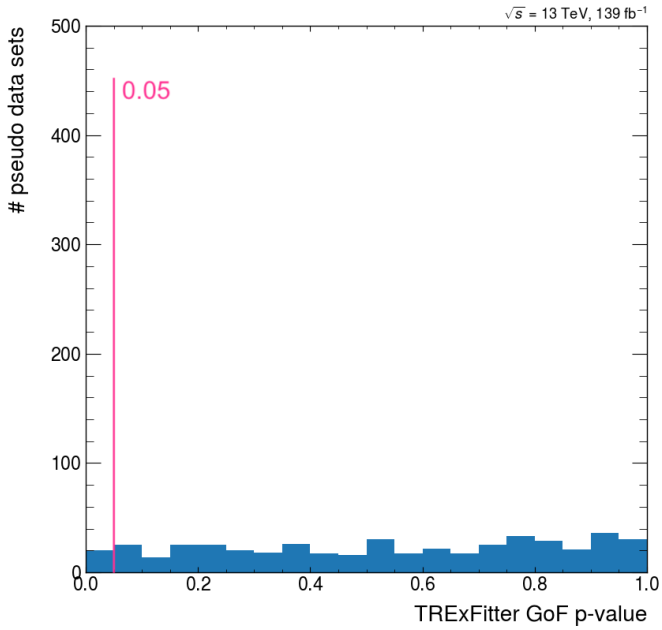

Figure 6.13: Goodness of fit p-values for 500 pseudodata sets sampled from the MC background distributions.

An example for a pseudodata set sampled from the MC simulated background m_{JJ} distributions compared to the post-fit background estimation is shown in Figure 6.14.

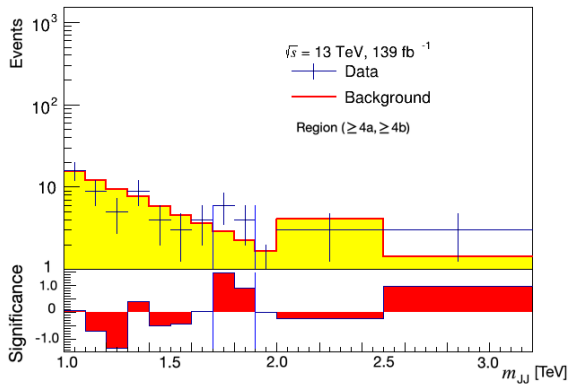

(a) m_{JJ} distribution with most discrepant interval highlighted.

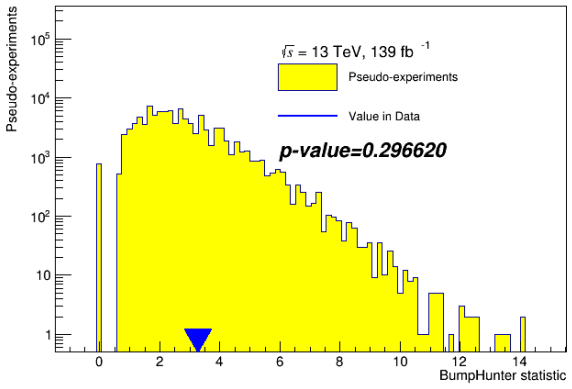

(b) BumpHunter test statistic with the observed value and the corresponding p-value.

Figure 6.14: BumpHunter results showing (a) the most discrepant interval in the m_{JJ} distribution and (b) the BumpHunter test statistic for an example pseudodata set generated from the background MC distributions in the region $(\geq 4a, \geq 4b)$. In (a), the BumpHunter interval is indicated by the blue vertical lines. The lower panel shows the corresponding significance. In (b), the observed value of the BumpHunter test statistic is indicated by the blue arrow and the corresponding p-value is printed.

The most discrepant intervals and the corresponding p-values are computed for 500 pseudodata sets. For a large number of pseudodata sets where there is no deviation between the pseudodata and the background prediction, the distribution of p-values is expected to be uniform. The test is considered to be passed when no more than 10 % of the pseudodata sets have a p-value smaller than 0.05. The intervals are expected to be distributed over the studied mass range. The intervals are shown in Figure 6.15 versus the p-value. Each pseudodata set in a specific region results in one interval identified by the BumpHunter algorithm as most discrepant interval with a corresponding p-value. A marker is set for each mass value within the interval at that p-value. The intervals are spread over the mass range and no specific range is clearly favored. Individual intervals are assigned small p-values by the algorithm but for the majority of pseudodata sets, there is no trend towards small p-values. The described behavior is observed in all regions.

The distribution of only the p-values are shown in Figure 6.16. They are identical to the p-values shown in Figure 6.15 but allow to evaluate the test requirement. The p-values are evenly distributed between 0 and 1. This is expected when the tested data is described well by the background hypothesis distribution it is compared to. No difference between the analysis regions is observed. The test is passed since for all regions less than 10 % of the pseudodata sets have a p-value < 0.05.

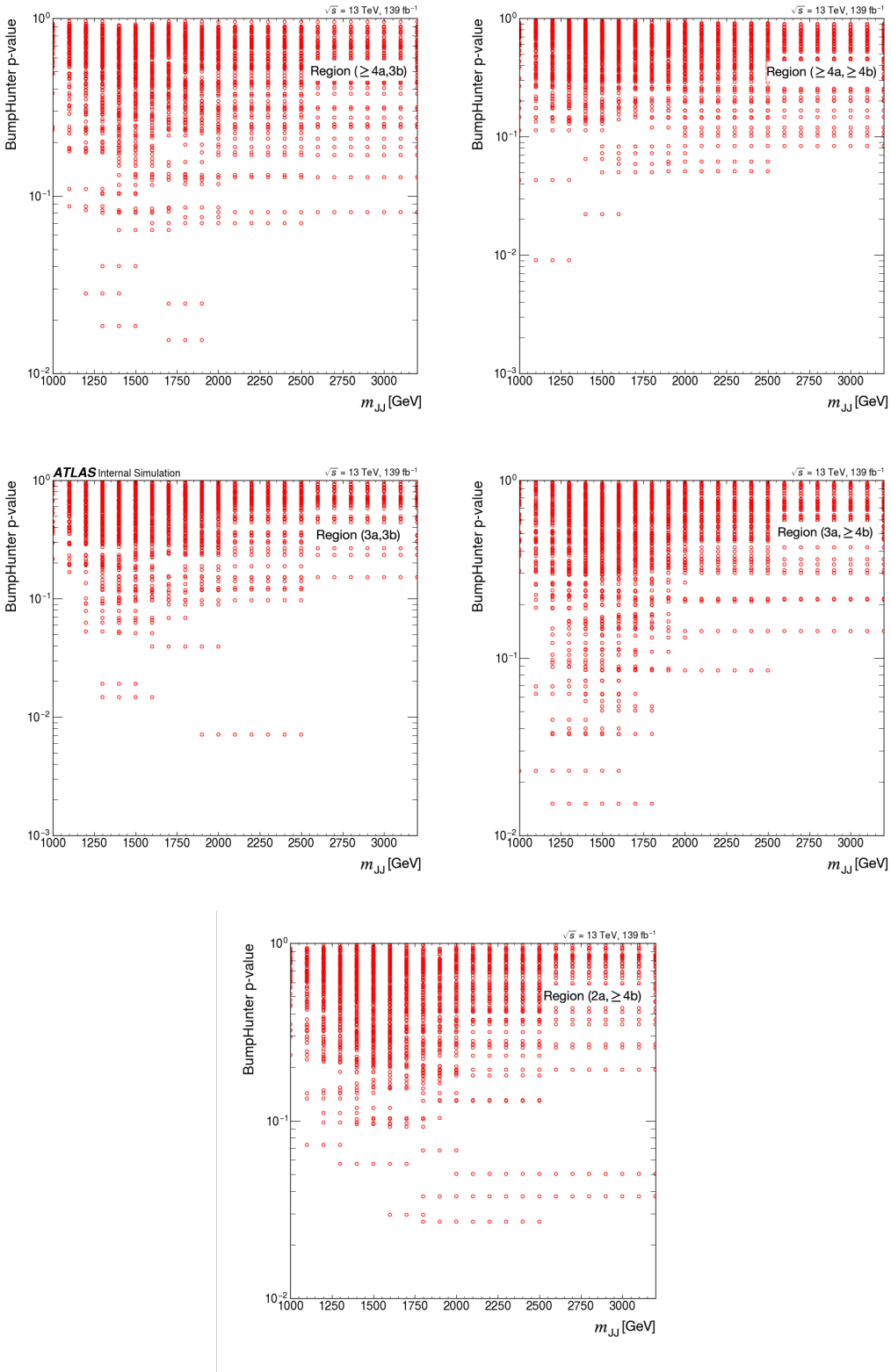

Figure 6.15: BumpHunter intervals versus p-values for 500 pseudo-data sets generated from background MC distributions.

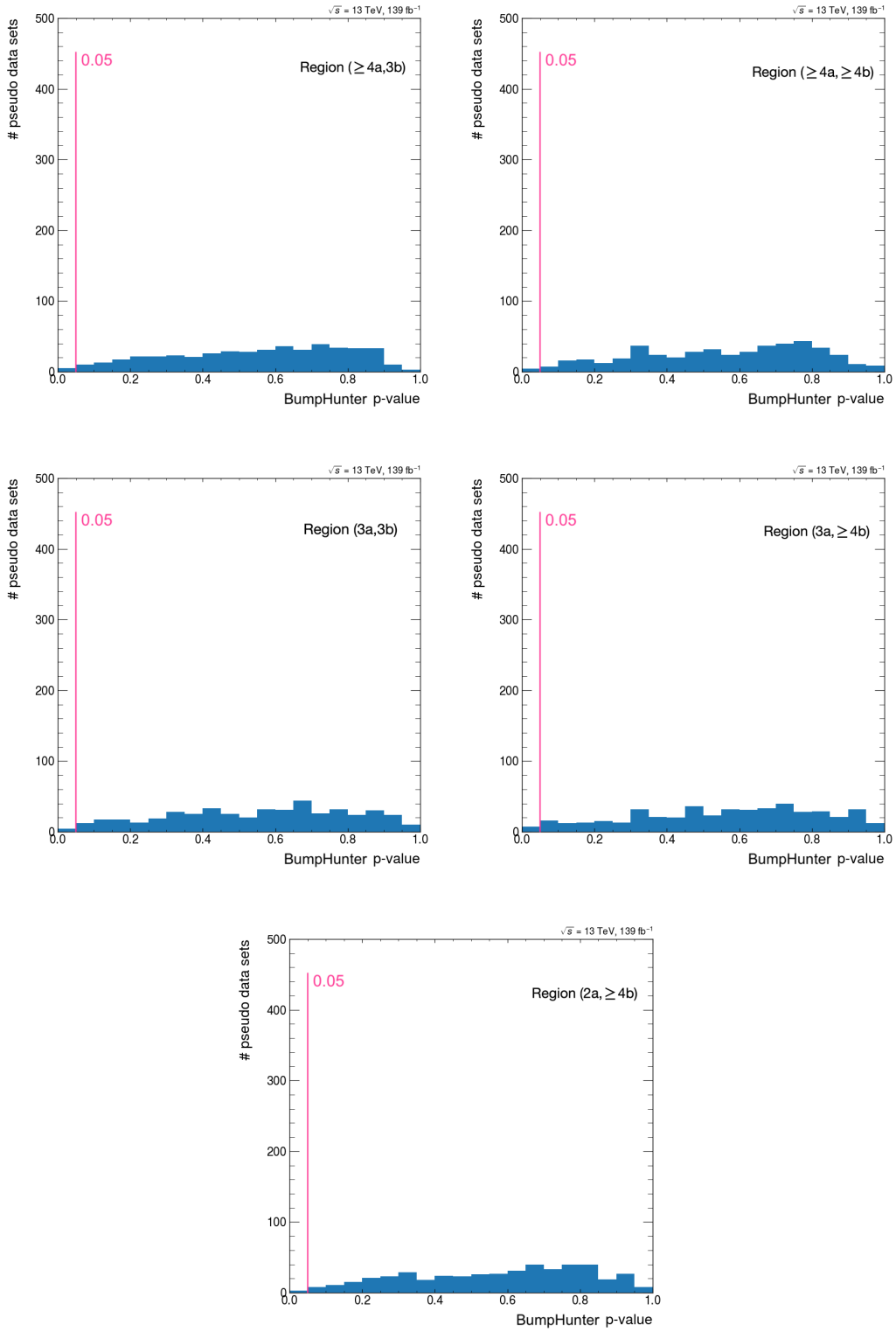

Figure 6.16: BumpHunter p-values for 500 pseudo-data sets generated from background MC distributions.

Bumphunter Results for Pseudodata With Signal Injected

Similarly to the previous test, also 500 sets of pseudodata sampled from MC distributions describing the background with a signal distribution added are scanned with the BumpHunter algorithm. The signal used for the study shown here is based on the $t\bar{t}Z'$ model with a resonance mass of 1.5 TeV and the cross section scaled to 100 fb which is of the order of magnitude of the expected analysis sensitivity. The large cross section is chosen to ensure that the algorithm is able to identify the signal. Because the background estimation to which the pseudodata is compared is obtained from after the profile likelihood fit assuming no signal in the fit, the background normalization is increased to accommodate for the signal in the pseudodata. Small signals can be absorbed completely by the fit and would not be identified by the BumpHunter algorithm. The BumpHunter results for an example pseudodata set is shown in Figure 6.17.

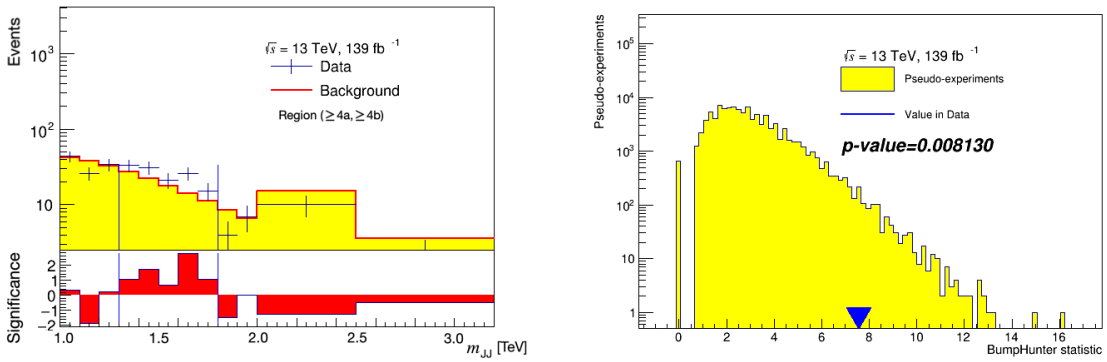

(a) m_{JJ} distribution with most discrepant interval highlighted.

(b) BumpHunter test statistic with the observed value and the corresponding p-value.

Figure 6.17: BumpHunter results for a pseudodata set generated from background and signal MC in the region $(\geq 4a, \geq 4b)$ showing (a) the most discrepant interval and (b) the BumpHunter test statistic.

In this test, the most discrepant intervals are expected to be centered around the resonance mass of 1.5 TeV. The p-values are expected to be small, especially for the regions with larger numbers of additional and b-tagged jets which are expected to contain larger relative amounts of signal. The most discrepant intervals versus the corresponding p-value are shown in Figure 6.18. The intervals are centered around the signal mass of 1.5 TeV for a majority of the pseudodata sets. The p-value corresponding to many of these intervals is small indicating a deviation of the data from the expected background distribution. The corresponding distribution of p-values is shown in Figure 6.19. An accumulation towards smaller p-values is seen for the regions $(\geq 4a, 3b)$ and $(\geq 4a, \geq 4b)$ as expected. Especially for the region $(\geq 4a, \geq 4b)$, a large majority of the pseudodata sets have a p-value smaller than 0.05. In contrast to the previous test, this test is of qualitative nature without providing a clearly-defined criterion for passing or failing it. The probability of the algorithm identifying the interval where the signal is expected strongly depends on the signal model, in particular its cross section and shape. However, a trend towards small p-values for intervals around the signal mass is observed, showing the ability of BumpHunter to identify these signals.

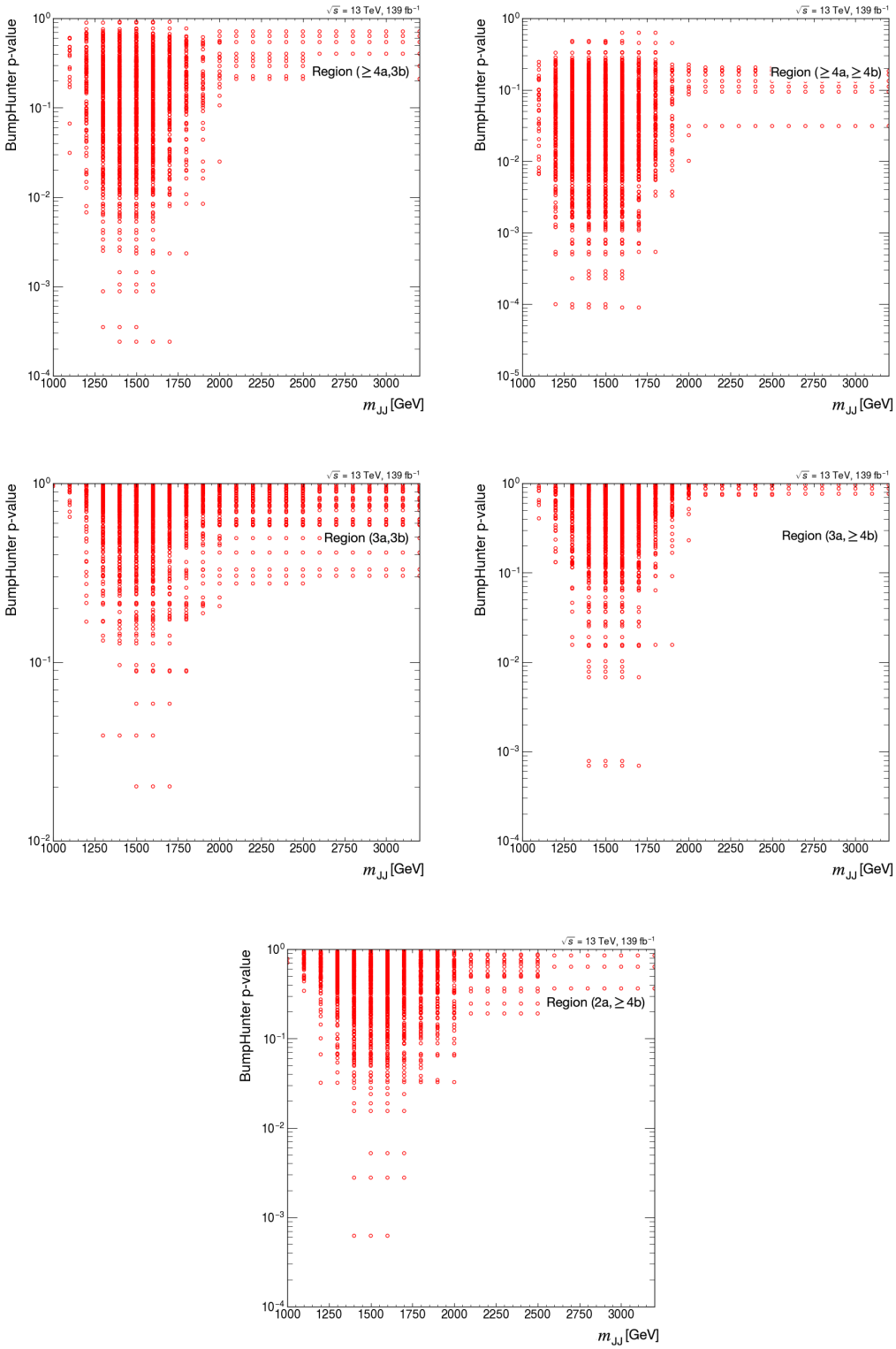

Figure 6.18: BumpHunter intervals versus p-values for 500 pseudodata sets generated from MC background distributions with the added contribution of a resonance signal with $m_{Z'} = 1.5$ TeV scaled to 100 fb.

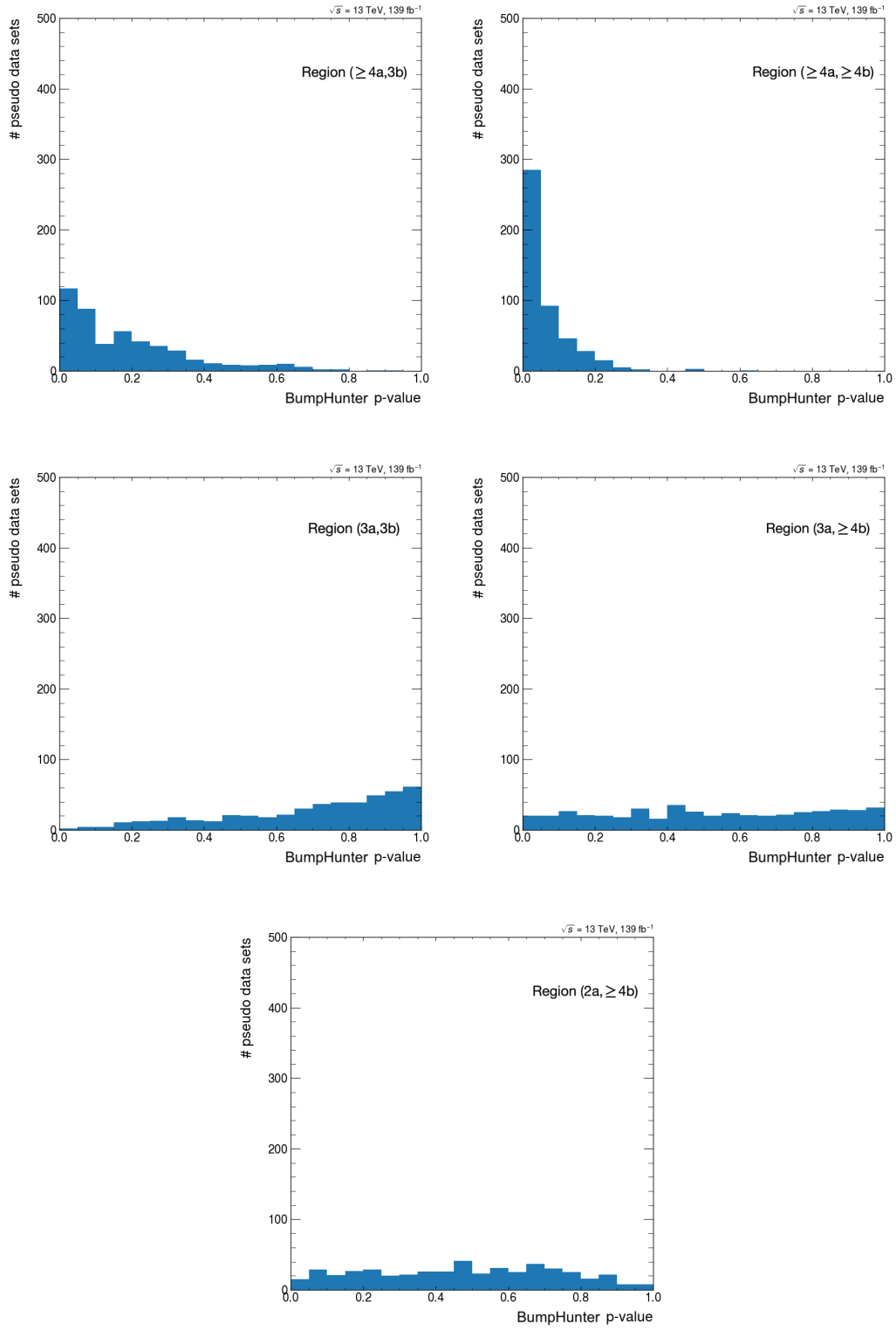

Figure 6.19: BumpHunter p-values for 500 pseudodata sets generated from MC background distributions with the added contribution of a resonance signal with $m_{Z'} = 1.5$ TeV scaled to 100 fb.

6.8.4 Model Dependent Tests

As opposed to the model-agnostic tests, for the model-dependent tests, the signal model as described in Section 2.3.3 is assumed in the following. In these tests, the ability of the statistical model to fit the specific signal is investigated.

Signal Extraction

The first model-dependent test studies the fit performance for different sizes of the signal. The nominal signal template corresponding to $\mu = 1$ is defined as the signal distribution of the 1.5 TeV signal normalized to an arbitrarily chosen cross section of 45 fb. For each signal factor, 500 pseudodata sets are generated from background MC with a signal scaled by different values of μ. The extracted signal strength is then obtained from the profile likelihood fit. Two examples for the distributions of the extracted signal strength for pseudodata sets that include signals with strengths of 0.5 and 1.5 respectively are shown in Figure 6.20.

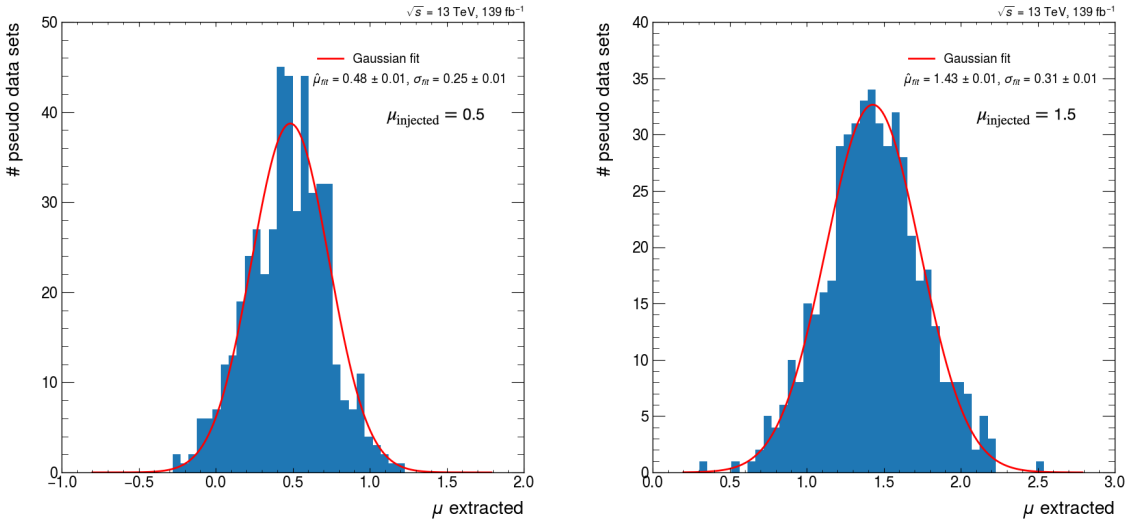

(a) Signal scaled by signal strength 0.5 included in pseudodata.

(b) Signal scaled by signal strength 1.5 included in pseudodata.

Figure 6.20: Distributions of the fitted value of the signal strength μ for 500 pseudodata sets generated from background MC distributions with added signal contributions of differenet signal strengths for $m_{Z'} = 1.5$ TeV). The distribution is fit with a Gaussian function shown in red with its mean and standard deviation printed.

The distributions are centered around the injected signal strengths as expected. The test is repeated for different values of the signal strength in the range between 0 and 3. The results are summarized in Figure 6.21 which shows the mean of the extracted signal strength as a function of the injected signal strength. The expected linear behavior is observed with only a small negative bias.

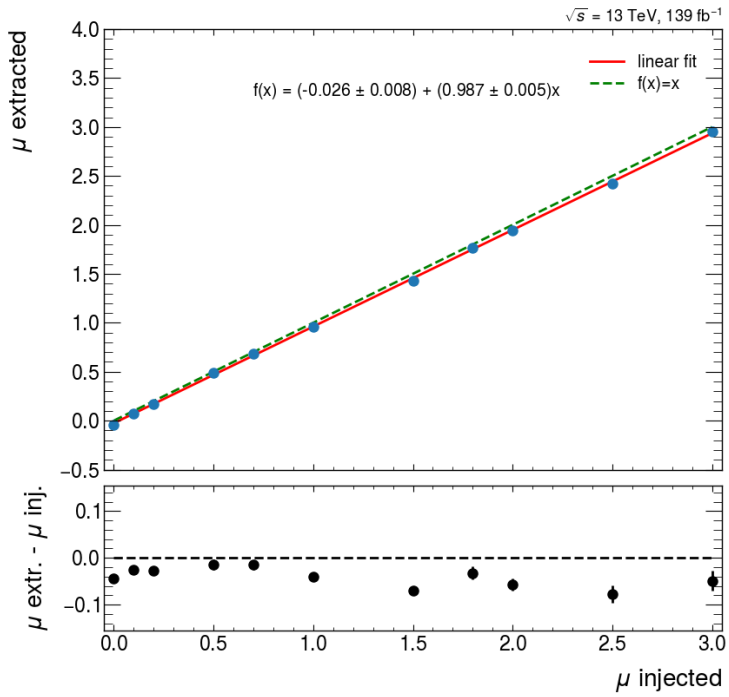

Figure 6.21: Mean of the extracted signal strength as a function of the injected signal strength for the $m_{Z'} = 1.5\,\text{TeV}$ signal.

Spurious Signal

Similar to the signal extraction test, in the spurious signal test the $t\bar{t}Z'$ signal model is fit to the pseudodata. In this case however, the pseudodata is generated from background-only MC. It is therefore expected that the fitted signal strength is compatible with 0. The test is repeated with the distribution of each of the six resonance masses used as signal templates. Two examples of the resulting distributions of the extracted signal strength μ with a Gaussian function fit to them are shown in Figure 6.22.

The best fit value S_{spur} of the spurious signal is determined by the mean of the Gaussian fit to the distribution of signal strengths as shown in the figures. The corresponding standard deviation of this Gaussian fit is σ_{fit}. The spurious signal uncertainty $|S_{\text{spur}}|$ should be in general small and smaller than σ_{fit}. Assuming a Gaussian measurement for the extracted signal, the total uncertainty on the signal yield can then be approximated with $\sigma_{\text{tot}} \approx \sqrt{\sigma_{\text{fit}}^2 + S_{\text{spur}}^2}$. A criterion can then be defined on the maximum relative size of this uncertainty $S_{\text{spur}}/\sigma_{\text{fit}}$. Criteria between 0.2 and 0.5 are typical choices. For each of the six resonance masses studied in this analysis, this ratio is computed and shown in Figure 6.23. The grey band indicates the ranges between 0.2 and 0.5 as well as between −0.2 and −0.5.

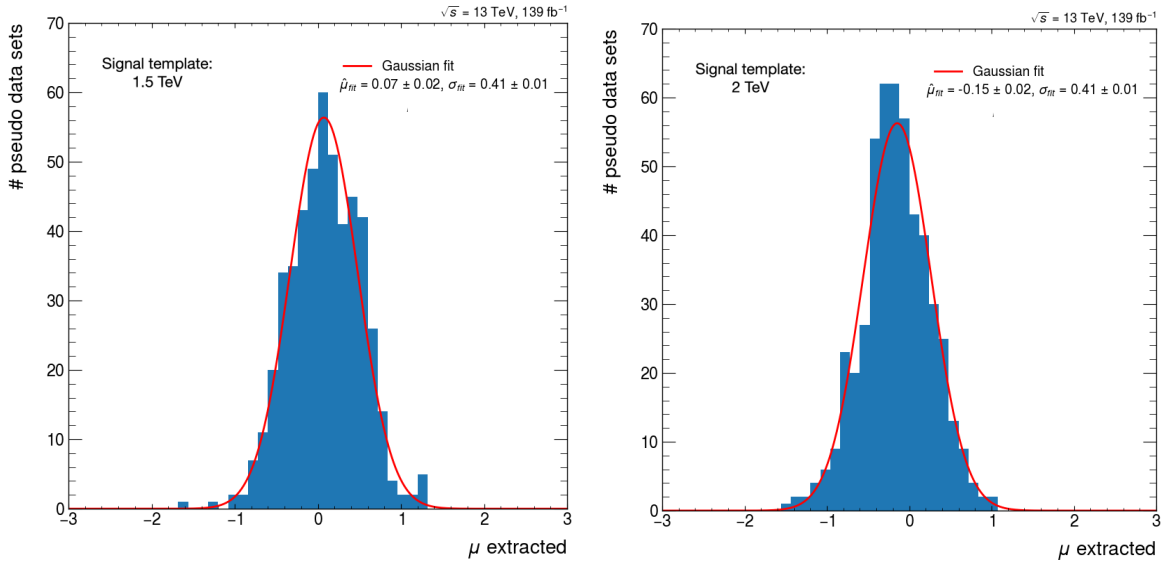

(a) Signal template with $m_{Z'} = 1.5$ TeV.

(b) Signal template with $m_{Z'} = 1.5$ TeV.

Figure 6.22: Fitted value of the signal strength μ for 500 pseudodata sets generated from background-only MC using different signal templates. The distribution is fit with a Gaussian function shown in red with its mean and standard deviation printed.

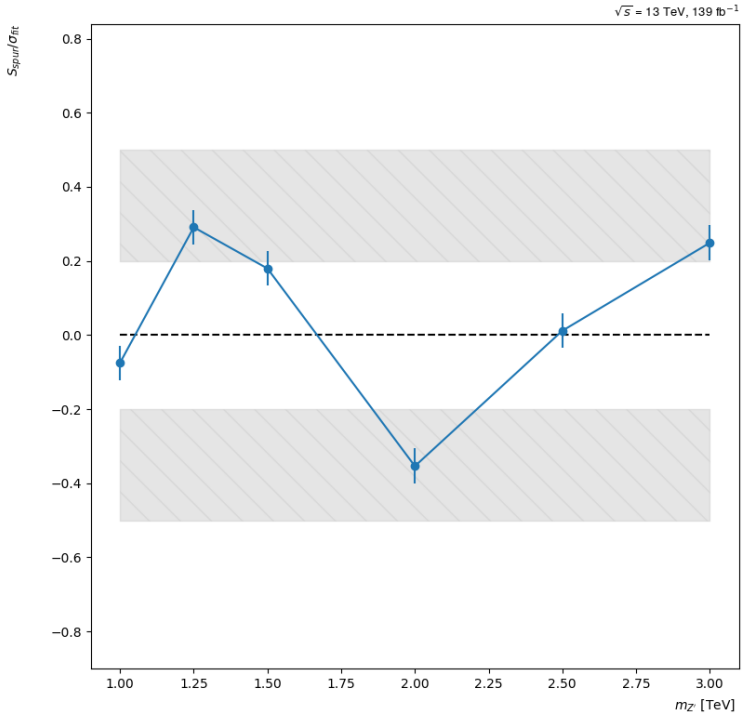

Figure 6.23: Ratio of mean μ obtained from Gaussian fits as shown in Figure 6.22 and standard deviation as a function of the resonance mass.

Multiple dedicated studies have been carried out to identify the origin of the observed spurious signal bias. The studies showed that the large spurious signal arises from a combination of different factors. One contributing factor is the procedure how the pseudodata is sampled. It is obtained from MC distributions while the background prediction is computed by extrapolating the dijet fit to source region pseudodata. As a consequence, the modeling that the functional form fit provides does not perfectly describe the MC. Another factor is the contribution of systematic uncertainty. When no systematic uncertainties but only statistical effects are taken into account, the spurious signal bias is reduced.

A designated uncertainty is defined to account for the spurious signal bias. For the definition of this uncertainty, Ref. [145] is followed closely. The absolute number of spurious signal events is obtained by multiplying the spurious signal strength from Figure 6.22 with the number of events of the corresponding signal template. The numbers of spurious signal events as a function of the resonance mass are shown in red Figure 6.24.

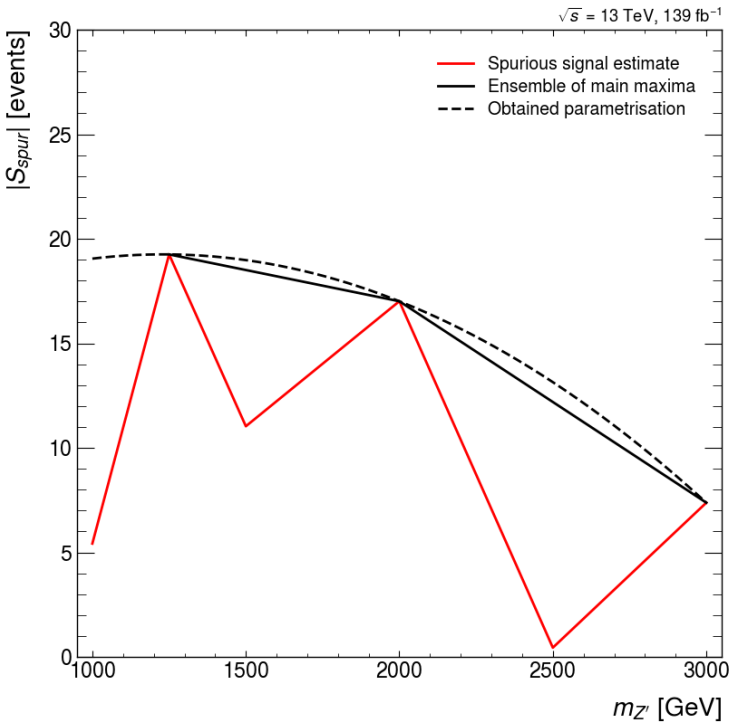

Figure 6.24: Number of spurious signal events as a function of the resonance mass shown in red. The main maxima of spurious signal events are shown in solid black with a polynomial of second order fit to them in black dashed.

In order to obtain a conservative estimate of the size of the spurious signal, the main maxima of the spurious signal events are selected. The main maxima of the spurious signal events shown in Figure 6.24 are at 1.25 TeV, 2 TeV and 3 TeV. These points are connected by the black solid line in the figure. The main maxima are then fit by a polynomial function of second order shown as the black dashed line. This function describes the envelope of spurious signal events which

gives a conservative estimate of the number of spurious signal events which is used to define the corresponding uncertainty. The signal template scaled to the envelope number of events of spurious signal is added to the nominal background prediction to obtain the distribution used as uncertainty. Depending on the signal template used in the profile likelihood fit, the uncertainty for the selected resonance mass is applied.

6.9 Results

The results of the statistical analysis are presented in this section. For the model independent interpretation, the data is compared with the expected background distribution and any deviations are statistically evaluated. For the model dependent interpretation, the simplified model for a heavy top-philic resonance presented in Section 2.3.3 ($t\bar{t}Z'$ model) is assumed and the 95 % CL upper limits on the cross section of this process are computed.

6.9.1 Impact and Correlation of Nuisance Parameters

The impacts of different groups of systematic uncertainties relative to the total uncertainty of the fitted signal strength in the profile likelihood fit are summarized in Table 6.3.

Table 6.3: Relative contributions to the total uncertainty of the fitted signal strength for the $t\bar{t}Z'$ model with a mass of 1.5 TeV and 3 TeV.

Uncertainty categories	Relative contribution to the total uncertainty [%]	
	1.5 TeV	3 TeV
$t\bar{t}$+jets modeling	68	50
Signal bias	45	25
Functional fit and extrapolation	34	33
Jet energy scale and resolution	29	18
Single-top-quark modeling	9.4	7.7
Flavor tagging	8.7	3.6
Minor backgrounds modeling	5.1	5.6
Other uncertainties	0.4	2.0
Luminosity	0.3	0.1
Total systematic uncertainty	92	74
Statistical uncertainty	39	67

The different individual systematic uncertainties are grouped in categories according to the effects they account for. The relative contributions are computed for the $t\bar{t}Z'$ model with a mass of 1.5 TeV and 3 TeV. The signal with a resonance mass of 3 TeV is chosen as example for a high mass signal with an even broader distribution than for a resonance mass of 1.5 TeV. The profile likelihood fit is repeated for each group with the corresponding uncertainties set to their best fit values. The uncertainty on the signal strength is then subtracted in quadrature from the uncertainty of the fit including all uncertainties which gives the absolute impact. The relative impact is calculated as the absolute impact divided by the total uncertainty from the profile likelihood fit including all systematic uncertainties. Due to correlations between uncertainties, the total systematic uncertainty is not equal to the quadrature sum of the different groups. The systematic uncertainties dominate for lower resonance mass signals and the statistical uncertainty dominate for higher resonance mass signals. The largest contribution comes from the modeling of the $t\bar{t}$+jets background processes. This is expected, as they are the main background processes. The most dominant uncertainties within that group are the MC generator uncertainties and the parton shower uncertainties as well as the cross section uncertainties of $t\bar{t}+\geq 1b$ and $t\bar{t}+\geq 1c$. The signal bias uncertainty also has a large impact. As it has the same shape as the signal, a strong correlation between the signal strength μ and this uncertainty is expected. The high impact of the jet energy scale and resolution arises from the large jet multiplicity in the final state.

The correlation of the different individual systematic uncertainties assuming the background-only hypothesis is shown in the correlation matrix in Figure 6.25. Only the largest correlations are shown with correlation factors larger than 20 %. A previous version of the statistical model was used here. The parton shower uncertainty is only split in components for the normalization and shape of the m_{JJ} distributions. The MC generator uncertainty is only split in components for the $3b$- and $\geq 4b$-jets regions. Furthermore, the signal bias uncertainty is not included as it is only relevant when a signal contribution is included in the profile likelihood fit. All other systematic uncertainties are included as described in Section 6.7. The largest correlations arise between systematic uncertainties associated with the modeling of the main background processes $t\bar{t}$+jets. A large correlation between the normalization component of the MC parton shower and the $t\bar{t}+\geq 1b$ cross section uncertainty is observed. This correlation is expected as the choice of parton shower modeling in MC simulations can affect the $t\bar{t}+\geq 1b$ and $t\bar{t}+\geq 1c$ components in $t\bar{t}$+jets samples. Another moderate correlation is observed between the two components for the $3b$- and $\geq 4b$-jets regions of the MC generator region uncertainty. This correlation arises because the two components of the same underlying systematic uncertainty are not fully independent of each other.

6.9.2 Model-Independent Interpretation

The BumpHunter algorithm [134] is used for the model-independent interpretation. As described in Section 6.6.2, the algorithm compares the given data and background distributions. For this analysis, the reconstructed invariant mass of the two RC jets m_{JJ} is studied. The background estimation in each region is the post-fit distribution after carrying out the conditional $\mu = 0$ profile likelihood fit where no signal presence is assumed. This approach allows to take into account effects of the systematic uncertainties. As a consequence, the background estimation can be adjusted by the

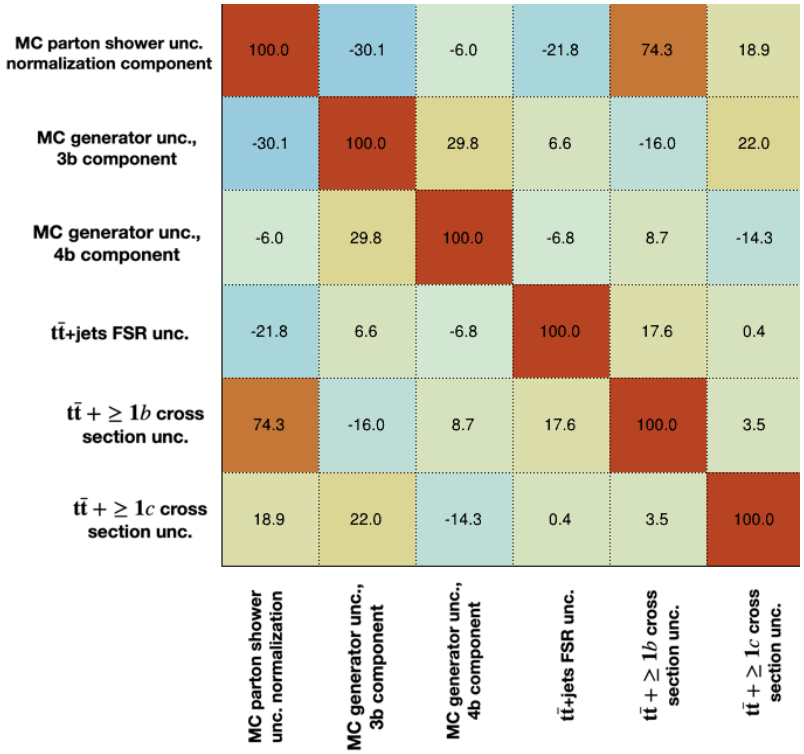

Figure 6.25: Estimated values of the correlations between the different nuisance parameters after the background-only fit to signal region data above a threshold of 20 %.

profile likelihood fit to partially absorb a potential signal present in the data. However, sufficiently large signals could still be observed with this method as demonstrated in Section 6.8.3. While in the profile likelihood fit the regions are combined, the model-independent interpretation is carried out separately for each region. Combining the regions in this part of the search requires that the algorithm can identify an excess in all regions at the same positions. Especially in the regions where less signal is expected it cannot always be identified. Furthermore, how the signal is distributed over the different regions depends on the considered model. The regions were therefore not combined here.

Figure 6.27 shows the comparison of the post-fit distribution of the background estimate and the data which enter the BumpHunter algorithm. Additionally, the post-fit background uncertainty and the data over background ratio are shown. A signal distribution for the $t\bar{t}Z$ model with $m_{Z'} = 1.5$ TeV is shown for visualization but is not included in this part of the interpretation. It is scaled to a cross section of 45 fb which corresponds to 100 times the theory prediction of the cross section assuming a coupling of the resonance to the top quark of $c_t = 1$. The intervals identified to have the largest deviation of the data compared to the background estimate are highlighted by vertical blue lines. The corresponding bin significance is shown in the lower panel. The per bin significances within the most discrepant interval are combined to yield the significance and p-value of that interval which is indicated for each region.

The data is modeled well by the background estimate. This is also reflected in the GoF p-value of 0.68 which is computed for all regions combined. No excess of the data over the expected background is observed in any region. Intervals with a corresponding p-value below a chosen threshold of 0.05 would be considered as significantly deviating from the background prediction. None such intervals are observed. The interval with the smallest p-value identified by the BumpHunter algorithm is observed in the region $(2a, \geq 4b)$ and corresponds to a significance of 0.64σ.

6.9.3 Model-Dependent Interpretation

In the second interpretation phase of the analysis, the $t\bar{t}Z'$ model is explicitly assumed. The compatibility of the data with the background estimate and an additionally present signal is studied. As no deviation from the data compared to the background estimation was observed, the upper limits on the cross section are computed.

Unconditional Profile Likelihood Fit

For computing the upper limits on the model under consideration, unconditional profile likelihood fits are performed for each resonance mass. In this case, the profile likelihood is carried out with the signal strength μ included as free parameter. In the following, a fit assuming the $t\bar{t}Z'$ signal model with $m_{Z'} = 1.5\,\text{TeV}$ and a cross section of $\sigma = 45\,\text{fb}$ is discussed as an example. The uncertainties described in Section 6.7 are included as well as the signal bias uncertainty as defined in Section 6.8.4. The m_{JJ} distributions of the data compared to the background estimate with the signal distribution overlayed is shown in Figure 6.28. Because of the broadness of the signal, no clear peak structure is observed. The signal is distributed over a wider range in m_{JJ} increasing the number of total events but a maximum can still be observed around the signal mass of 1.5 TeV. The signal contribution is larger in the regions with larger numbers of additional and b-tagged jets as expected. The best fit value obtained for the signal strength is $\mu = 0.06 \pm 0.28$ as shown in Figure 6.26.

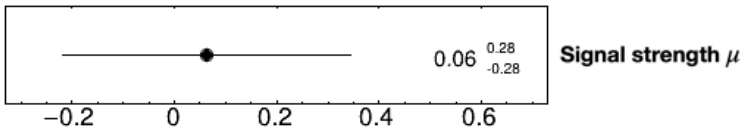

Figure 6.26: Extracted signal strength μ after unconditional signal plus background profile likelihood fit to signal regions for a signal with $m_{Z'} = 1.5\,\text{TeV}$ and $\sigma = 45\,\text{fb}$.

The corresponding significance is 0.23σ observed and 3.59σ expected. The data is therefore not significantly discrepant from the background. The m_{JJ} distributions of the data compared to the background estimate with the signal distribution after the profile likelihood fit is shown in Figure 6.29. The signal contribution almost entirely vanishes as the data is described well by the background estimate alone which is also reflected in the small value of μ. The evaluated goodness of fit p-value is 0.66 in this case which confirms that no deviation of the data compared to the expected background is observed.

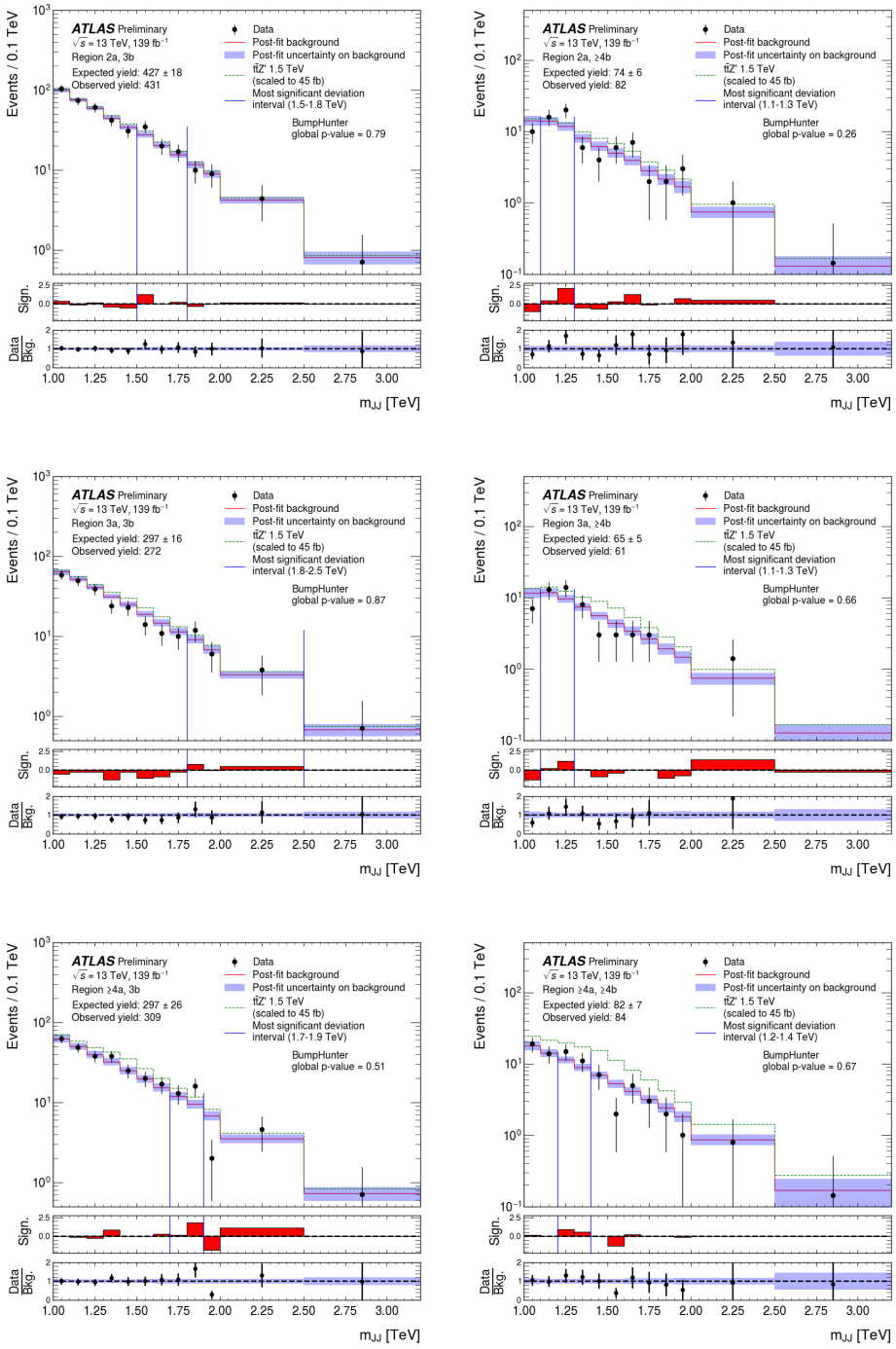

Figure 6.27: Comparison of the post-fit background distributions with uncertainties to data. The lowest panel shows the ratio data over background. An example for a signal is shown in green for $m_{Z'} = 1.5$ TeV scaled to 45 fb. The blue vertical lines indicate the most discrepant intervals as identified by the BumpHunter algorithm with the corresponding p-values indicated in the figure. The middle panel shows the BumpHunter significance per bin. Figure taken from Ref. [4].

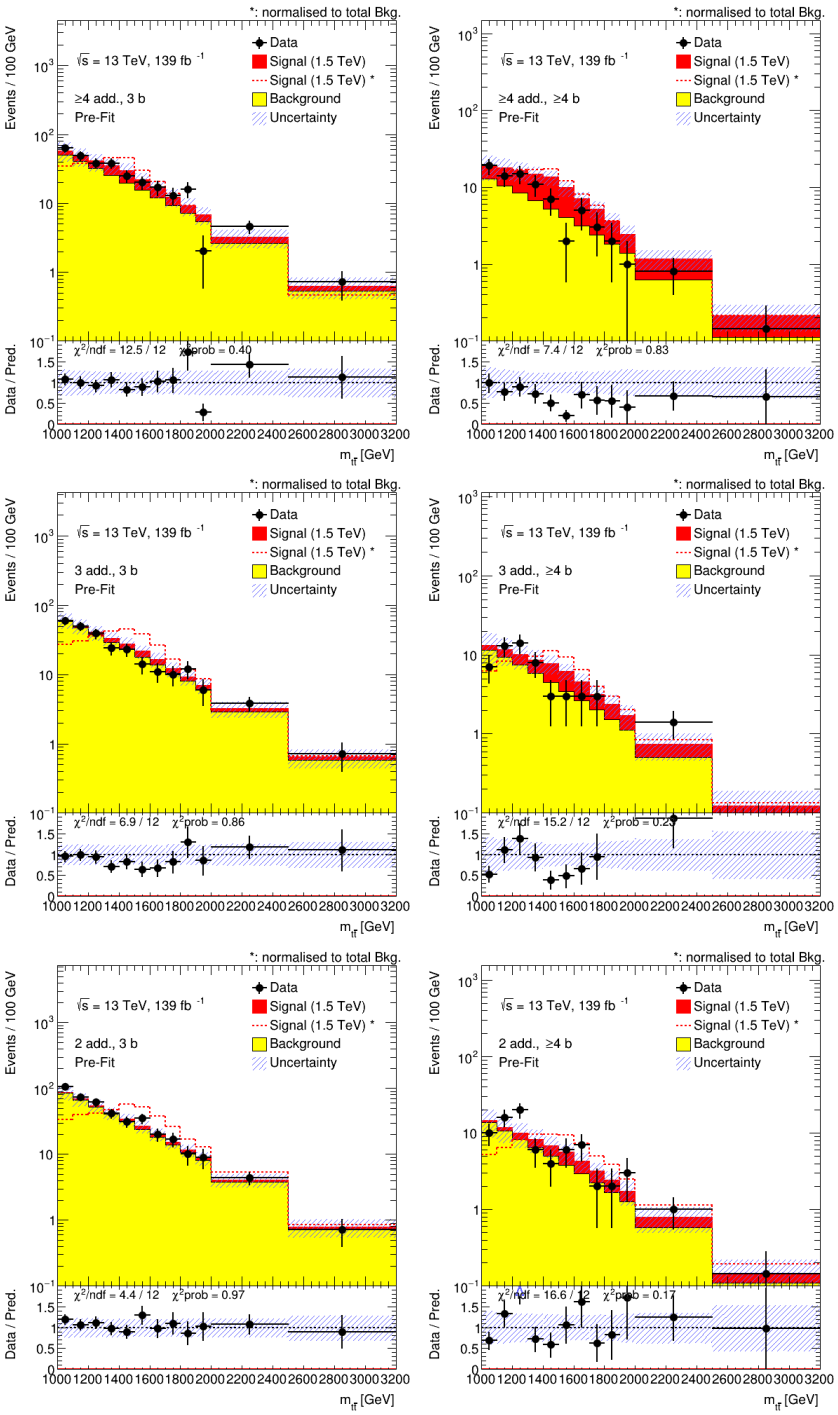

Figure 6.28: Comparison of the m_{JJ} distributions for observed data and signal + background prediction in all signal regions before the profile likelihood fit for a signal with $m_{Z'} = 1.5$ TeV and $\sigma = 45$ fb. The lower panel shows the ratio of the data over expected background. The error band includes all systematic uncertainties described in Section 6.7.

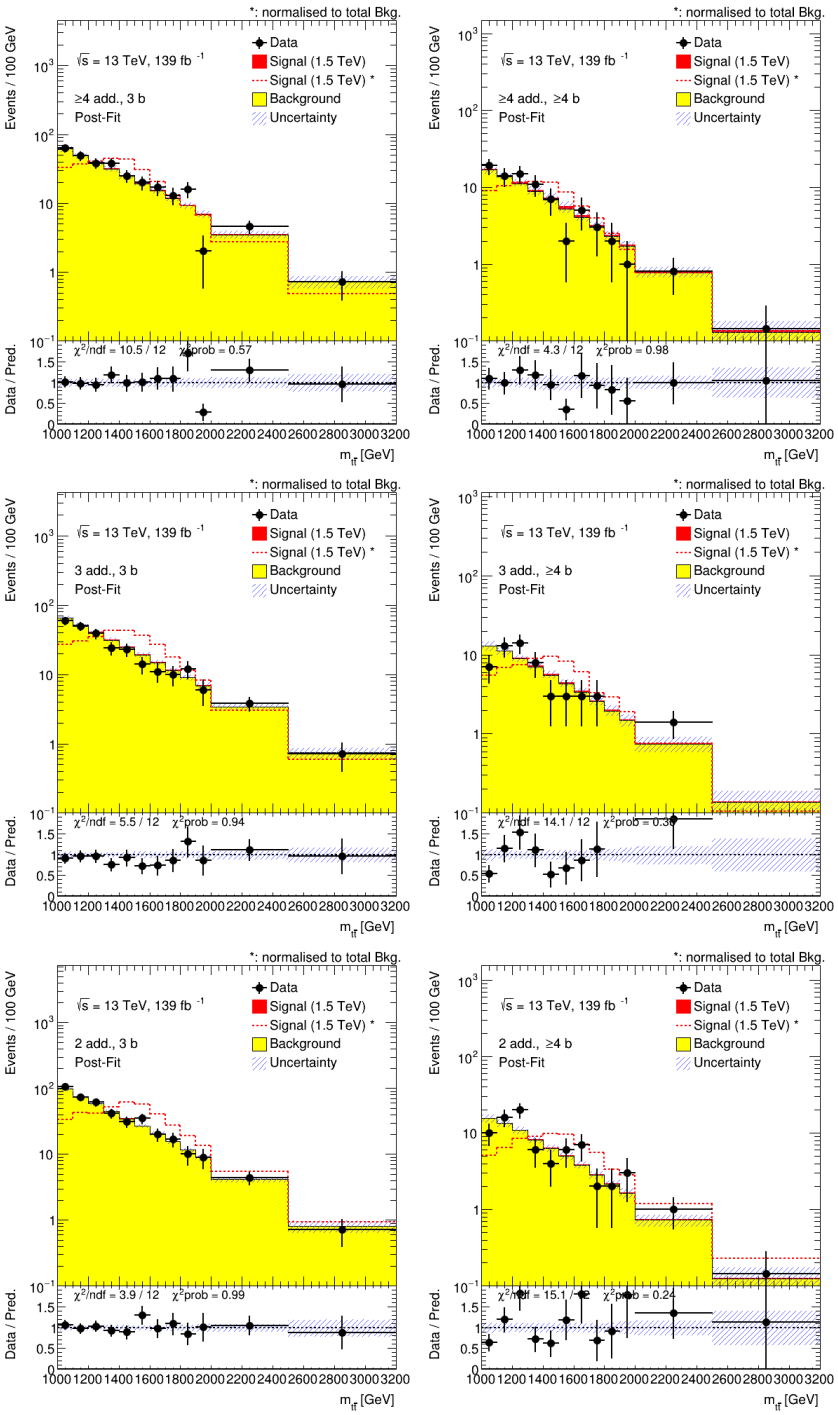

Figure 6.29: Comparison of the m_{JJ} distributions for observed data and signal + background prediction in all signal regions after the unconditional profile likelihood fit for a signal with $m_{Z'} = 1.5\,\text{TeV}$ and $\sigma = 45\,\text{fb}$. The lower panel shows the ratio of the data over expected background. The error band includes all systematic uncertainties described in Section 6.7.

Upper Limits for Constant c_t

The upper limits are evaluated in terms of the CL_s method as described in Section 6.6.3. The cross section upper limit is shown as a function of the resonance mass in Figure 6.30.

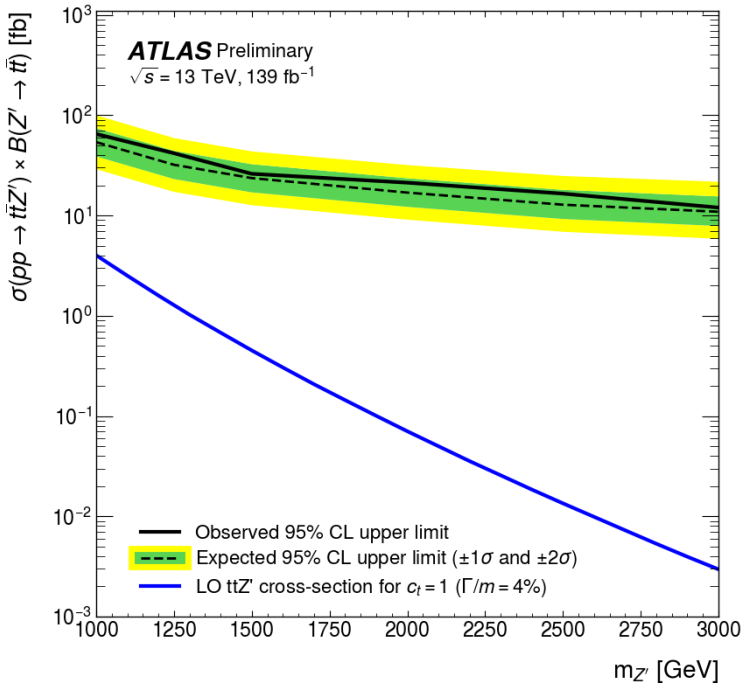

Figure 6.30: The 95 % CL upper limit on the cross section of the $t\bar{t}Z'$ signal as function of the resonance mass $m_{Z'}$. The green and yellow band correspond to the $\pm 1\sigma$ and $\pm 2\sigma$ bands, respectively. The theory cross section predicted by the model described in Section 2.3.3 for $c_t = 1$ is shown in blue.

In addition to the upper limits, the theoretical prediction is shown for the $t\bar{t}Z'$ signal model assuming a coupling between the top quark and the resonance of $c_t = 1$. The observed (expected) limits range between 59 (52) fb for $m_{Z'} = 1$ TeV and 11 (10) fb for $m_{Z'} = 3$ TeV. No exclusions for this signal model can be made for the case of $c_t = 1$.

Upper Limits as Function of c_t

In the following part of the model-dependent interpretation, a more inclusive signal model is assumed. These results will be presented in a publication which is about to be submitted to a peer-reviewed journal.

As discussed in Section 2.3.3, there are additional production modes of the signal which were so far neglected in the $t\bar{t}Z'$ model as it corresponds to a scenario where θ is chosen to minimize these contributions. The signal model considered below includes the t-channel production of the top-philic resonance as well as its production in association with tj or tW. Two values of the chirality

parameter θ are considered. For $\theta = 0$, the contribution of the production modes of the signal in association with tj or tW are maximized, while they are minimized for $\theta = \pi/2$. Furthermore, different values of the coupling of the resonance to the top quark c_t are studied. The c_t parameter strongly affects the signal cross section. The number of signal events increases with increasing c_t as shown in Figure 6.31 for $m_{Z'} = 1.5$ TeV in the region $(\geq 4a, \geq 4b)$. The shape information of the signal distribution is lost as for large values of c_t. For $c_t = 4$, the decay width according to Eq. 2.52 is approximately 64 %. For $c_t = 4.5$, the relative width is about 81 %. Approaching these large relative widths, the signal cannot further be described as a resonance.

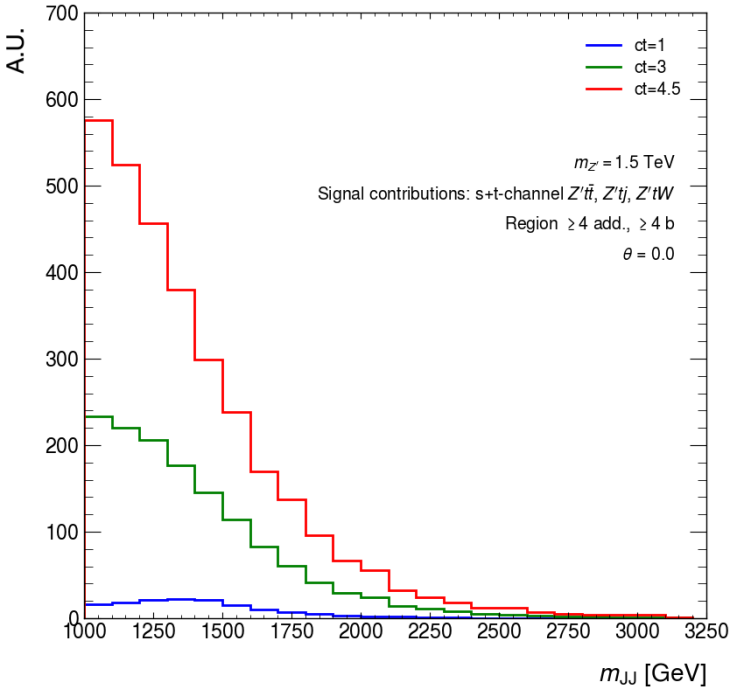

Figure 6.31: The $m_{t\bar{t}}$ distribution of the 1.5 TeV Z' resonance for different values of its coupling to the top quarks c_t in the region $(\geq 4a, \geq 4b)$.

A scan in c_t is carried out for values between 1.0 and 4.5. For each combination of c_t and $m_{Z'}$, the 95 % CL upper limit is computed. All systematic uncertainties described Section 6.7 are included. The signal bias uncertainty is evaluated for each point in the c_t and mass plane. The expected and observed upper limits on the signal strength μ are shown for $\theta = \pi/2$ in Figure 6.32 and for $\theta = 0$ in Figure 6.33. If the observed upper limit on the signal strength is smaller than 1 for a specific choice of the considered parameters, this point can be excluded. For $\theta = \pi/2$, two points can be excluded for the c_t values 4.0 and 4.5 for $m_{Z'} = 1$ TeV. For $\theta = 0$, three points of this grid of c_t and $m_{Z'}$ can be excluded based on their observed upper limit, the c_t values 4.0 and 4.5 for $m_{Z'} = 1$ TeV and for $c_t = 4.5$ and $m_{Z'} = 1.25$ TeV. The corresponding upper limits on the production cross section of the heavy top-philic resonance is shown in Figure 6.34 for $c_t = 1$ as in the first interpretation phase and for $c_t = 4$ which is the smallest c_t value resulting in an exclusion.

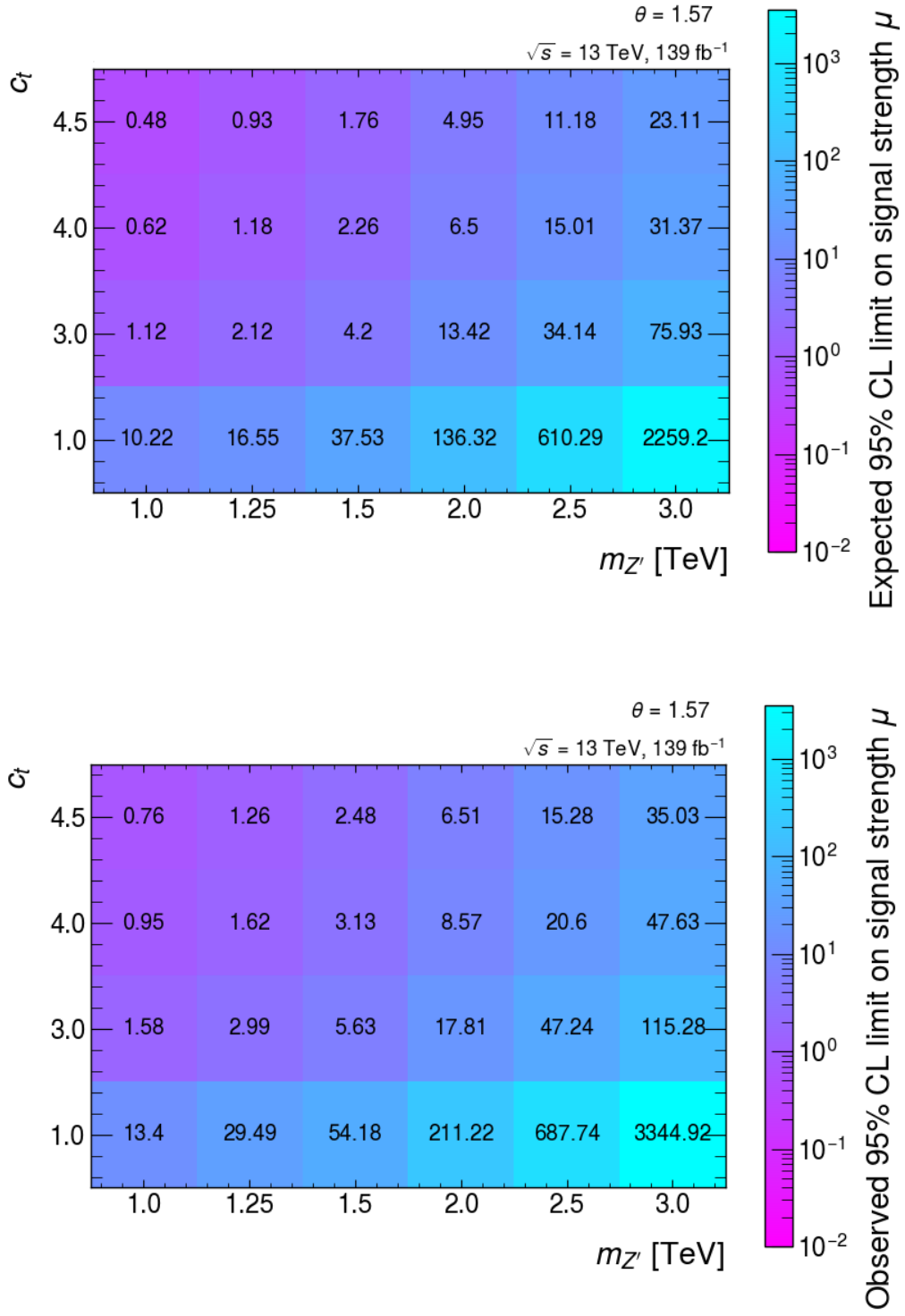

Figure 6.32: The expected and observed 95 % CL upper limit on the signal strength μ of the simplified model of a heavy top-philic resonance as function of its mass $m_{Z'}$ and its coupling to the top quarks c_t for $\theta = \pi/2$.

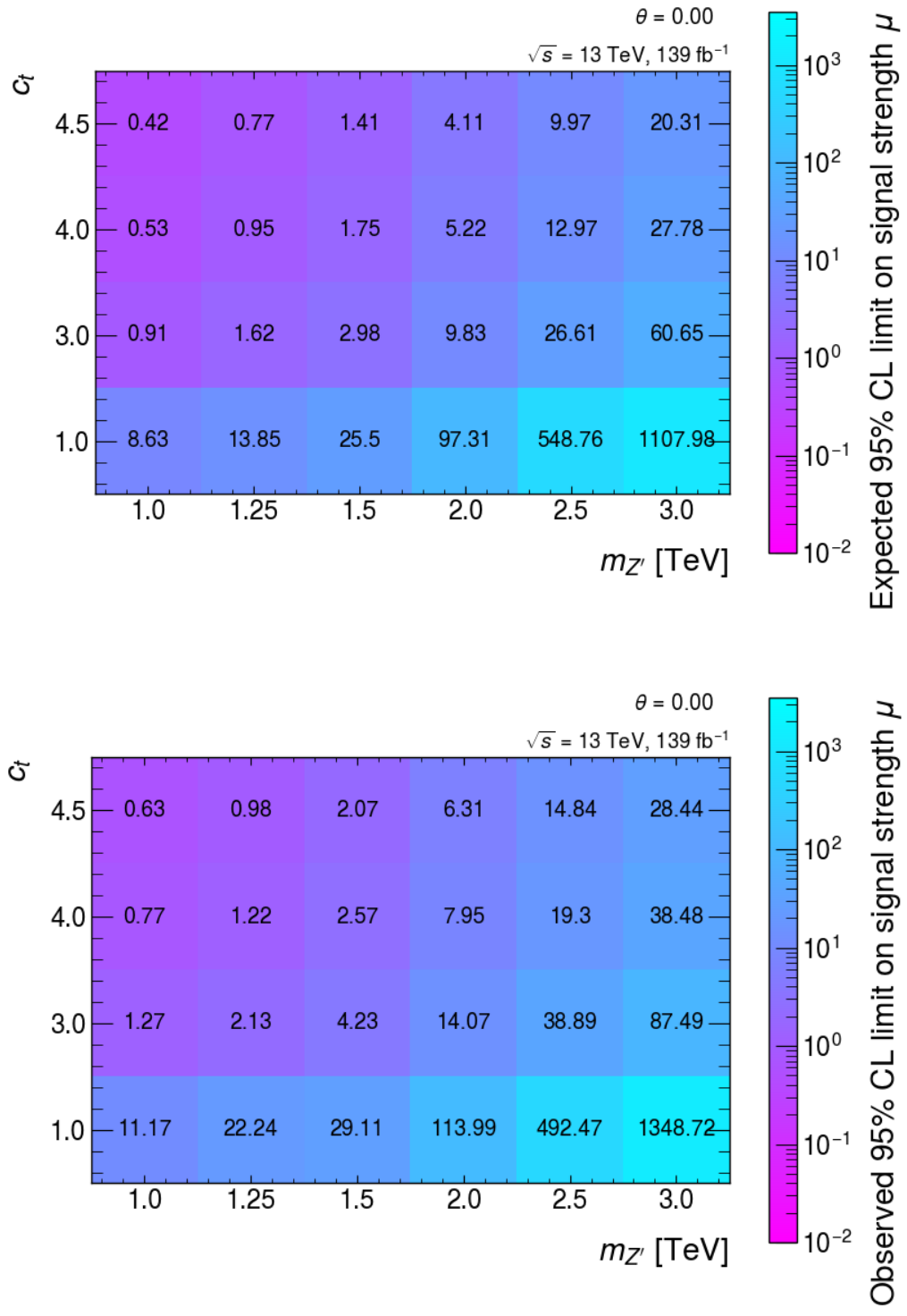

Figure 6.33: The expected and observed 95 % CL upper limit on the signal strength μ of the simplified model of a heavy top-philic resonance as function of its mass $m_{Z'}$ and its coupling to the top quarks c_t for $\theta = 0$.

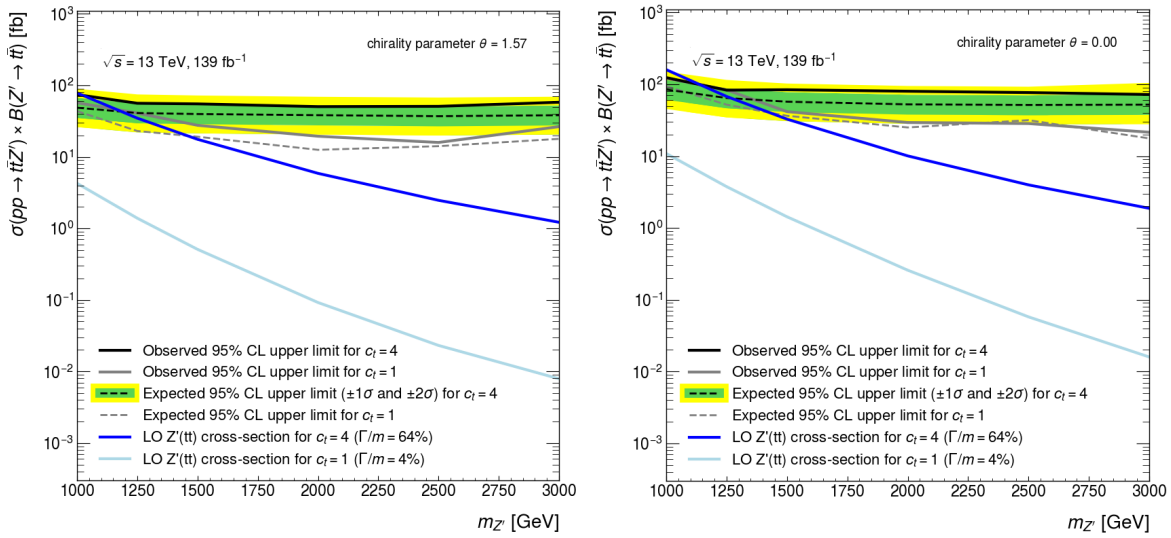

(a) $\theta = \pi/2$ (b) $\theta = 0$

Figure 6.34: The expected and observed 95 % CL upper limit on the cross section of the simplified model of a heavy top-philic resonance as function of its mass $m_{Z'}$ for $c_t = 4$ in black and $c_t = 1$ in grey for (a) $\theta = \pi/2$ or (b) $\theta = 0$. The theory cross section predicted by the considered model for $c_t = 4$ is shown in dark blue and for $c_t = 1$ in light blue.

6.10 Future Prospects of the Analysis

The search for heavy resonances with an explicit reconstruction of the resonance was carried out for the first time with Run 2 data. Future iterations of this analysis are foreseen and will aim to improve its results.

One limitation of the analysis selection as described, is the broad distribution of the reconstructed invariant mass of the top quark candidates. A narrower resonance peak could be identified more easily over the steeply falling background. One important factor leading to the broad signal shape is the incorrect identification of the top quarks originating from the resonance decay. These two top quarks would be highly boosted and carry large momentum. When the top quark pair used to reconstruct the resonance mass includes one of the spectator top quarks instead, the reconstructed mass is lower than with the correct choice of top quarks. This effect is shown in Figure 6.35 using simulated events for the $t\bar{t}Z'$ model with $m_{Z'} = 1.5$ TeV.

The lepton required in the selection is expected to originate from a leptonically decaying top quark in most cases. For a large fraction of events, the lepton is matched to a top quark which is used to reconstruct the resonance instead as shown in red. The reconstructed mass using only top quarks that are matched to a top quark from the resonance decay, shows a clearer peak structure closer to the mass of the resonance as shown in blue. The resulting distribution including both cases which corresponds to the signal template used in the presented analysis is shown in pink. In addition to the peak around the signal mass, it shows a broad shoulder from the events where the lepton originates

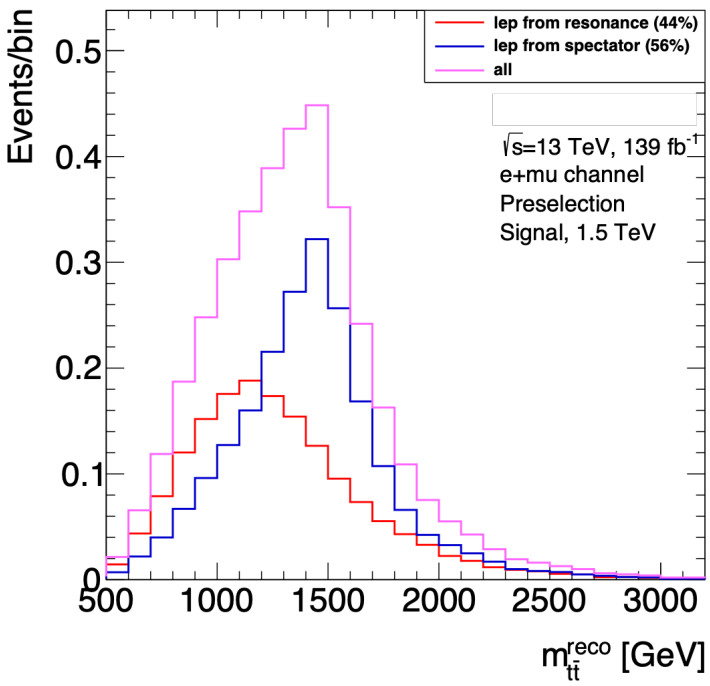

Figure 6.35: Reconstructed top pair mass $m_{t\bar{t}}$ with the lepton matched to a spectator top quark or a resonance top quark.

from a resonance top quark. Several attempts were made to mitigate the contribution of leptonically decaying top quarks in the reconstruction of the resonance. These studies include additional cuts on the RC jets and variables such as the distance of the lepton to the closest b-tagged jet and the p_{T} of that b-tagged jet. None of the studied variables allowed for an improved discrimination between the hadronically decaying resonance top quarks and the leptonically decaying resonance top quarks. The imperfection in the reconstruction of the resonance was therefore accepted in this analysis and left for improvement in future iterations.

In addition to improved analysis techniques, the search will also benefit from a larger data set that will become available in the high-luminosity phase of the LHC as described in Section 4.4. Additionally, the detector will be upgraded which includes the replacement of the ATLAS inner detector. As the BSM four-top-quark production is a rare process, stronger limits are expected when data with larger integrated luminosity is studied. An estimate for the limits with $3\,\mathrm{ab}^{-1}$ assuming $c_t = 1$ is shown in Figure 6.36.

The cross sections predicted from theory for $c_t = 1$ and $c_t = 3$ are shown as well. The considered signal model contains the production modes of the top-philic heavy resonance in association with a top quark pair in the s- and t-channel as well as the production in association with tj or tW. While the signal model with $c_t = 1$ is still not in sensitivity reach, the model with $c_t = 3$ could be tested for $\mathrm{m}_{Z'} < 2\,\mathrm{TeV}$. The expected limits range between 11 fb for $\mathrm{m}_{Z'} = 1\,\mathrm{TeV}$ and 3 fb for $\mathrm{m}_{Z'} = 3\,\mathrm{TeV}$. The upper limits are estimated by a simple scaling of the background estimates by the increase in

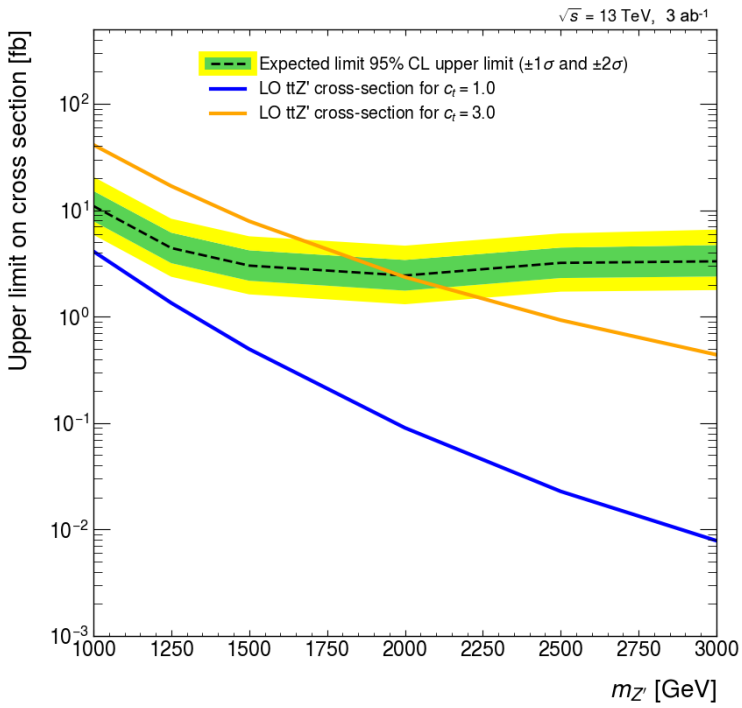

Figure 6.36: High luminosity estimate of the 95 % CL upper limit on the cross section of the top-philic heavy resonance model as function of the resonance mass $m_{Z'}$. An integrated luminosity of 3 ab^{-1} and $c_t = 1$ is assumed. The green and yellow band correspond to the $\pm 1\sigma$ and $\pm 2\sigma$ bands respectively. The theory cross section predicted by the model for $c_t = 1$ is shown in blue and for $c_t = 3$ in orange.

luminosity. This approximation neglects the major changes introduced by the detector upgrade and the HL-LHC running conditions which strongly effects the recorded data and the corresponding uncertainties. These effects are not taken into account here.

Based on these approximate estimates, lower limits than presented in this thesis are expected for the high-luminosity phase of the LHC and exclusions of the simplified top-philic resonance model would be possible at lower values of c_t.

CHAPTER 7

Conclusions

The development of the ITk endcap service trays and a search for heavy resonances in the four-top-quark final state are presented in this thesis. The service trays are part of the mechanical structure of the endcaps of the ITk detector which will replace the inner detector of ATLAS in the high-luminosity phase of the LHC. They contribute to the mechanical stability of the endcap, hold the cooling services of the petals and guide their electrical services. The fullfillment of the required specifications of the service trays with the developed design and methods is demonstrated in this thesis. An electrically conductive glued connection between the service trays, the wheels of the endcap structure and the cooling pipes is established to connect to the overall ITk Faraday cage. This is realized with copper pads cured to the surface of the service trays and a carbon fiber mat in addition to the adhesive. The applied method for this connection is optimized to achieve high mechanical strength. The required mechanical stiffness of the service tray is obtained by a C-profile design with additional flanges. The production of the final endcap service trays was completed in fall of 2021. The endcap global structure will be assembled in 2022. The fully equipped endcap is planned to be installed at the ATLAS detector in 2026. The upgraded detector will then allow to collect up to 3 ab^{-1} of data from 2029 onwards.

The data set of 139 fb^{-1} integrated luminosity collected in recent years already allows to investigate certain rare processes for the first time. A search for heavy resonances with a mass of 1 TeV or more in four-top-quark events is presented in this thesis. It investigates the full Run 2 data of proton-proton-collisions recorded in the years 2015-2018 with the ATLAS detector at a center-of-mass energy of $\sqrt{s} = 13$ TeV. This final state allows to search for resonances which are produced in association with a top quark pair and decay to another top quark pair. The semi-leptonic final state is investigated where one of the top quarks which does not originate from the resonance decays leptonically while the other three top quarks decay hadronically.

A potential new resonance with large coupling strength to the top quarks but negligible coupling strength to the lighter quarks could be observed in the studied final state. This analysis searches for heavy resonances with masses between 1 TeV and 3.2 TeV. Events with exactly one lepton are selected and categorized in regions according to the number of jets in the event. The potential signature of such a resonance is uniquely explored in this search by direct reconstruction of the

resonance. The expected contribution from SM particles is estimated with a data-driven approach to reduce known mismodeling effects in the simulation of the main background processes $t\bar{t}$+jets. The background is estimated by a functional form fit to data in the most signal depleted region. The resulting template is then extrapolated to the other regions with a scale factor function. The predicted SM contribution is compared to the recorded data in the model-independent interpretation of this search. No excess of the data compared to the background estimate is observed. For the model-dependent interpretation, a simplified model is assumed to describe the resonance. The 95 % CL upper limits are computed for six resonance masses on the cross section of the $t\bar{t}Z'$ production. A fixed coupling constant is assumed of the resonance coupling to the top quarks of $c_t = 1$. The observed (expected) limits range between 59 (52) fb for a resonance with $m_{Z'} = 1\,\text{TeV}$ and 11 (10) fb for a resonance with $m_{Z'} = 3\,\text{TeV}$. The results of this analysis are published in Ref. [4]. Upper limits in terms of different values of c_t are also presented assuming a more inclusive signal model. This signal model includes the t-channel production of the resonance as well as its production modes in association with tj and tW. The upcoming data-taking periods as well as the high luminosity phase of the LHC will offer the possibility to further investigate rare processes as the four-top-quark final state and improve the presented result.

With the large variety of potential signatures of new physics, the common effort of investigating the available data is continued and the reach for discoveries further extended by improving the tools. The work presented in this thesis aims to make a contribution to these endeavors.

Appendix

Appendix A

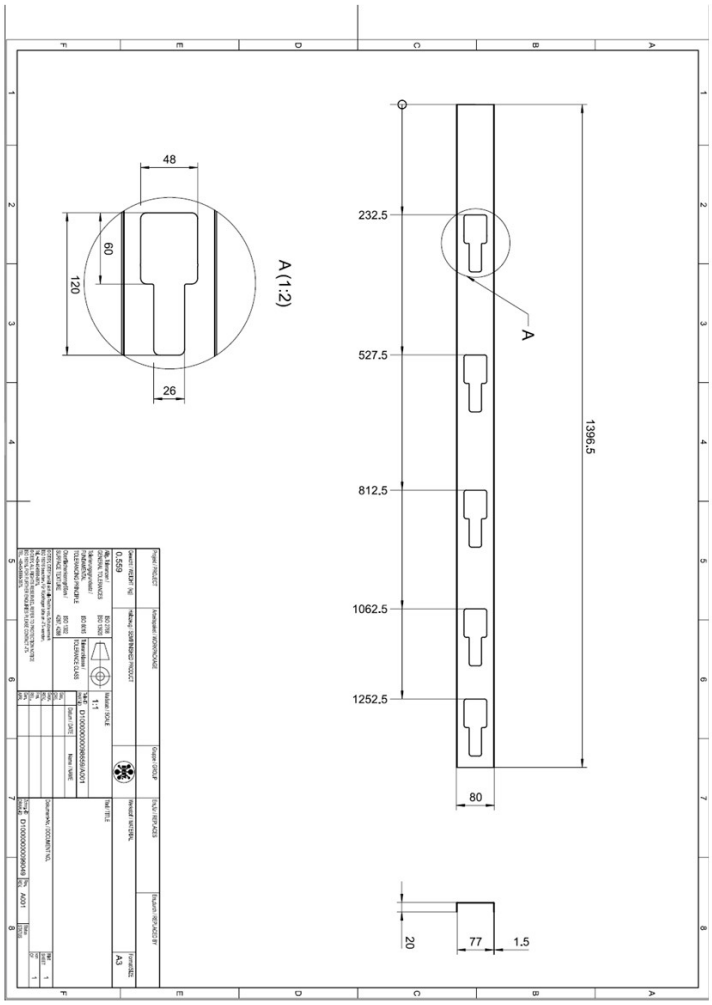

Figure A.1: Technical drawing of the service tray.

Bibliography

[1] ATLAS Collaboration, *Observation of a new particle in the search for the Standard Model Higgs boson with the ATLAS detector at the LHC*, Phys. Lett. B **716** (2012) 1, arXiv: 1207.7214 [hep-ex].

[2] CMS Collaboration, *Observation of a New Boson at a Mass of 125 GeV with the CMS Experiment at the LHC*, Phys. Lett. B **716** (2012) 30, arXiv: 1207.7235 [hep-ex].

[3] ATLAS Collaboration, *Evidence for $t\bar{t}t\bar{t}$ production in the multilepton final state in proton–proton collisions at $\sqrt{s}$ = 13 TeV with the ATLAS detector*, Eur. Phys. J. C **80** (2020) 1085, arXiv: 2007.14858 [hep-ex].

[4] ATLAS Collaboration, *Search for heavy resonances in four-top-quark final states in pp collisions at $\sqrt{s}$ = 13 TeV with the ATLAS detector*, ATLAS-CONF-2021-048 (2021), URL: http://cds.cern.ch/record/2781173.

[5] D. H. Perkins, *Introduction to high energy physics*, Cambridge: Cambridge Univ. Press, 2000.

[6] G. ALTARELLI, *The Standard model of particle physics*, CERN-PH-TH-2005-206 (2005), arXiv: hep-ph/0510281.

[7] A. Pich, "The Standard model of electroweak interactions," *2006 European School of High-Energy Physics*, 2007 1, arXiv: 0705.4264 [hep-ph].

[8] M. E. Peskin and D. V. Schroeder, *An Introduction to quantum field theory*, Reading, USA: Addison-Wesley, 1995, ISBN: 978-0-201-50397-5.

[9] E. Fermi, *On the Quantization of the Monoatomic Ideal Gas*, Translation of Italian original: Sulla quantizzazione del gas perfetto monoatomico (1926), arXiv: cond-mat/9912229.

[10] P. A. M. Dirac, *On the Theory of quantum mechanics*, Proc. Roy. Soc. Lond. A **112** (1926) 661.

[11] S. N. Bose, *Planck's law and light quantum hypothesis*, Z. Phys. **26** (1924) 178.

[12] N. Cabibbo, *Unitary Symmetry and Leptonic Decays*, Phys. Rev. Lett. **10** (1963) 531.

[13] M. Kobayashi and T. Maskawa, *CP Violation in the Renormalizable Theory of Weak Interaction*, Prog. Theor. Phys. **49** (1973) 652.

[14] *SM Infographic*,
URL: https://texample.net/tikz/examples/model-physics/
(visited on 02/07/2022).

[15] M. Gell-Mann, *The Eightfold Way: A Theory of strong interaction symmetry*,
CTSL-20, TID-12608 (1961).

[16] J. Ellis, *TikZ-Feynman: Feynman diagrams with TikZ*,
Comput. Phys. Commun. **210** (2017) 103, arXiv: 1601.05437 [hep-ph].

[17] S. L. Glashow, *Partial Symmetries of Weak Interactions*, Nucl. Phys. **22** (1961) 579.

[18] S. Weinberg, *A Model of Leptons*, Phys. Rev. Lett. **19** (1967) 1264.

[19] A. Salam, *Weak and Electromagnetic Interactions*, Conf. Proc. C **680519** (1968) 367.

[20] P. W. Higgs, *Broken Symmetries and the Masses of Gauge Bosons*,
Phys. Rev. Lett. **13** (1964) 508.

[21] F. Englert and R. Brout, *Broken Symmetry and the Mass of Gauge Vector Mesons*,
Phys. Rev. Lett. **13** (1964) 321.

[22] G. S. Guralnik, C. R. Hagen, and T. W. B. Kibble,
Global Conservation Laws and Massless Particles,
Phys. Rev. Lett. **13** (1964) 585, ed. by J. C. Taylor.

[23] P. W. Anderson, *Plasmons, Gauge Invariance, and Mass*,
Phys. Rev. **130** (1963) 439, ed. by J. C. Taylor.

[24] G. 't Hooft and M. J. G. Veltman, *Regularization and Renormalization of Gauge Fields*,
Nucl. Phys. **B44** (1972) 189.

[25] J. Goldstone, A. Salam, and S. Weinberg, *Broken Symmetries*, Phys. Rev. **127** (1962) 965.

[26] S. Abachi et al., *Observation of the top quark*, Phys. Rev. Lett. **74** (1995) 2632,
arXiv: hep-ex/9503003.

[27] J. H. Christenson, J. W. Cronin, V. L. Fitch, and R. Turlay,
Evidence for the 2π Decay of the K_2^0 Meson, Phys. Rev. Lett. **13** (4 1964) 138,
URL: https://link.aps.org/doi/10.1103/PhysRevLett.13.138.

[28] B. T. Cleveland et al.,
Measurement of the solar electron neutrino flux with the Homestake chlorine detector,
Astrophys. J. **496** (1998) 505.

[29] Z. Maki, M. Nakagawa, and S. Sakata,
Remarks on the unified model of elementary particles, Prog. Theor. Phys. **28** (1962) 870.

[30] B. Pontecorvo,
Neutrino Experiments and the Problem of Conservation of Leptonic Charge,
Sov. Phys. JETP **26** (1968) 984.

[31] Y. Fukuda et al., *Evidence for oscillation of atmospheric neutrinos*, Phys. Rev. Lett. **81** (1998) 1562, arXiv: hep-ex/9807003 [hep-ex].

[32] Q. R. Ahmad et al., *Direct evidence for neutrino flavor transformation from neutral current interactions in the Sudbury Neutrino Observatory*, Phys. Rev. Lett. **89** (2002) 011301, arXiv: nucl-ex/0204008 [nucl-ex].

[33] P. A. Zyla et al., *Review of Particle Physics*, PTEP **2020** (2020) 083C01.

[34] C. Bambi and A. D. Dolgov, *Introduction to Particle Cosmology*, Springer, 2015, ISBN: 9783662480779.

[35] F. Zwicky, *On the Masses of Nebulae and of Clusters of Nebulae*, Astrophys. J. **86** (1937) 217.

[36] V. C. Rubin and W. K. Ford Jr., *Rotation of the Andromeda Nebula from a Spectroscopic Survey of Emission Regions*, Astrophys. J. **159** (1970) 379.

[37] P. A. R. Ade et al., *Planck 2015 results. XIII. Cosmological parameters*, Astron. Astrophys. **594** (2016) A13, arXiv: 1502.01589 [astro-ph.CO].

[38] CMS Collaboration, *Search for production of four top quarks in final states with same-sign or multiple leptons in proton-proton collisions at $\sqrt{s}$ = 13 TeV*, Eur. Phys. J. C **80** (2020) 75, arXiv: 1908.06463 [hep-ex].

[39] R. Kukla, *Probing composite models at the LHC with exotic quarks production*, EPJ Web Conf. **138** (2017) 01009, ed. by S. Bondarenko, V. Burov, and A. Malakhov.

[40] G. Panico and A. Wulzer, *The Composite Nambu-Goldstone Higgs*, vol. 913, Springer, 2016, arXiv: 1506.01961 [hep-ph].

[41] N. Craig, F. D'Eramo, P. Draper, S. Thomas, and H. Zhang, *The Hunt for the Rest of the Higgs Bosons*, JHEP **06** (2015) 137, arXiv: 1504.04630 [hep-ph].

[42] J. Bernon, J. F. Gunion, H. E. Haber, Y. Jiang, and S. Kraml, *Scrutinizing the alignment limit in two-Higgs-doublet models: m_h=125 GeV*, Phys. Rev. D **92** (2015) 075004, arXiv: 1507.00933 [hep-ph].

[43] J. F. Gunion and H. E. Haber, *The CP conserving two Higgs doublet model: The Approach to the decoupling limit*, Phys. Rev. D **67** (2003) 075019, arXiv: hep-ph/0207010.

[44] N. Greiner, K. Kong, J.-C. Park, S. C. Park, and J.-C. Winter, *Model-independent production of a top-philic resonance at the LHC*, Journal of High Energy Physics **2015** (2015), URL: http://dx.doi.org/10.1007/JHEP04(2015)029.

[45] J. H. Kim, K. Kong, S. J. Lee, and G. Mohlabeng, *Probing TeV scale Top-Philic Resonances with Boosted Top-Tagging at the High Luminosity LHC*, Phys. Rev. D **94** (2016) 035023, arXiv: 1604.07421 [hep-ph].

[46] D. Kar, *Experimental Particle Physics*, 2053-2563, IOP Publishing, 2019, ISBN: 978-0-7503-2112-9, URL: https://dx.doi.org/10.1088/2053-2563/ab1be6.

[47] S. Mandelstam, *Determination of the pion - nucleon scattering amplitude from dispersion relations and unitarity. General theory*, Phys. Rev. **112** (1958) 1344.

[48] R. P. Feynman, *Photon-hadron interactions*, Frontiers in physics, Reading, MA: Benjamin, 1972, URL: https://cds.cern.ch/record/102074.

[49] Y. L. Dokshitzer, *Calculation of the Structure Functions for Deep Inelastic Scattering and e+ e- Annihilation by Perturbation Theory in Quantum Chromodynamics.*, Sov. Phys. JETP **46** (1977) 641.

[50] V. N. Gribov and L. N. Lipatov, *Deep inelastic e p scattering in perturbation theory*, Sov. J. Nucl. Phys. **15** (1972) 438, URL: https://cds.cern.ch/record/427157.

[51] G. Altarelli and G. Parisi, *Asymptotic Freedom in Parton Language*, Nucl. Phys. B **126** (1977) 298.

[52] J. C. Collins, D. E. Soper, and G. F. Sterman, *Factorization of Hard Processes in QCD*, Adv. Ser. Direct. High Energy Phys. **5** (1989) 1, arXiv: hep-ph/0409313.

[53] W. Herr and B. Muratori, *Concept of luminosity*, CERN Accelerator School (2006), URL: https://cds.cern.ch/record/941318.

[54] T. Gleisberg et al., *Event generation with SHERPA 1.1*, JHEP **02** (2009) 007, arXiv: 0811.4622 [hep-ph].

[55] T. Sjöstrand et al., *An introduction to PYTHIA 8.2*, Comput. Phys. Commun. **191** (2015) 159, arXiv: 1410.3012 [hep-ph].

[56] ATLAS Collaboration, *Summary of ATLAS Pythia 8 tunes*, tech. rep., CERN, 2012, URL: https://cds.cern.ch/record/1474107.

[57] J. Bellm et al., *Herwig 7.0/Herwig++ 3.0 release note*, Eur. Phys. J. C **76** (2016) 196, arXiv: 1512.01178 [hep-ph].

[58] E. Bothmann et al., *Event Generation with Sherpa 2.2*, SciPost Phys. **7** (2019) 034, arXiv: 1905.09127 [hep-ph].

[59] J. Alwall et al., *The automated computation of tree-level and next-to-leading order differential cross sections, and their matching to parton shower simulations*, JHEP **07** (2014) 079, arXiv: 1405.0301 [hep-ph].

[60] S. Alioli, P. Nason, C. Oleari, and E. Re, *A general framework for implementing NLO calculations in shower Monte Carlo programs: the POWHEG BOX*, JHEP **06** (2010) 043, arXiv: 1002.2581 [hep-ph].

[61] S. Agostinelli et al., *GEANT4–a simulation toolkit*, Nucl. Instrum. Meth. A **506** (2003) 250.

[62] M. Beckingham et al., *The simulation principle and performance of the ATLAS fast calorimeter simulation FastCaloSim*, ATL-PHYS-PUB-2010-013 (2010), URL: https://cds.cern.ch/record/1300517.

[63] J. de Favereau et al., *DELPHES 3, A modular framework for fast simulation of a generic collider experiment*, JHEP **02** (2014) 057, arXiv: 1307.6346 [hep-ex].

[64] *LHC Machine*, JINST **3** (2008) S08001, ed. by L. Evans and P. Bryant.

[65] *LEP design report*, Geneva: CERN, 1984, URL: https://cds.cern.ch/record/102083.

[66] *ATLAS: technical proposal for a general-purpose pp experiment at the Large Hadron Collider at CERN*, LHC technical proposal, Geneva: CERN, 1994, URL: https://cds.cern.ch/record/290968.

[67] *CMS, the Compact Muon Solenoid: Technical proposal*, LHC technical proposal, Geneva: CERN, 1994, URL: https://cds.cern.ch/record/290969.

[68] *ALICE: Technical proposal for a Large Ion collider Experiment at the CERN LHC*, LHC technical proposal, Geneva: CERN, 1995, URL: https://cds.cern.ch/record/293391.

[69] *LHCb : Technical Proposal*, Geneva: CERN, 1998, URL: https://cds.cern.ch/record/622031.

[70] E. Mobs, *The CERN accelerator complex - 2019. Complexe des accélérateurs du CERN - 2019*, (2019), General Photo, URL: https://cds.cern.ch/record/2684277.

[71] S. Fartoukh et al., *LHC Configuration and Operational Scenario for Run 3*, CERN-ACC-2021-0007 (2021), URL: https://cds.cern.ch/record/2790409.

[72] I. Zurbano Fernandez et al., *High-Luminosity Large Hadron Collider (HL-LHC): Technical design report*, **10/2020** (2020), ed. by I. Béjar Alonso et al.

[73] ATLAS Collaboration, *The ATLAS Experiment at the CERN Large Hadron Collider*, JINST **3** (2008) S08003.

[74] A. Vogel, *ATLAS Transition Radiation Tracker (TRT): Straw tube gaseous detectors at high rates*, Nucl. Instrum. Meth. A **732** (2013) 277, ed. by T. Bergauer et al.

[75] ATLAS Collaboration, *Operation of the ATLAS trigger system in Run 2*, JINST **15** (2020) P10004, arXiv: 2007.12539 [physics.ins-det].

[76] ATLAS Collaboration, *Performance of the ATLAS Inner Detector Track and Vertex Reconstruction in the High Pile-Up LHC Environment*, ATLAS-CONF-2012-042 (2012), URL: https://cds.cern.ch/record/1435196.

[77] R. Fruhwirth, *Application of Kalman filtering to track and vertex fitting*, Nucl. Instrum. Meth. A **262** (1987) 444.

[78] ATLAS Collaboration, *Topological cell clustering in the ATLAS calorimeters and its performance in LHC Run 1*, Eur. Phys. J. C **77** (2017) 490, arXiv: 1603.02934 [hep-ex].

[79] ATLAS Collaboration, *Electron reconstruction and identification in the ATLAS experiment using the 2015 and 2016 LHC proton-proton collision data at $\sqrt{s} = 13$ TeV*, Eur. Phys. J. C **79** (2019) 639, arXiv: 1902.04655 [physics.ins-det].

[80] W. Lampl et al., *Calorimeter Clustering Algorithms: Description and Performance*, ATL-LARG-PUB-2008-002, ATL-COM-LARG-2008-003 (2008), URL: https://cds.cern.ch/record/1099735.

[81] R. Frühwirth, *A Gaussian-mixture approximation of the Bethe–Heitler model of electron energy loss by bremsstrahlung*, Computer Physics Communications **154** (2003) 131.

[82] ATLAS Collaboration, *Electron and photon performance measurements with the ATLAS detector using the 2015–2017 LHC proton-proton collision data*, JINST **14** (2019) P12006, arXiv: 1908.00005 [hep-ex].

[83] ATLAS Collaboration, *Muon reconstruction performance of the ATLAS detector in proton–proton collision data at $\sqrt{s}$ =13 TeV*, Eur. Phys. J. C **76** (2016) 292, arXiv: 1603.05598 [hep-ex].

[84] ATLAS Collaboration, *Jet reconstruction and performance using particle flow with the ATLAS Detector*, Eur. Phys. J. C **77** (2017) 466, arXiv: 1703.10485 [hep-ex].

[85] ATLAS Collaboration, *Jet global sequential corrections with the ATLAS detector in proton-proton collisions at sqrt(s) = 8 TeV*, ATLAS-CONF-2015-002 (2015), URL: https://cds.cern.ch/record/2001682.

[86] ATLAS Collaboration, *ATLAS detector and physics performance: Technical Design Report, 1*, Technical design report. ATLAS, Geneva: CERN, 1999, URL: https://cds.cern.ch/record/391176.

[87] M. Cacciari, G. P. Salam, and G. Soyez, *The anti-k_t jet clustering algorithm*, JHEP **04** (2008) 063, arXiv: 0802.1189 [hep-ph].

[88] S. D. Ellis and D. E. Soper, *Successive combination jet algorithm for hadron collisions*, Phys. Rev. D **48** (1993) 3160, arXiv: hep-ph/9305266.

[89] ATLAS Collaboration, *Determination of jet calibration and energy resolution in proton-proton collisions at $\sqrt{s} = 8$ TeV using the ATLAS detector*, Eur. Phys. J. C **80** (2020) 1104, arXiv: 1910.04482 [hep-ex].

[90] M. Cacciari, G. P. Salam, and G. Soyez, *FastJet User Manual*, Eur. Phys. J. C **72** (2012) 1896, arXiv: 1111.6097 [hep-ph].

[91] M. Aaboud et al., *Jet energy scale measurements and their systematic uncertainties in proton-proton collisions at $\sqrt{s} = 13$ TeV with the ATLAS detector*, Phys. Rev. D **96** (2017) 072002, arXiv: 1703.09665 [hep-ex].

[92] ATLAS Collaboration, *Identification of Jets Containing b-Hadrons with Recurrent Neural Networks at the ATLAS Experiment*, ATL-PHYS-PUB-2017-003 (2017), URL: http://cds.cern.ch/record/2255226.

[93] C. Varni, *Tracking and flavour tagging performance at ATLAS*, PoS **ICHEP2020** (2021) 793.

[94] ATLAS Collaboration, *Jet reclustering and close-by effects in ATLAS run II*, ATLAS-CONF-2017-062 (2017), URL: https://cds.cern.ch/record/2275649.

[95] C. F. Galea, *Tau Lepton Reconstruction in ATLAS*, Nucl. Part. Phys. Proc. **287-288** (2017) 111, ed. by C. Yuan, X. Mo, and L. Wang.

[96] ATLAS Collaboration, *Identification of hadronic tau lepton decays using neural networks in the ATLAS experiment*, ATL-PHYS-PUB-2019-033 (2019), URL: https://cds.cern.ch/record/2688062.

[97] ATLAS Collaboration, *Performance of missing transverse momentum reconstruction with the ATLAS detector using proton-proton collisions at $\sqrt{s} = 13$ TeV*, Eur. Phys. J. C **78** (2018) 903, arXiv: 1802.08168 [hep-ex].

[98] A. Collaboration, *E_T^{miss} performance in the ATLAS detector using 2015-2016 LHC pp collisions*, ATLAS-CONF-2018-023 (2018), URL: https://cds.cern.ch/record/2625233.

[99] ATLAS Collaboration, *Letter of Intent for the Phase-II Upgrade of the ATLAS Experiment*, CERN-LHCC-2012-022, LHCC-I-023 (2012), URL: https://cds.cern.ch/record/1502664.

[100] ATLAS Collaboration, *Technical Design Report for the ATLAS Inner Tracker Strip Detector*, CERN-LHCC-2017-005, ATLAS-TDR-025 (2017), URL: https://cds.cern.ch/record/2257755.

[101] *ATLAS Radiation Simulation Public*,
URL: https://twiki.cern.ch/twiki/bin/view/AtlasPublic/RadiationSimulationPublicResults (visited on 02/23/2022).

[102] S. Wonsak and ATLAS Collaboration,
The ATLAS ITk Strip Detector System for the Phase-II LHC Upgrade, PoS (2020),
URL: https://cds.cern.ch/record/2706027.

[103] *EX-1515 epoxy data sheet*,
URL: https://www.toraytac.com/media/57c4813d-ce39-4b11-a5f4-11c3aaeeeef4/14xkyg/TAC/Documents/Data_sheets/Thermoset/UD%20tapes%20and%20prepregs/EX-1515_Cyanate-Ester_PDS.pdf (visited on 02/28/2022).

[104] *T300 carbon fibers data sheet*,
URL: https://www.toraycma.com/wp-content/uploads/T300-Technical-Data-Sheet-1.pdf.pdf (visited on 02/28/2022).

[105] B. Schneider, *Thermische Ausdehnung von Faserverbunden bei tiefen Temperaturen*, Hauptversammlung der Deutschen Gesellschaft fuer Materialkunde (1991).

[106] *Hysol adhesive data sheet*, URL: https://twiki.cern.ch/twiki/pub/Main/AtlasEdinburghGroupMaterialStudies/Henkel_Hysol_EA_9396_epoxy.pdf (visited on 02/28/2022).

[107] F. Guarino, C. Hauviller, and M. Tavlet,
Compilation of radiation damage test data. 4. Adhesives, CERN-2001-006 (2001).

[108] *CF mat UD safety data sheet*,
URL: http://www.ezentrumbilder.de/rg/pdf/si_en_190289.pdf (visited on 02/25/2022).

[109] ATLAS Collaboration, *Search for heavy particles decaying into a top-quark pair in the fully hadronic final state in pp collisions at $\sqrt{s}$ = 13 TeV with the ATLAS detector*, Phys. Rev. D **99** (2019) 092004, arXiv: 1902.10077 [hep-ex].

[110] ATLAS Collaboration,
Search for heavy particles decaying into top-quark pairs using lepton-plus-jets events in proton–proton collisions at $\sqrt{s}$ = 13 TeV with the ATLAS detector,
Eur. Phys. J. C **78** (2018) 565, arXiv: 1804.10823 [hep-ex].

[111] ATLAS Collaboration, *Search for pair production of up-type vector-like quarks and for four-top-quark events in final states with multiple b-jets with the ATLAS detector*, JHEP **07** (2018) 089, arXiv: 1803.09678 [hep-ex].

[112] ATLAS Collaboration, *Search for new phenomena in events with same-charge leptons and b-jets in pp collisions at $\sqrt{s}$ = 13 TeV with the ATLAS detector*, JHEP **12** (2018) 039, arXiv: 1807.11883 [hep-ex].

[113] ATLAS Collaboration, *Luminosity determination in pp collisions at $\sqrt{s}$ = 13 TeV using the ATLAS detector at the LHC*, ATLAS-CONF-2019-021 (2019), URL: https://cds.cern.ch/record/2677054.

[114] ATLAS Collaboration, *The ATLAS Simulation Infrastructure*, Eur. Phys. J. C **70** (2010) 823, arXiv: 1005.4568 [physics.ins-det].

[115] ATLAS Collaboration, *Performance of the Fast ATLAS Tracking Simulation (FATRAS) and the ATLAS Fast Calorimeter Simulation (FastCaloSim) with single particles*, ATL-SOFT-PUB-2014-001 (2014), URL: https://cds.cern.ch/record/1669341.

[116] D. Lange, *The EvtGen particle decay simulation package*, Nuclear Instruments & Methods in Physics Research Section A-accelerators Spectrometers Detectors and Associated Equipment **462** (2001) 152.

[117] R. D. Ball et al., *Parton distributions for the LHC Run II*, JHEP **04** (2015) 040, arXiv: 1410.8849 [hep-ph].

[118] ATLAS Collaboration, *ATLAS Pythia 8 tunes to 7 TeV data*, ATL-PHYS-PUB-2014-021 (2014), URL: https://cds.cern.ch/record/1966419.

[119] S. Frixione, P. Nason, and G. Ridolfi, *A Positive-weight next-to-leading-order Monte Carlo for heavy flavour hadroproduction*, JHEP **09** (2007) 126, arXiv: 0707.3088 [hep-ph].

[120] S. Frixione, P. Nason, and G. Ridolfi, *The POWHEG-hvq manual version 1.0*, (2007), arXiv: 0707.3081 [hep-ph].

[121] P. Nason, *A New method for combining NLO QCD with shower Monte Carlo algorithms*, JHEP **11** (2004) 040, arXiv: hep-ph/0409146.

[122] S. Frixione, P. Nason, and C. Oleari, *Matching NLO QCD computations with Parton Shower simulations: the POWHEG method*, JHEP **11** (2007) 070, arXiv: 0709.2092 [hep-ph].

[123] S. Frixione, E. Laenen, P. Motylinski, B. R. Webber, and C. D. White, *Single-top hadroproduction in association with a W boson*, JHEP **07** (2008) 029, arXiv: 0805.3067 [hep-ph].

[124] M. Bahr et al., *Herwig++ Physics and Manual*, Eur. Phys. J. C **58** (2008) 639, arXiv: 0803.0883 [hep-ph].

[125] L. A. Harland-Lang, A. D. Martin, P. Motylinski, and R. S. Thorne, *Parton distributions in the LHC era: MMHT 2014 PDFs*, Eur. Phys. J. C **75** (2015) 204, arXiv: 1412.3989 [hep-ph].

[126] ATLAS Collaboration,
Vertex Reconstruction Performance of the ATLAS Detector at $\sqrt{s}$ = 13 TeV,
ATL-PHYS-PUB-2015-026 (2015),
URL: https://cds.cern.ch/record/2037717.

[127] ATLAS Collaboration,
Performance of electron and photon triggers in ATLAS during LHC Run 2,
Eur. Phys. J. C **80** (2020) 47, arXiv: 1909.00761 [hep-ex].

[128] ATLAS Collaboration, *Performance of the ATLAS muon triggers in Run 2*,
JINST **15** (2020) P09015, arXiv: 2004.13447 [physics.ins-det].

[129] ATLAS Collaboration, *Measurement of the $t\bar{t}t\bar{t}$ production cross section in pp collisions at $\sqrt{s}$=13 TeV with the ATLAS detector*, CERN-EP-2021-075 (2021),
arXiv: 2106.11683 [hep-ex].

[130] ATLAS Collaboration, *Search for new resonances in mass distributions of jet pairs using 139 fb^{-1} of pp collisions at $\sqrt{s}$ = 13 TeV with the ATLAS detector*,
JHEP **03** (2020) 145, arXiv: 1910.08447 [hep-ex].

[131] G. Cowan, K. Cranmer, E. Gross, and O. Vitells,
Asymptotic formulae for likelihood-based tests of new physics,
Eur. Phys. J. C **71** (2011) 1554, [Erratum: Eur.Phys.J.C 73, 2501 (2013)],
arXiv: 1007.1727 [physics.data-an].

[132] J. Neyman and E. S. Pearson,
On the Problem of the Most Efficient Tests of Statistical Hypotheses,
Phil. Trans. Roy. Soc. Lond. A **231** (1933) 289.

[133] S. S. Wilks, *The Large-Sample Distribution of the Likelihood Ratio for Testing Composite Hypotheses*, Annals Math. Statist. **9** (1938) 60.

[134] G. Choudalakis, "On hypothesis testing, trials factor, hypertests and the BumpHunter,"
PHYSTAT 2011, 2011, arXiv: 1101.0390 [physics.data-an].

[135] A. L. Read, *Presentation of search results: The CL(s) technique*,
J. Phys. G **28** (2002) 2693, ed. by M. R. Whalley and L. Lyons.

[136] L. Lista, "Practical Statistics for Particle Physicists,"
2016 European School of High-Energy Physics, 2017 213,
arXiv: 1609.04150 [physics.data-an].

[137] ATLAS Collaboration, *Jet Calibration and Systematic Uncertainties for Jets Reconstructed in the ATLAS Detector at $\sqrt{s}$ = 13 TeV*,
ATL-PHYS-PUB-2015-015 (2015),
URL: https://cds.cern.ch/record/2037613.

[138] ATLAS Collaboration, *Tagging and suppression of pileup jets with the ATLAS detector*,
ATLAS-CONF-2014-018 (2014),
URL: https://cds.cern.ch/record/1700870.

[139] D. de Florian et al.,
Handbook of LHC Higgs Cross Sections: 4. Deciphering the Nature of the Higgs Sector, **2/2017** (2016), arXiv: 1610.07922 [hep-ph].

[140] ATLAS Collaboration,
Combined measurements of Higgs boson production and decay using up to 80 fb^{-1} *of proton-proton collision data at* $\sqrt{s}$ *= 13 TeV collected with the ATLAS experiment*, Phys. Rev. D **101** (2020) 012002, arXiv: 1909.02845 [hep-ex].

[141] J. Alwall et al., *Comparative study of various algorithms for the merging of parton showers and matrix elements in hadronic collisions*, Eur. Phys. J. C **53** (2008) 473, arXiv: 0706.2569 [hep-ph].

[142] ATLAS Collaboration, *Measurements of inclusive and differential fiducial cross-sections of* $t\bar{t}$ *production with additional heavy-flavour jets in proton-proton collisions at* $\sqrt{s}$ *= 13 TeV with the ATLAS detector*, JHEP **04** (2019) 046, arXiv: 1811.12113 [hep-ex].

[143] J. Butterworth et al., *PDF4LHC recommendations for LHC Run II*, J. Phys. G **43** (2016) 023001, arXiv: 1510.03865 [hep-ph].

[144] J. Alitti et al.,
A measurement of two-jet decays of the W and Z bosons at the CERN $\bar{p}p$ *collider*, Z. Phys. C **49** (1990) 17, URL: https://cds.cern.ch/record/210698.

[145] ATLAS Collaboration, *Recommendations for the Modeling of Smooth Backgrounds*, ATL-PHYS-PUB-2020-028 (2020),
URL: https://cds.cern.ch/record/2743717.

List of Figures

List of Tables

Acknowledgements

I would like to thank Krisztian Peters for his guidance and advice which helped me to succeed in completing my PhD project. I would also like to thank Loïc Valéry and Philipp Gadow for their invaluable help along the way, always taking the time to answer my questions and helping me achieve my tasks. It was a great pleasure to be part of the BSM4tops analysis team and I'm thankful for the active discussions and productive mindsets during the entire process of the analysis. Special thanks to Elise Le Boulicaut who was the other main contributor to the analysis and tirelessly carried out numerous studies.

I would also like to thank the DESY ATLAS tech team for welcoming me openly and sparking my joy for engineering. Many thanks to Sergio Díez Cornell for introducing me to the project and his advice. Special thanks to Darío Ariza, Sören Ahrens and Bob Langer for their time and dedication. It was always great fun to work at the lab with you.